# Abstract

The efficiency of particulate photocatalysts used to split water is limited by the recombination of photogenerated electrons and holes and the back reaction of intermediate species to reform water. This efficiency could be improved by better spatial separation of charge carriers and reaction sites. The primary goal of this work is to test the hypothesis that dipolar fields in ferroelectric substrates can drive photogenerated electrons and holes in opposite directions, thus creating spatially distinct locations for photochemical oxidation and reduction reactions on the surfaces of supported $TiO_2$ thin films.

To investigate this, thin films of $TiO_2$ (10 to 100 nm) were grown on polycrystalline, ferroelectric $BaTiO_3$ and $BiFeO_3$ substrates by pulsed laser deposition. The films grown on $BaTiO_3$ were characterized by electron backscatter diffraction, which showed that some substrate orientations stabilize the anatase phase while others stabilize rutile. Specifically, orientations within about 25° of (100) $BaTiO_3$ promote the growth of biaxially orientated anatase such that [001] $BaTiO_3$ is parallel to [001] anatase and [110] $BaTiO_3$ is parallel to [110] anatase. Orientations further from (100) stabilize the growth or rutile. While the rutile growth is epitaxial, there is no single orientation relationship.

The photochemical properties of the surface were probed using the photochemical reduction of $Ag^+$ to $Ag^0$ and the photochemical oxidation of $Pb^{2+}$ to $Pb^{4+}$. These specific oxidation and reduction reactions were chosen because they leave behind insoluble reaction products (Ag and $PbO_2$) on the surface that allow the location of the reaction to be determined. The same locations of the surface were imaged by atomic

force microscope before and after the reaction and the heights of the reaction product on the surface was used as a measure of the extent of the reactivity.

In this study, we found that the ferroelectric substrate does influence reactivity on the surface of the thin film. Oxidation and reduction reactions on the thin film surface were observed to occur in separate locations. This effect was observed for films grown on both n-type $BaTiO_3$ and p-type $BiFeO_3$. The observed spatial localization of reactions diminished as the thickness of the film was increased from 10 nm to 100 nm. The effect also diminished as the carrier concentration in the film was increased. Experiments in which the reactivity of the bare substrate was compared to the reactivity of the supported film showed that domains that promoted reduction (or oxidation) on the substrate surface also promoted reduction (or oxidation) on the film surface.

Because the $BaTiO_3$ substrates were polycrystalline, the effect of film and $BaTiO_3$ substrate orientation on the reactivity was also explored. No significant differences in the reactivity of {100}, {110} and {111} $BaTiO_3$ were observed. For some rutile films orientations near the type (hk0), the presence of the ferroelectric substrate appeared to increase the photochemical reactivity of the $TiO_2$ as compared much thicker films with the same structure and orientation.

# List of Figures

# Table of Contents

# 1 Introduction

## 1.1 Motivation

Rising concern over the inability of fossil fuels to meet future energy needs, as well as their negative environmental impact, has prompted investigations into alternative energy sources. One potential alternative is hydrogen, a clean burning fuel with three times the energy density of oil. A breakthrough in hydrogen synthesis occurred in 1972, when Fujishima and Honda [1] discovered that illuminated $TiO_2$ could be used to catalyze the dissociation of water into $H_2$ and $O_2$ (see Fig. 1.1). When a semiconductor, such as $TiO_2$, is exposed to light with an energy exceeding its band gap, electrons are excited into the conduction band, leaving conducting holes in the valence band. If they do not recombine, these electrons and holes are then able to participate in oxidation or reduction reactions at the semiconductor surface. For example, water can be split into hydrogen and oxygen according to the following reactions:

$H_2O + 2h^+ = 1/2O_2 + 2H^+$ (oxidation reaction)

$2H^+ + 2e^- = 2H_2$ (reduction reaction)

In this system, illumination could be provided by sunlight (for titania, only the UV part of the spectrum has enough energy to create electrons and holes), which is renewable and readily available, making this process an extremely attractive means of energy production.

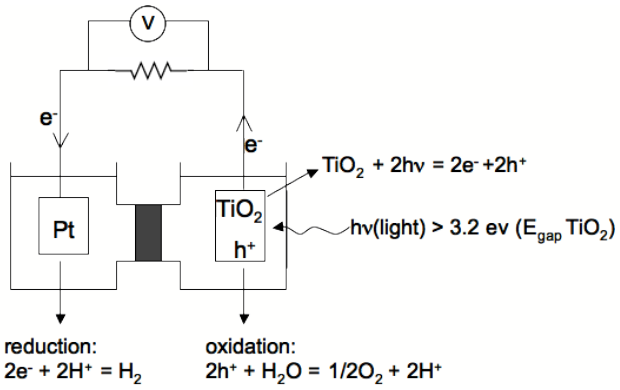


**Figure 1.1**. Cell used by Fujushima and Honda [1]. Photogenerated holes react on the $TiO_2$ surface to produce $O_2$ and $H^+$. Photogenerated electrons migrate to the Pt electrode where they react with $H^+$ to produce $H_2$.

However, for hydrogen gas to be a feasible alternative, it must be possible to produce it both efficiently and economically. Current research focuses on two main setups for water photolysis; the first setup is the photoelectrochemical cell (Figure 1.1) [1, 2] and the second is the particle photocatalyst (Figure 1.2) [3-7], which is essentially a "short-circuited" version of the photoelectrochemical cell, in which the two electrodes are in contact.

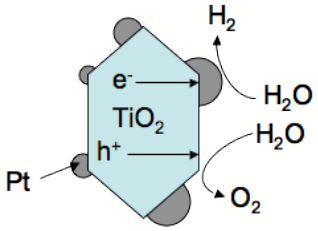


**Figure 1.2**. Platinized titania particulate cell. Reduction occurs on the Pt surface, while oxidation takes place on $TiO_2$; the proximity of anode and cathode leads to recombination of charge carriers and back reaction of intermediate species.

While photoelectrochemical cells have demonstrated promising efficiencies [2], their high cost prevents them from being practical for large-scale application. Particulate systems are a less expensive alternative, however their efficiencies are limited by electron

and hole recombination and back reaction of intermediate species to reform water. This can be attributed to the fact that, unlike in the case of the photoelectrochemical cell, there is not efficient spatial separation between photogenerated charges or oxidation and reduction reaction sites. [3, 4, 8, 9] Thus, one current goal of particle catalyst research is to find materials that better separate charge and reaction sites. A notable example of this is a La-doped $NaTaO_3$ particle photocatalyst studied by Kato et al., [10] which demonstrated a very high quantum efficiency (56% at 270 nm). The observed efficiency was attributed to the formation of a surface nanostep structure, which provided unique, spatially separated sites for oxidation and reduction; reduction took place on the step edges and oxidation occurred in the grooves between steps. A number of other efforts at improving particle photocatalyst efficiency are summarized in several recent review articles [3-7].

In this study, we aim to achieve separation of the anode and cathode by utilizing internal fields in ferroelectric metal oxides, specifically barium titanate and bismuth ferrite. Previous research has shown that the internal dipolar field in ferroelectric $BaTiO_3$ acts to drive electrons and holes to different locations, thus creating separate sites for reduction and oxidation [11-15]. Reduction (electron transport) was preferred on surfaces that intersected with the positive end of the polarization dipole, while oxidation (hole transport) was favored on surfaces that intersected the negative end [11-16]. However, many ferroelectrics are susceptible to photocorrosion and degradation in an aqueous environment, hence their surfaces cannot be used to catalyze reactions. A suitable solution is to grow a film ($TiO_2$) on the ferroelectric material, so that its surface may be protected. Prior work has suggested that the polarization charge in ferroelectric

substrates can modify charge carrier transport in thin semiconducting films [17]. The work in this thesis is driven by the hypothesis that the internal dipolar field in the ferroelectric substrate will influence charge carriers in the film, and thus create spatially distinct sites for oxidation and reduction.

## 1.2 Objectives

As discussed above, the dipolar field in a ferroelectric material can separate photogenerated electrons and holes and create spatially distinct sites for oxidation and reduction on its surface. This research focuses on determining how the dipolar field from an underlying ferroelectric substrate will affect the photochemical behavior of a protective $TiO_2$ film. Additionally, this work examines how specific properties of the substrate and film impact the photochemical reactivity of the film surface. Experiments were designed to answer the following questions:

**1** Can a ferroelectric substrate create unique, preferred sites for oxidation and reduction on the surface of a protective thin film? If so, what is the relationship between the underlying polarization and the preferred half reaction (for example, does the positive end of the dipole create a preferred site for oxidation or reduction on the film surface)?

**2** What influence does the type of junction (i.e. n/n or p/n) between the substrate and film have?

**3** How does the thickness of the film influence the effect of the ferroelectric?

**4** How does the carrier concentration in the film change reaction behavior?

**5** How do substrate and film orientation affect photochemical reactivity?

## 1.3 Organization

This document is organized as follows. Chapter 2 presents relevant background material for this thesis. Chapter 3 discusses the experimental approach. In Chapter 4, the orientation relationship between the $BaTiO_3$ substrate and the $TiO_2$ film is discussed. The orientation relationship between the $BiFeO_3$ substrate and $TiO_2$ was not studied. In Chapter 5, the effect of ferroelectric $BaTiO_3$ and $BiFeO_3$ substrates on photochemical reactivity of $TiO_2$ thin film surfaces is described. Chapters 6 and 7 attempt to establish a correlation between substrate domain polarization and reactivity on thin film surfaces. Chapters 8, 9, and 10 examine the effects of film thickness, film carrier concentration and substrate and film orientation, respectively.

# 2 Background

## 2.1 Introduction

The purpose of this chapter is to discuss concepts and background material that are relevant to this thesis. Since the primary focus of this work is to examine photochemical reactions on thin $TiO_2$ films supported by ferroelectric oxide substrates, relevant information about ferroelectric oxides and photochemistry on both ferroelectric and non-ferroelectric semiconductor materials is presented. Pertinent information about the specific materials being used in this work is also included. Additionally, the properties of ferroelectric/semiconductor heterostructures are discussed. Finally, known orientation relationships between $BaTiO_3$ and titania are reviewed and the orientation sensitivity of the reactivity of titania is discussd.

## 2.2 Ferroelectricity

In a centrosymmetric crystal, application of a stress results in the displacement of charge. The displacement is symmetric, however, so all charge movements are compensated and the deformation does not cause polarization. Most noncentrosymmetric crystals, on the other hand, do exhibit an electrical polarity when a stress is applied. Equivalently, an applied electric field produces a mechanical strain. Any material that demonstrates this behavior is termed piezoelectric. Ferroelectrics are a special class of piezoelectrics that possess a spontaneous polarization below a specific temperature, $T_C$ (Curie temperature). Ferroelectrics have multiple polar axes and their polarization can be switched by an applied electric field. [18]

*2.2.1 Barium titanate*

For barium titanate, the Curie temperature is 120°C. Above this temperature, the cubic perovskite crystal structure is stable, while below it a tetragonally distorted form of this structure becomes energetically favorable. Orthorhombic and rhombohedral structures become stable at temperatures below 5°C and -90°C, respectively [19]. These two structures are pictured in Fig. 2.1. In the tetragonal structure (a = 3.997 Å, c = 4.03 Å [19]), the $Ti^{4+}$ and $O^{2-}$ ions are displaced from their symmetrical cubic perovskite positions. Consequently, the centers of positive and negative charge no longer coincide and a spontaneous polarization in the direction of $Ti^{4+}$ displacement results. For barium titanate, the spontaneous polarization creates a surface charge of 26 $\mu C/cm^2$ [20] and can occur in the ±z, ±x, or ±y directions. [18]

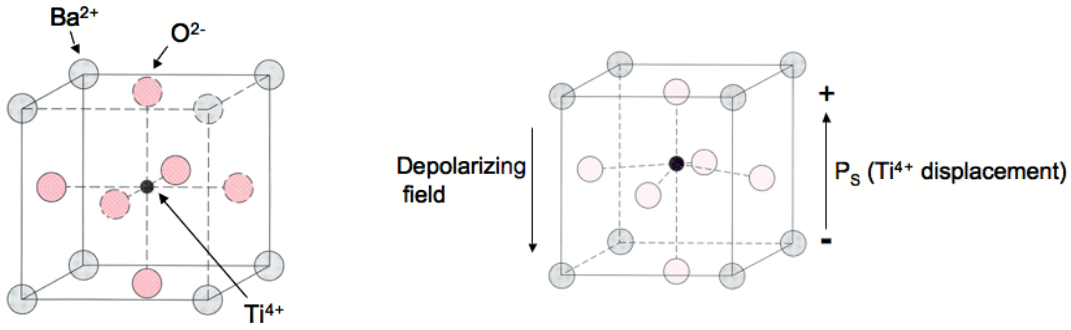


**Figure 2.1**. **(a)** cubic perovskite structure **(b)** tetragonally distorted structure where $Ti^{4+}$ is displaced up. The top surface becomes positively charged while the bottom surface is negatively charged. Redrawn from [21].

The charged surfaces created by the spontaneous polarization (see Fig 2.1) result in the formation of a counteracting depolarizing field. This depolarizing field is associated with a positive (unfavorable) energy contribution that is generally minimized

through the formation of a domain structure. Domains are regions of a ferroelectric in which the orientation of the polarization vector is uniform. When multiple randomly polarized domains are present, depolarizing fields can compensate for one another and the energy of the system is decreased. It would appear that as more domains form, compensation would be more complete and the energy of the system would decrease. Domains cannot continue to form indefinitely, however, since domain walls (regions between domains within which the spontaneous polarization vector changes from one orientation to another) increase the overall energy of the system. The equilibrium number of domains is thus determined by balancing the decrease in the depolarizing field energy with the increase in domain wall energy.

For $BaTiO_3$, two types of boundaries can form between neighboring domains. A 180° boundary forms between domains whose polarization vectors are 180° apart (for example, between [001] and [00-1] oriented polarization vectors). Likewise, 90° boundaries occur when polarization vectors of adjacent domains are 90° apart. It is energetically favorable for 90° boundaries to form on (110) planes [22], thus these boundaries appear straight. A 180° boundary, on the other hand, can form on any plane in the <001> zone and thus appears curvy. A schematic of a $BaTiO_3$ domain structure is shown in Fig. 2.2. In this schematic the two types of domain boundaries are shown to overlap. Orientations of polarization vectors in the various regions are marked. A topographical image (obtained from Atomic Force Microscopy) of the domain structure of a polished $BaTiO_3$ polycrystal is shown in Fig. 2.3. The contrast in the image represents varying heights, where black corresponds to lower features and white corresponds to higher features. In this image, it is likely that the height contrast between

domains is caused by differential polishing (domains with different polarization vectors wear at different rates). This differential polishing makes it possible to observe the boundaries between domains. Height contrast may also be visible for samples that have been annealed at a temperature above the Curie temperature. As the sample is cooled below 120°C, the unit cells become tetragonally distorted and a stretching in the direction of the polarization takes place. This stretching causes domains whose polarization vector runs normal to the surface to be slightly raised (or lowered) with respect to domains whose polarization runs parallel to the surface (see Fig. 2.4). It is important to note that if the sample is heated above the Curie temperature after polishing, domain contrast from differential polishing may remain on the surface, but will not be expected to correlate with the actual domain structure (since a new domain structure may form on cooling from $T_C$).

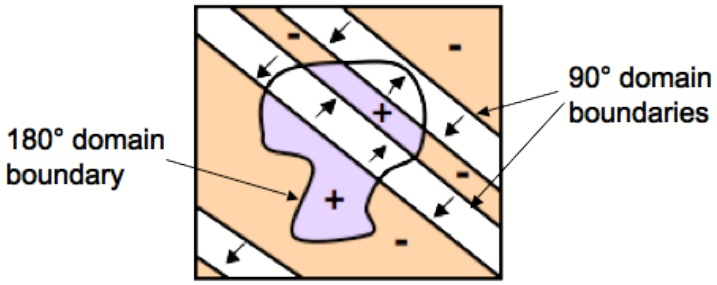


**Figure 2.2**. Schematic of the $BaTiO_3$ domain structure. The + represents polarization vectors that point in the +z direction, the – represents those that point in the –z direction, and the arrows correspond to x and y lateral directions. Reproduced from [23].

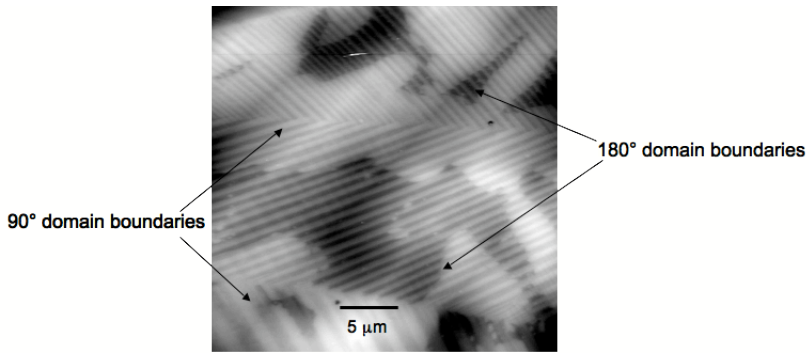


**Figure 2.3**. Domain structure of $BaTiO_3$. Adjacent stripes represent domains containing polarization vectors separated by 90° angles, curved boundaries form between domains with polarization vectors 180° apart. Vertical black-to-white contrast is 70 nm.

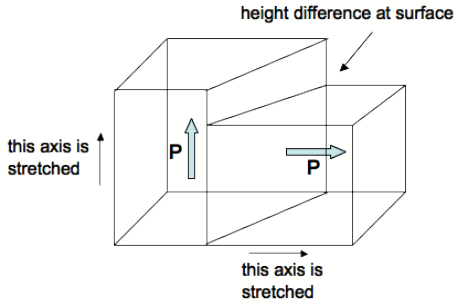


**Figure 2.4**. Schematic showing height contrast that develops after annealing samples at temperatures above the Curie temperature.

### *2.2.2 Bismuth Ferrite*

Bismuth ferrite has a Curie temperature of about 830°C [24-26], which is high compared to many other ferroelectrics. The charge resulting from the spontaneous polarization is 6.1 $\mu C/cm^2$ for the bulk, but has been reported to be as high as 100 $\mu C/cm^2$ for thin films [26]. The structure of $BiFeO_3$ is shown in Fig. 2.5. Bismuth ferrite has a rhombehedral structure, which consists of two distorted cubic perovskite blocks connected along the pseudocubic <111> body diagonal [27]. The spontaneous polarization can occur along any of the four pseudocubic <111> body diagonals in either the positive or negative direction, resulting in a total of eight possible polarization vectors

[27]. The three possible domain walls have polarization vectors separated by 180°, 71° or 109° [27, 28]. An image of the domain structure in bismuth ferrite taken with an optical microscope is presented in Fig. 2.6.

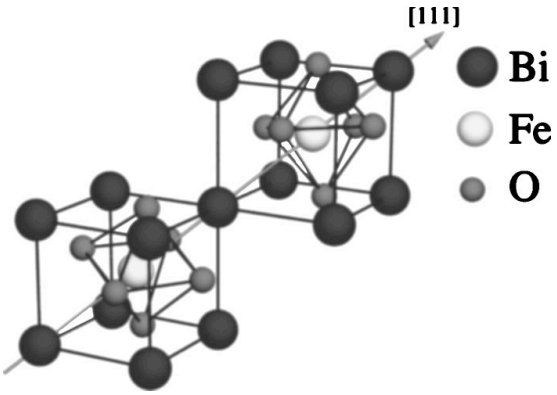


**Figure 2.5.** Structure of $BiFeO_3$ showing [111] direction of polarization. Reproduced from [26].

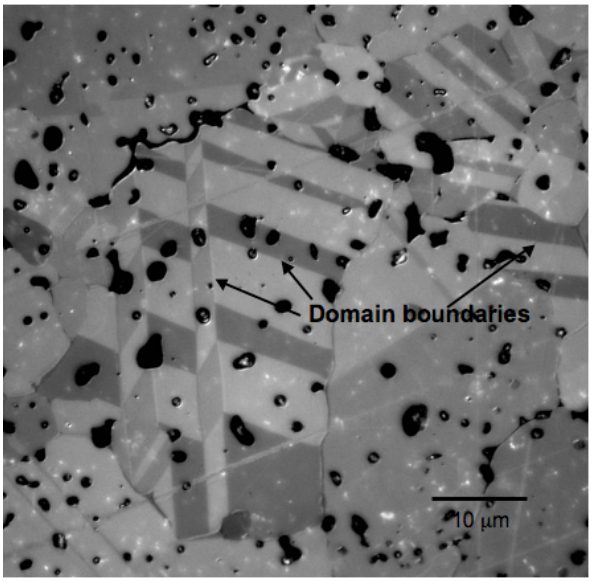


**Figure 2.6.** Visible light microscope image of a polished polycrystalline $BiFeO_3$ surface. Some domain boundaries are marked in the image.

## 2.3 Photochemistry On Semiconductor Surfaces

If a semiconductor is illuminated with light having an energy greater than the band gap energy, it is possible for electrons from the valence band to be excited into the conduction band. The excited electrons leave behind conducting holes, so that for every photon absorbed, an electron-hole pair is generated. If they do not recombine, it is possible for these photogenerated electrons and holes to move to the surface and participate in photochemical reactions, however the likelihood that a certain reaction will actually occur is dependent on several factors. In this section, the factors involved in determining the feasibility of specific reactions on a semiconductor surface are discussed.

### *2.3.1 Energy levels in the solid and solution*

For a photochemical reaction to occur on a semiconductor surface, photogenerated electrons and holes must move to the surface and reduce or oxidize ionic species in the solution. Electron and hole transfer to the ions in the solution will only occur if the charge carriers can lower their energy by participating in the reaction. So, to determine reaction plausibility, it is necessary to compare the energy levels in the solid to those in solution.

In the solution, the energy levels that are available to electrons and holes are dependent on the ions present in the solution. Ions in solution are associated with energy levels (redox potentials) that reflect their tendency to give up or accept electrons. The redox potentials for the photochemical half reactions relevant to this thesis are listed below [29]:

| | | |
|---|---|---|
| $2e^- + 2H^+ = H_2$ | 0 V | (2.1) |
| $Ag^+ + e^- = Ag$ | 0.8 V | (2.2) |
| $O_2 + 4e^- + 4H^+ = 2H_2O$ | 1.23 V | (2.3) |
| $PbO_2 + 4H^+ + 2e^- = Pb^{2+} + 2H_2O$ | 1.5 V | (2.4) |

Eqs. 2.1 and 2.3 are the reduction and oxidation half reactions for the photosplitting of water. Eqs. 2.2 and 2.4 are the half reactions used in this thesis to identify photochemical reaction location (details about these reactions and their use in this thesis are provided in Chapter 3, the experimental section of this document).

Typically, redox potentials for ions in solution are calculated with respect to the Normal Hydrogen Electrode (NHE), i.e. the potentials are given relative to the reaction $H_2 = 2e^- + 2H^+$, which is set at 0 V. A more positive redox potential indicates that a reaction is more likely to proceed to the right, i.e. in the reduction direction. So, for example, reduction of $Ag^+$ to Ag is more likely than the reduction of $2H^+$ ions to a $H_2$ molecule. In Fig. 2.7, the reactions listed above are placed on an energy scale vs. NHE. Note that electron energy increases as you move higher on the scale. Species that have a greater tendency to undergo reduction occupy a lower energy level, since electrons are required for reduction and electrons prefer to move to lower energy states. Analogously, redox couples that are more likely to undergo oxidation will occupy a higher energy level, since higher energy electrons are more likely to be given up.

In a semiconductor, the energy levels occupied by photogenerated electrons and holes are determined by the positions of the conduction and valence band edges. The positions are calculated relative to the "vacuum level", which is defined as the energy of

an electron at infinity. Similar to the case of ions in solution, energy level positions in a solid are related to a materials' tendency to attract an electron. A measure of the tendency of an atom or solid to attract an electron is the electronegativity. The electronegativity of an atom is defined by Mulliken [30, 31] as follows:

$$X(M) = \tfrac{1}{2}(A + I), \qquad (2.5)$$

where X(M) is the electronegativity of atom M, A is the electron affinity (energy required to remove and electron from an anion) and I is the first ionization energy (energy required to remove an electron from a neutral atom).

For a solid compound, Sanderson [32, 33] found that electronegativity can be calculated from the geometric mean of its constituent atom electronegativities (ex. for $AB_2$, $X= [X(A)X(B)^2]^{1/3}$). This electronegativity (X) along with the band gap of the material can be used to relate the position of the semiconductor conduction band edge to the vacuum level (see Fig. 2.8) [34].

To link the solid and solution energy scales, the redox potential for the $H^+/ H_2$ redox couple has to be related to the vacuum level. The $H^+/H_2$ redox energy has been determined to be 4.5 eV below the vacuum level [35]. In Fig. 2.9 energy levels for both solid and solution are plotted together. All half reactions and band edges relevant this thesis are displayed. The positions of band edges were calculated using the method described above. The values used for band gap energy were 3.2 eV for $BaTiO_3$ [36], 3.0 eV for $TiO_2$ [37], and 2.7 for $BiFeO_3$ [24, 38, 39]. In these diagrams, bulk, unbent, flat

band positions are assumed. In reality, values of the band gap are different for carriers traveling in different crystal directions [40, 41].

From Fig. 2.9, we can now predict which reactions are favorable for each semiconductor surface. Photogenerated electrons lie near the conduction band edge and will transfer to energy states in the solution that are lower in energy. For valence band holes, moving to an energy state that is higher on the diagram is energetically favorable. Thus, in order to produce photogenerated charge carriers that have enough energy to split water, the conduction band edge must lie above the $H^+/ H_2$ redox level and the valence band edge must lie below the $H_2O/O_2$ redox level. To meet both of these conditions, the band gap must be at least 1.23 eV, which is the difference in energy between the two half reactions involved in splitting water. From the diagram, we can conclude that water splitting is at least energetically possible for all the materials considered.

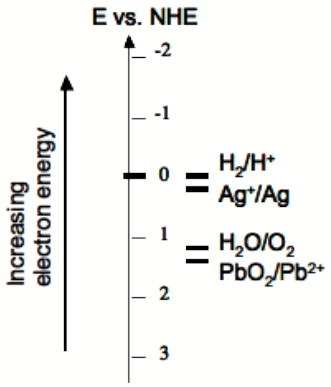


**Figure 2.7.** Energy level diagram showing the positions of relevant half reactions.

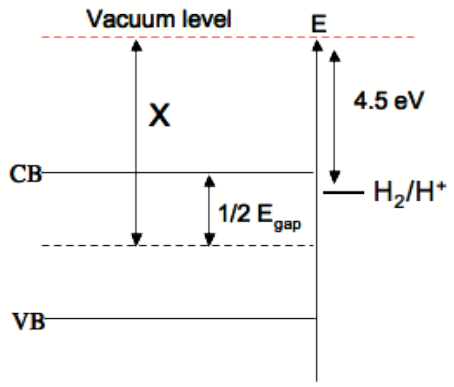


**Figure 2.8.** Energy level diagram showing how positions of semiconductor band edges are related to the vacuum level and the hydrogen reference potential.

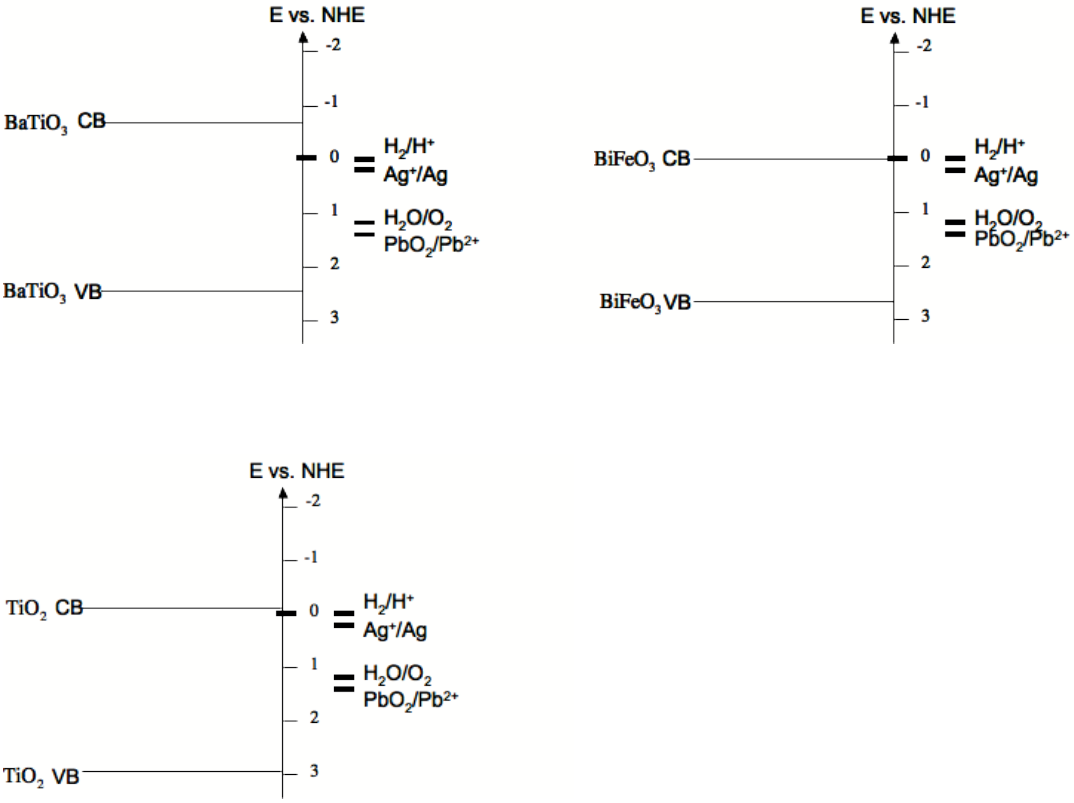


**Figure 2.9.** Energy level diagrams showing how semiconductor band edge positions in $BaTiO_3$, $BiFeO_3$ and $TiO_2$ are related to energy levels of relevant half reactions.

### *2.3.2 Semiconductor/Electrolyte Interface; Semiconductor Band Bending*

As the previous section demonstrated, positions of energy levels in the semiconductor and solution determine whether a specific reaction is energetically feasible for a given material. However, the likelihood that a specific reaction will occur on the surface of a material is highly dependent on the ease of electron or hole transport to the material's surface. Charge carrier transport to the surface is generally governed by the properties of the interface between the semiconductor and the electrolyte. In this section, the characteristics of this interface and their implications for photochemical reactions will be discussed.

When the semiconductor and electrolyte come into contact, regions of excess charge develop in both species (Fig. 2.10). In the semiconductor, the region of excess charge is called the space charge layer; in the solution, two regions of excess charge, the Helmholtz and Gouy layers, are present.

These regions result from charge transfer between the two phases as well as from the presence of surface states at the interface. Charge transfer between the solid and solution occurs when the chemical potentials of the two phases are different [35]. Consider the situation depicted in Fig. 2.11(a). In electrochemistry, the chemical potential for electrons in the solution is given by the redox potential of the solution. In the solid, the chemical potential is given by the position of the Fermi energy. In the figure, the Fermi energy is drawn to represent an n-type semiconductor. Since the Fermi energy is higher than the redox potential, electrons will transfer into the lower energy level in the solution until electronic equilibrium is reached and $E_F$ is equal to $E_{redox}$.

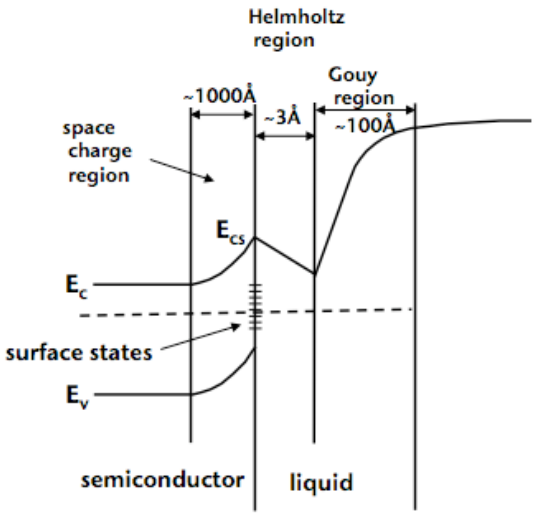


**Figure 2.10.** Schematic showing the regions of excess charge for semiconductors in solution. Reproduced from [42].

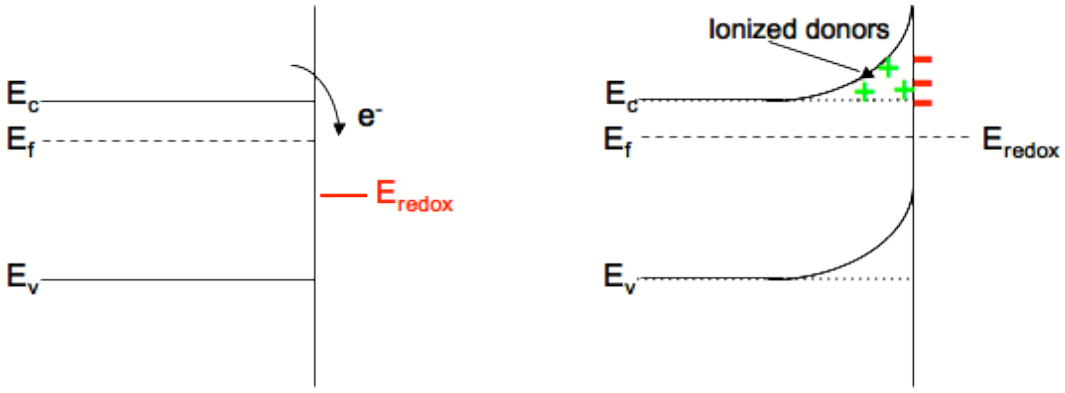


**(a)** **(b)**

**Figure 2.11.** (a) Schematic showing how charge transfer between the semiconductor and solution results in a depletion layer (b) near the semiconductor surface.

This electron transfer to the solution depletes the near surface region in the semiconductor of electrons and results in a build up of excess negative charge at the interface. Electrons in the semiconductor will be repelled by the negatively charged

interface. This is represented by an upward bending of bands near the surface. It makes sense that upward band bending corresponds to a repelling of electrons since electrons prefer to occupy the lowest possible energy state and thus will not climb up the potential hill to a higher energy. The build up of negative charge at the interface must be compensated by positive charge in both the solid and solution. In the semiconductor, the positive charge comes from the immobile donor cores left behind by the electrons that transferred to the solution. For oxides such as $TiO_2$, the positive charge often comes from oxygen vacancies, which introduce conducting electrons in the material according to the following reaction:

$$O_O = \frac{1}{2} O_2 + V_O^{\bullet\bullet} + 2e^-, \qquad (2.6)$$

where $O_O$ is an oxygen ion on an oxygen site, $V_O^{\bullet\bullet}$ is a (positively charged) vacant oxygen site and $e^-$ is an electron in the conduction band [43, 44]. As mentioned above, this region of excess charge is called the space charge layer. In this case, the space charge layer is depleted of majority carriers and is thus called a depletion layer. Typically, depletion widths range from 10 nm to several microns [35]. For example, in Fig. 2.10, the depletion width is shown to be around 100 nm [42]. In the solution, the excess negative charge is compensated by the buildup of mobile, charged ions in the Helmholtz and Gouy layers.

The overall charge at the interface can also be affected by the presence of surface states, such as adsorbed ions. Depending on the amount of surface states and the relative levels of $E_F$ and $E_{redox}$, other types of space charge layers are also possible. Accumulation and inversion layers are pictured in Fig. 2.12. Accumulation layers form when majority carriers are injected into the solid from the solution. Inversion layers form

when the near surface region changes from n-type to p-type or vice versa. So, for example, in an n-type material, an inversion layer would form if conduction band electrons could not supply enough negative charge to the surface and electrons from the valence band had to be extracted.

In general, n-type materials in solution have upward band bending at the surface, while p-type materials have downward band bending at the surface (Fig. 2.13) [45]. This has important implications for photochemical reactions at the semiconductor surface. For the n-type case, electrons will be repelled from the surface by the upward band bending and will move towards the bulk. Holes move in the opposite direction as electrons and will thus be propelled towards the surface. As a result, oxidation reactions (which require holes) will generally be preferred on n-type semiconductor surfaces. Electron transport to the surface is more difficult so the reduction half reaction is generally the rate-limiting reaction on n-type materials. Thus, it should be noted that while one reaction is the "preferred" reaction, both types of half reactions can occur on semiconductor surfaces. Analogously, electrons will be driven to the surface of p-type materials and reduction reactions will be favored.

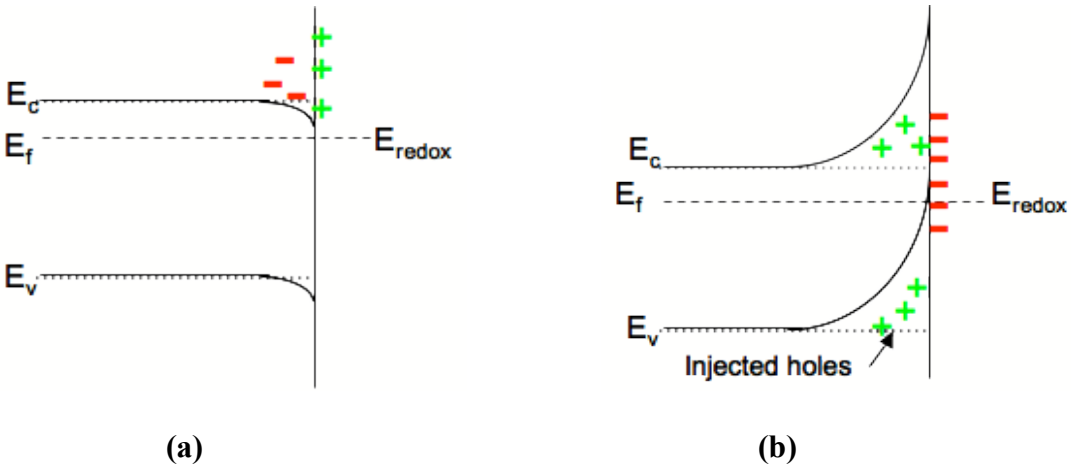


**(a)** **(b)**

**Figure 2.12.** Diagrams illustrating (a) an accumulation layer and (b) an inversion layer.

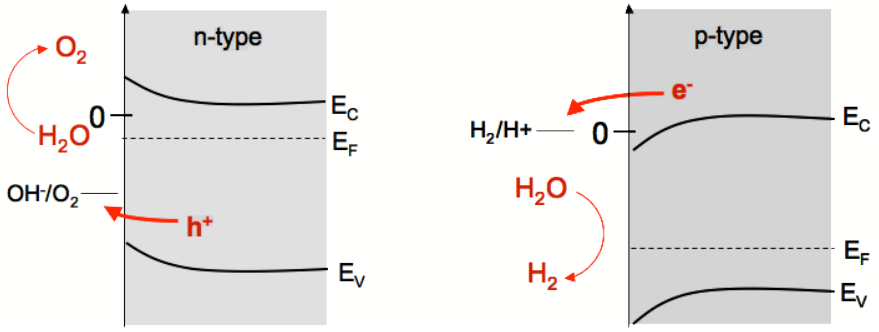


**(a)** **(b)**

**Figure 2.13.** Diagrams showing "easy" reactions for (a) n-type and (b) p-type semiconductors.

### *2.3.3 Semiconductor Band Bending; Relevance for PECs and Particulate Cells*

The importance of the surface band bending region for water photolysis is demonstrated in Fig. 2.14. Here, a schematic of a photoelectrochemical cell used for water splitting is presented. When the n-type semiconductor is illuminated, photogenerated electrons and holes are created. In the near surface region, the electrons and holes are driven in opposite directions by the space charge layer. The hole moves to the semiconductor surface to oxidize water and the electron is driven by an external circuit to the platinum catalyst to reduce protons. This separation of charge carriers and oxidation and reduction sites is essential since it markedly decreases the rate of electron and hole recombination and back reaction to reform water.

For the particulate cell (Fig. 2.15), space charge layers also exist at the semiconductor/solution interface, so holes are driven to the semiconductor surface and electrons are repelled towards the bulk of the particle. Band bending is also present at the interface between the semiconductor and metal co-catalyst.. At this interface, bands bend down [46, 47] and electrons are driven into the Pt, while holes are repelled towards the

bulk. However, unlike in the PEC, these repelled electrons and holes are not driven to separate spatial locations by an external field, so they can recombine in the particle bulk. Furthermore, since there is no spatial separation between the sites for the oxidation and reduction half reactions, $H_2$ and $O_2$ or intermediates (most likely H and OH•) that are successfully produced are at risk of undergoing the thermodynamically favorable back reaction to reform water.

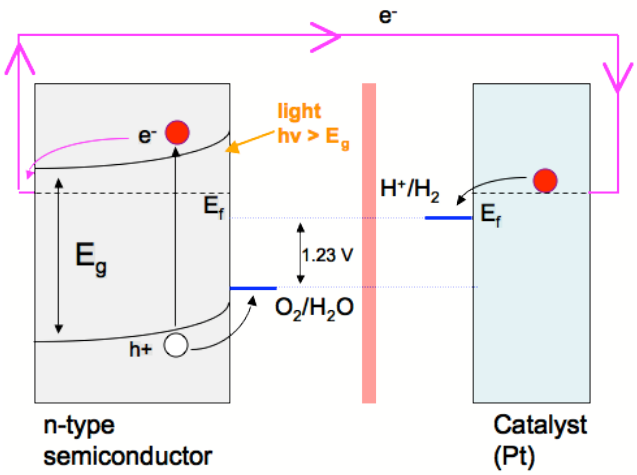


**Figure 2.14.** Schematic illustrating the operation of a PEC. Electrons and holes are separated by the space charge layer and electrons are swept away by the external circuit to the Pt catalyst. In this manner, charge carriers and reaction sites are spatially separated.

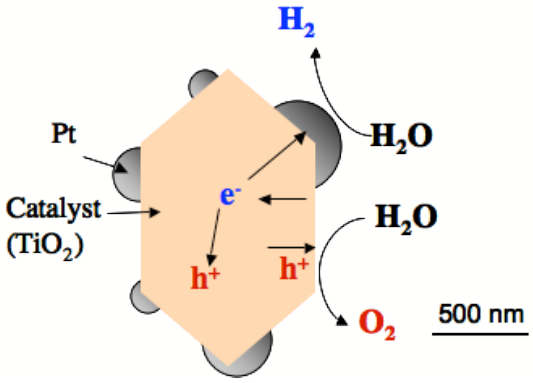


**Figure 2.15.** Schematic illustrating the operation of a particle photocatalyst. Electrons and holes can move to the surface to react if they do not recombine in the bulk of the particle. Unlike in the PEC, sites for oxidation and reduction are in close proximity and thus the likelihood of back reaction to reform water is more likely.

## 2.4 Effect of ferroelectricity on photochemical reactions

Polarization creates dipolar electric fields in ferroelectric materials. As a result, when ferroelectric materials are illuminated, photogenerated electrons and holes are driven in opposite directions. This is called the bulk photovoltaic effect [48-53] (Fig. 2.16). In ferroelectrics, this effect can be exploited to create spatially distinct, preferred sites for both oxidation and reduction. The manner in which ferroelectric polarization affects charge carrier transport and, consequently, reaction behavior is illustrated in Fig. 2.5. In this schematic, the case of a uniformly polarized ferroelectric crystal is considered. At the negative surface, photogenerated electrons are repelled and accordingly, there exists a potential barrier to their flow towards the surface. As electrons are repelled from the surface, photogenerated holes are driven towards it and consequently, oxidation reactions are promoted at the negative surface. The opposite situation occurs on the other end of the crystal, i.e. holes are repelled and there is a downward sloping of bands. Electrons are hence available at the positive surface and reduction is favored. [12, 13, 18, 54]

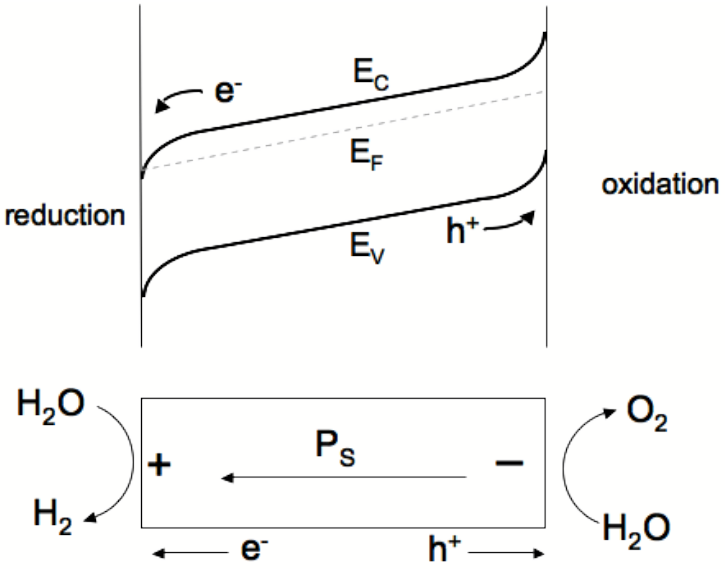


**Figure 2.16**. Band bending behavior of a polarized crystal. Note that the polarization creates a dipolar field across the crystal (bulk photovoltaic effect); this is represented by a sloping of bands across the bulk of the material. The bulk photovoltaic effect can be exploited to move electrons and holes to opposite ends of the crystal.

This domain dependent reaction behavior has been demonstrated in previous works [11, 12, 14, 15, 55-58]. For example, in a work by Giocondi [12], the domain dependent reactivity of $BaTiO_3$ was studied. In Fig. 2.17, results from this study are presented. Fig. 2.17(a) shows an AFM image of the surface of a {100} oriented $BaTiO_3$ single crystal. Fig. 2.17(b) shows the same location after reaction in silver nitrate solution. Here, the reduction of $Ag^+$ ions to Ag metal has occurred on the $BaTiO_3$ surface. White contrast results from the deposition of Ag metal onto the surface where the reaction occurred. It is evident that the reduction reaction has occurred preferentially in certain locations. Fig. 2.17(c) again shows the same location, this time after reaction

in lead acetate solution. Oxidation of lead ions results in the formation of lead oxide, which, like Ag metal, is left behind on the surface at the reaction location. It is clear that the oxidation reaction and reduction reactions are preferred on spatially distinct, complementary surfaces. In the study, it was determined (using etching techniques) that reduction occurred on domain surfaces where the polarization vector was aligned with its positive end towards the surface, while oxidation was preferred on domain surfaces where the dipole had the opposite orientation. Domain selective deposition of insoluble reaction products has been confirmed in numerous works for several ferroelectric materials including $BaTiO_3$ [11], PZT [11, 14, 15]and $LiNbO_3$ [55, 56]. Furthermore, domain dependent reaction behavior has also been suggested for the photosplitting of water. Inoue et al. [58] observed that the activity of $H_2$ formation (from reduction reaction) was significantly greater on a positively poled PZT surface than on a negatively poled surface (for poled materials, an electric field is used to align all polarization vectors in the same direction so that the entire surface has either a positive or negative charge).

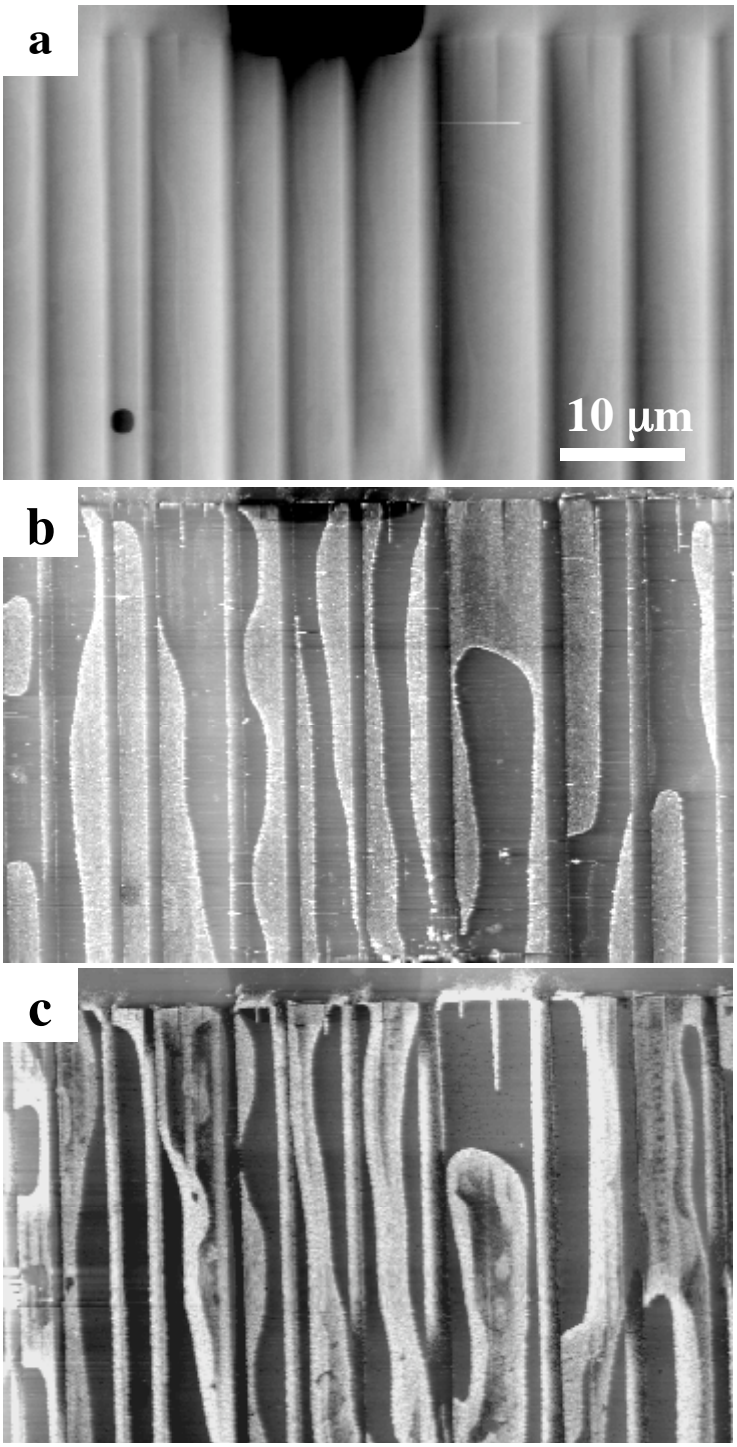


**Figure 2.17.** Topographic AFM images of the {001} surface of a $BaTiO_3$ single crystal. (a) Before the reactions. (b) The same area of the surface after illumination in an aqueous $AgNO_3$ solution. The white contrast corresponds to silver. (c) The same area of the surface after it was cleaned and illuminated in an aqueous lead acetate solution. The white contrast corresponds to lead containing deposits. The ranges of the vertical black-to-white contrast in (a) to (c) are 80 nm, 100 nm, and 110 nm, respectively. Reproduced from [12]

$BaTiO_3$ is typically an n-type semiconductor. In the previous section, it was mentioned that for n-type semiconductors, bands are generally bent upwards at the solid/electrolyte interface, and oxidation reactions are favored. However, from the experimental work presented above, it is apparent that both oxidation and reduction reactions were favored at different sites for the same material and that the preferred reaction was determined by the domain polarization. Thus, it appears that the ferroelectric polarization overwhelms any other charge effects from the solid/electrolyte interface. Hence, in contrast to other semiconductor materials, ferroelectrics can be used to promote both half reactions involved in water splitting.

Fig. 2.18 presents a plausible schematic for a ferroelectric based colloidal photocatalyst. As shown in the figure, electrons and holes created in the particle could be driven to different sites by the bulk photovoltaic effect. This schematic is experimentally supported by a previous work by Giocondi [59], in which the photochemical reactivity of ferroelectric $BaTiO_3$ microcrystals was investigated. Domain dependent reactivity was observed on the crystal surfaces. Furthermore, for single domain materials, oxidation and reduction reactions occurred on opposite sides of the crystal, suggesting that dipolar fields can separate charge carriers across particles.

So, unlike in non-ferroelectric semiconductors, charge carriers could be separated across the material, not just within the surface space charge layers. This has promising implications for particle photocatalysts. For non-ferroelectric particles, carriers that are photogenerated in the bulk (or driven into the bulk by space charge layers) have a greater likelihood of recombining because there is no charge separation in the bulk. This is important because significant numbers of carriers may be generated in the particle bulk.

Consider a 500 nm particle with a depletion layer width of 100 nm (a typical depth of space charge region as shown in Fig. 2.10). The percent of total carriers generated as a function of depth into the particle can be approximated using the Lambert-Beer Law, which predicts the light intensity at a certain depth into the particle:

$$I = I_0 \exp[-\alpha x] \qquad (2.7)$$

Where $\alpha$ is the absorption coefficient (material dependent), $I_0$ is the incident intensity of the light and I is the intensity at a depth of x. For $TiO_2$, $\alpha$ is $9x10^4$ /cm (at 360 nm) [47], so at a depth of 100 nm, the light intensity has decreased to around 40% of its initial value. So 40% of carriers are photogenerated at depths deeper than 100 nm into the material. Hence, a considerable amount of photogenerated carriers are created in the bulk. Thus, recombination of carriers created away from the space charge layers can cause marked decreases in efficiency.

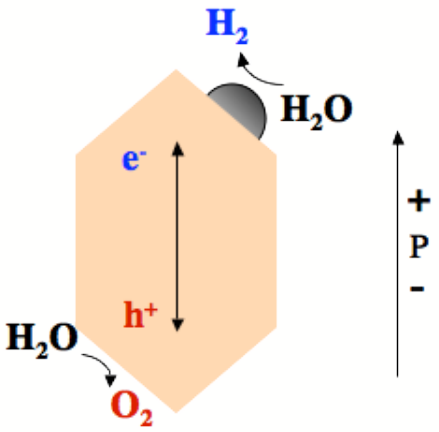


**Figure 2.18.** Schematic illustrating plausible charge separation in a ferroelectric particle photocatalyst.

## 2.5 Ferroelectric/Thin film heterostructures

As mentioned in Section 1.1, $BaTiO_3$ is susceptible to photocorrosion and therefore must be protected by a thin film of another material. $TiO_2$ was chosen as the film material because it is a well known photocatalyst with good photochemical stability and high photochemical activity. Furthermore, the conduction and valence band edges are in appropriate positions for water splitting.

In the previous sections, photochemical behavior for the separate cases of non-polar semiconductors and ferroelectric semiconductors was discussed. As these preceding sections have illustrated, band bending plays an essential role for photochemistry. Thus, in this section, we will address expected band structures for the case when non-polar semiconductors and ferroelectric semiconductors are combined, i.e. when of a ferroelectric semiconductor is coated with a thin film of $TiO_2$.

### *2.5.1 Semiconductor heterojunctions*

When any two dissimilar semiconductor materials come into contact, the energy bands for both materials are affected. If one of the materials is ferroelectric, energy bands will also be influenced by the dipolar field. First, we will ignore the contribution of the ferroelectric field and consider the interface as if it is between two non-polar semiconductors, which is the case, for example, when the dipolar field is aligned parallel to the surface. Heterojunction diagrams were constructed based on guidelines described in [60].

2.5.1.1 n/n heterojunctions ($BaTiO_3/TiO_2$ heterostructure)

Fig. 2.19 (a) shows the bulk, flat band positions for the conduction and valence band edges (relative to the vacuum level) for both $BaTiO_3$ and $TiO_2$ before they come into contact. The Fermi levels are drawn to reflect n-type conductivity, which is expected for both materials [43, 44, 61]. Also, for both materials, the Fermi level position is dependent on the position of the oxygen vacancy donor levels. For many oxides, the position of the donor levels is similar; typically they are 0.1-0.2 eV below the conduction band [62]. Thus, the distance between the Fermi level and conduction band is assumed to be the same for both materials. In (a), we see that the Fermi level of $BaTiO_3$ is at a higher energy than that of $TiO_2$. When the two materials are brought into contact, electrons from the $BaTiO_3$ flow into the $TiO_2$ (since electrons prefer to be at the lowest energy possible) until the Fermi levels of the two materials are equal. As a result, the near interface region in $BaTiO_3$ will be depleted of electrons (bands bend upwards) and the near interface region of the $TiO_2$ will have an accumulation of electrons (bands bend down). This is pictured in Fig. 2.19 (b). Additionally, in this figure, we see that there is a discontinuity (blue line) at the interface between the two materials. This discontinuity occurs because the two materials have different electron affinities, i.e their conduction band edges are at different positions relative to the vacuum level; $E_C$ for $BaTiO_3$ is 0.6 eV higher than $E_C$ for $TiO_2$. Thus the discontinuity represents the change in electron affinity as an electron moves from one material to the other. Similarly, the discontinuity at the valence band edges reflects that they are separated by 0.4 eV.

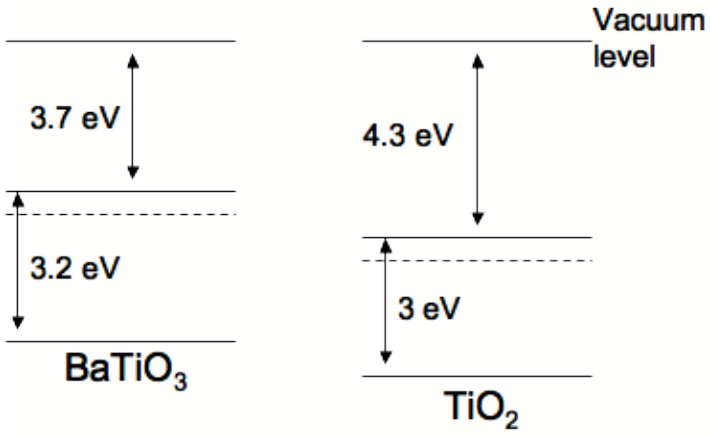


**(a)**

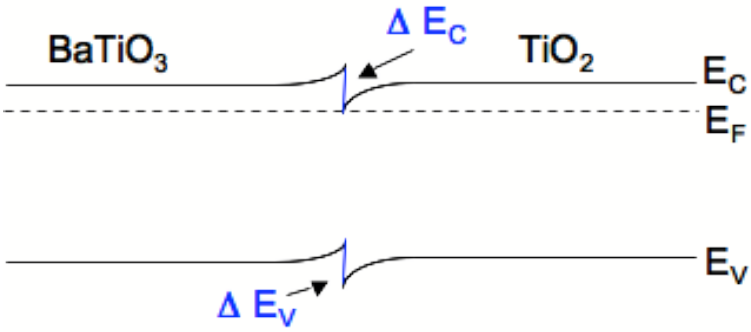


**(b)**

**Figure 2.19.** Energy band diagrams showing positions of energy bands in $BaTiO_3$ and $TiO_2$ (a) before contact and (b) after contact.

2.5.1.2 p/n heterojunctions ($BiFeO_3/TiO_2$ heterostructure)

In this section, energy diagrams for $BiFeO_3/TiO_2$ heterostructures will be presented. Again, the ferroelectric polarization will be ignored. For the $BiFeO_3/TiO_2$ heterostructure, the two materials have different conductivity types, i.e. $BiFeO_3$ is likely to be p-type and $TiO_2$ is n-type. $BiFeO_3$ is assumed to be p-type based on other works, in which p-type conductivity (from Bi vacancies) was observed in thin films [63, 64]. Fig. 2.20 (a) shows the bulk, flat band positions for the conduction and valence band edges

(relative to the vacuum level) for both $BiFeO_3$ and $TiO_2$ before they come into contact. The Fermi levels are drawn to reflect the conductivity type of each material. Similar to the case of the n/n heterojunction, charge carriers flow from one material to another to assume more favorable energy positions. $E_F$ is at a lower energy in p-type $BiFeO_3$, so electrons from the $TiO_2$ flow into $BiFeO_3$. Similarly, holes flow into $TiO_2$. This continues until electronic equilibrium is reached and $E_F$ is constant across the junction. On the $TiO_2$ side of the interface, bands are bent up to reflect electron depletion (fig. 2.20 (b)). For $BiFeO_3$, bands bend down to reflect hole depletion. As in the case of the n/n heterojunction, there are discontinuities at the junction to reflect the differences in $E_c$ (0.2 eV) and $E_V$ (0.1 eV).

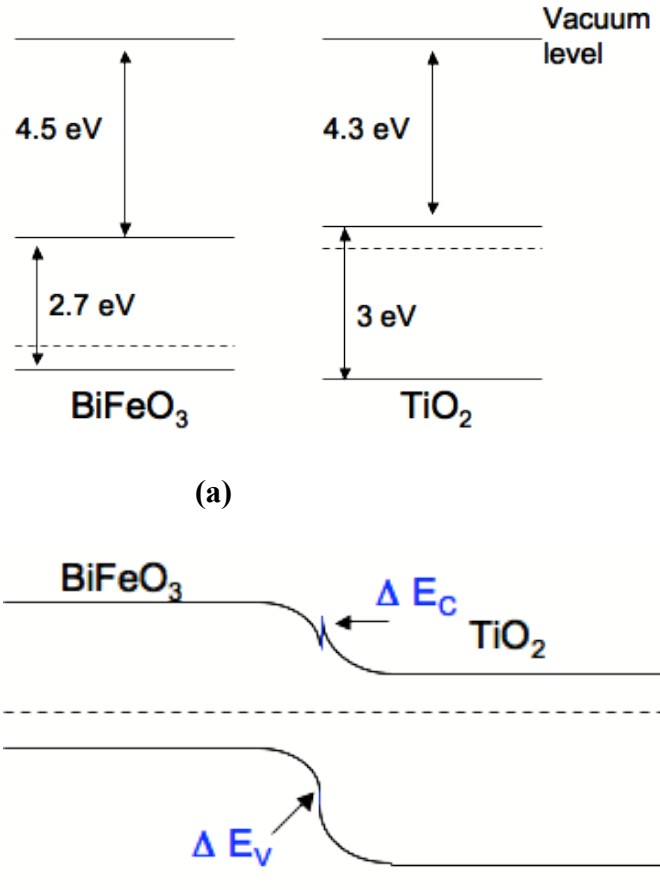


**Figure 2.20.** Energy band diagrams showing positions of energy bands in $BiFeO_3$ and $TiO_2$ (a) before contact and (b) after contact.

*2.5.2 Effect of polarization on band bending in the ferroelectric and $TiO_2$*

Now, we will discuss how polarization is expected to affect energy bands. In section 2.3, the effect of the dipolar field on the energy bands in a ferroelectric was discussed. Recall that at positive surfaces there is downward band bending (electron accumulation), while at negative surfaces there is upward band bending (electron depletion). Figure 2.21 shows the effect of ferroelectric polarizations on a contacting semiconductor. This schematic is based on the work of Wurfel and Batra [65] and their studies on ferroelectric TGS in contact with semiconducting electrodes. At the

ferroelectric-semiconductor interface, band bending is induced in the semiconductor by the polarization. When there is a negative charge from the spontaneous polarization, electrons in the semiconductor are repelled from the interface (upward bending of bands), and consequently, the positively charged, immobile donor cores are left behind to screen the excess interface charge. Similarly, a positive polarization charge results in an accumulation of electrons at the semiconductor side of the interface (downward bending of bands). Note that the effect of the excess charge on bands in both the ferroelectric and semiconductor is equivalent.

From the schematic we see that after some distance into the semiconductor, bands return to their equilibrium (unbent) state and the ferroelectric field is no longer felt by the semiconductor. For the depletion region, the depth of band bending into the semiconductor (thickness of semiconductor material needed to screen the charge) is predicted by Poisson's equation:

$$\frac{d^2V}{dx^2} = \frac{qN_{SC}}{\varepsilon} \qquad (2.8)$$

where V is the voltage at the interface (for example, from polarization), ε is the dielectric constant, q is the elementary charge and $N_{SC}$ is the density of compensating charge in the space charge layer (ex. for $TiO_2$, $N_{SC}$ is equal to the density of oxygen vacancies and is equivalent to the concentration of conducting electrons).

Integrating (twice) we get:

$$V = \frac{qN_{SC}}{\varepsilon}(x - x_0)^2 \qquad (2.9)$$

If x is defined as zero at the interface and $x_0$ is defined as the depth where the field is screened completely, then the depth of band bending, w, is given by:

$$w = \left( \frac{2V\varepsilon}{qN_{SC}} \right)^{1/2} \qquad (2.10)$$

This model suggests that as long as the film has not completely screened the polarization charge (film thickness < w), the ferroelectric field will still impact energy bands at the surface of the semiconductor film.

For the accumulation region, the Poisson equation has to be modified to account for charge screening by mobile charge carriers. Remember that for depletion, majority carriers, i.e. electrons in an n-type material, are depleted from the interface so charge compensation must come from immobile donor cores, which have a fixed concentration. For accumulation, mobile majority carriers can move to the interface to screen the charge; their contribution to charge screening is predicted by Boltzmann statistics. The Poisson equation becomes:

$$\frac{d^2V}{dx^2} = \left( \frac{qn_{bulk}}{\varepsilon} \right) \left[ \exp(-qV/kT) - 1 \right] \qquad (2.11)$$

where $n_{bulk}$ is the bulk density of electrons. For depletion, charge compensation is dependent on the concentration of immobile charge (charge carriers). For accumulation, charge can move to the region of excess charge, so larger compensating charge concentrations can be achieved. Hence accumulation layers are typically shorter and band bending is steeper.

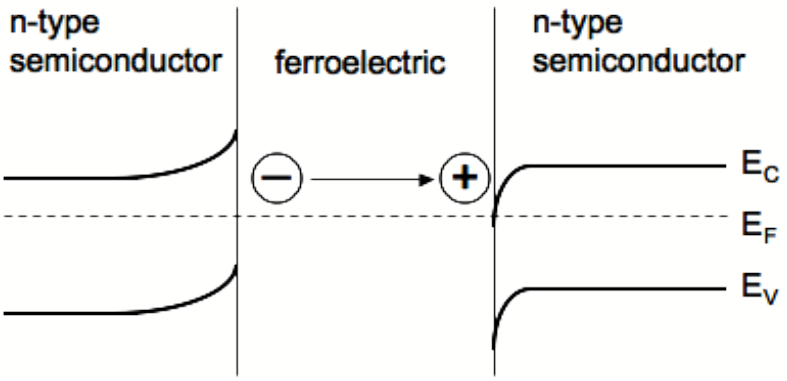


**Figure 2.21.** Schematic illustrating the impact of polarization from a ferroelectric material on a contacting n-type semiconductor.

*2.5.3 Ferroelectric/Semiconductor Heterojunctions*

Using the information from the previous sections, we can now construct an energy band diagram for the $BaTiO_3/TiO_2$ heterostructure that includes the contribution of both polarization and junction formation. Figure 2.22 shows expected energy band diagrams for the $BaTiO_3$/ $TiO_2$ junction for three different cases: no polarization at the interface, the positive end of the polarization dipole at interface and the negative end of the dipole at interface. These diagrams are based on models of ferroelectric/semiconductor heterostructures proposed by Watanabe [66, 67]. The non-polar case was discussed in Section 2.4.1. Fig. 2.22 (b) shows the effects of positive

polarization charge. Initially bands in the $BaTiO_3$ bend up at the interface, while bands in the $TiO_2$ bend down. The addition of a positive charge at the interface will cause electrons from both materials to accumulate at the interface. For $TiO_2$, accumulation will cause an increase in the downward band bending. For $BaTiO_3$, the effects of the polarization and junction formation counteract one another, thus depending on their relative contributions, bands may bend up to a lesser extent (not pictured) or they may bend downward (2.22 (b)). Similar arguments can be made for negative charge at the interface. Figure 2.23 shows energy band diagrams for the $BiFeO_3/TiO_2$ heterostructure for the same three cases. These diagrams are drawn using the same reasoning as for the $BaTiO_3/TiO_2$ heterostructure.

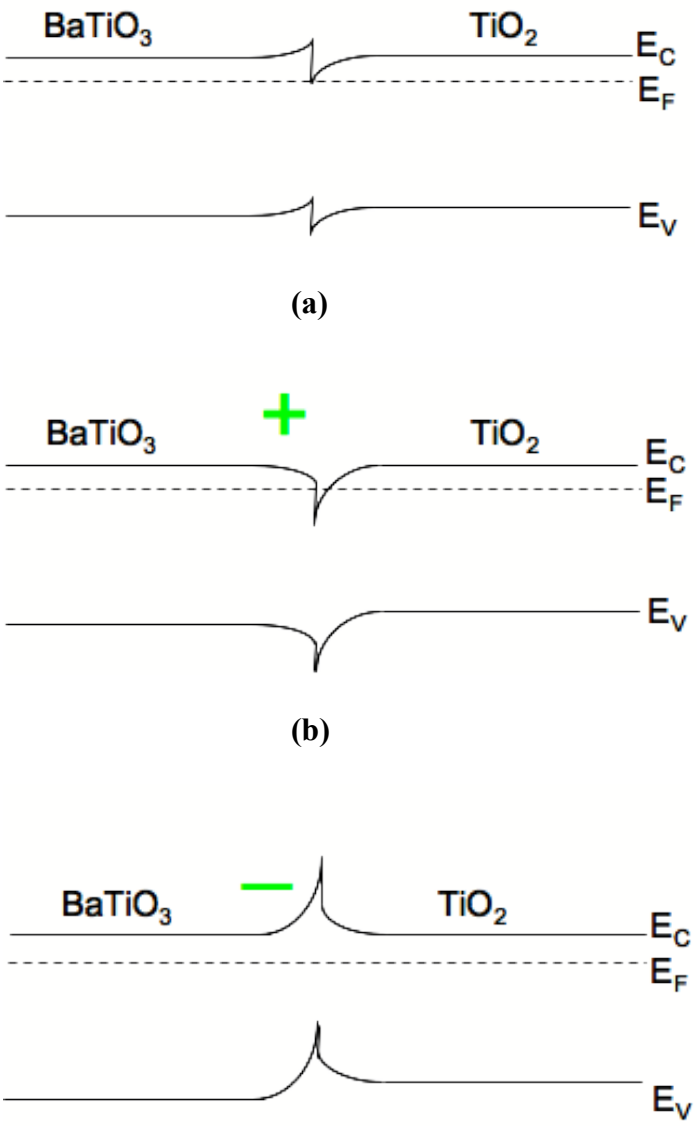


**Figure 2.22.** Band diagrams showing the effects of (b) positive and (c) negative polarization on the $BaTiO_3/TiO_2$ heterostructure (a).

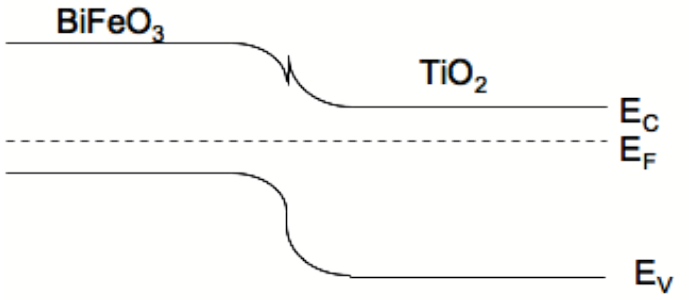


**(a)**

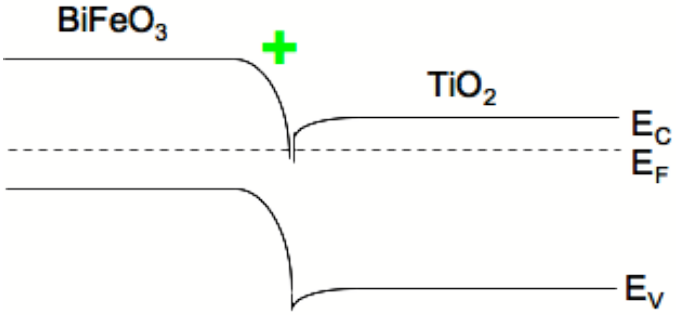


**(b)**

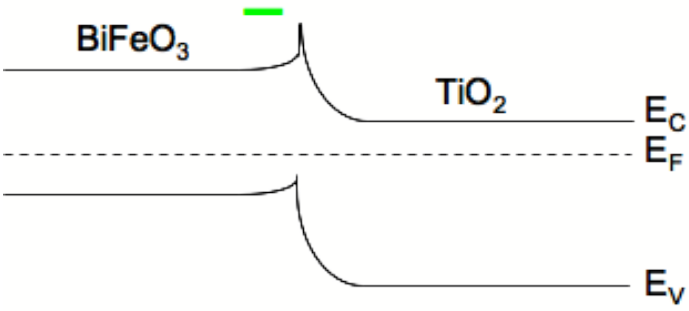


**(c)**

**Figure 2.23.** Band diagrams showing the effects of (b) positive and (c) negative polarization on the $BiFeO_3/TiO_2$ heterostructure (a).

*2.5.4 Ferroelectric/semiconductor Heterostructures and photocatalysis*

Experimentally, previous works have suggested that dipolar fields in ferroelectric materials can influence the photocatalytic activity of contacting materials [17, 68, 69]. For example, enhancement in $H_2$ evolution was observed when ferroelectric tourmaline powder was mixed in with titania powder photocatalysts [68]. Increased activity of the $TiO_2$ was attributed to enhanced separation between electrons and holes because of the presence of the electric field from the particles.

Previous works by Inoue et al. [69] have suggested that poled ferroelectric substrates can influence the photocatalytic activity of thin semiconducting films. In one study, $TiO_2$ films were grown on $LiNbO_3$ poled substrates. Photocatalytic activity was enhanced for films on polar substrates as compared to films grown on non-polar substrates. The effect of the polar substrates was observed to be dependent on the thickness of the film. For film thicknesses of around 20 nm, films grown on polar substrates and those grown on non-polar substrates exhibited similar photocatalytic activity. However, with increasing film thickness, the difference in photocatalytic activity increased significantly until a maximum in the difference was reached at a film thickness between 100-150 nm. After this maximum was passed, the difference decreased up to a thickness of around 200 nm, at which point the difference in photocatalytic activity between films gown on polar and non-polar substrates was again insignificant.

In another study, ferroelectric $LiNbO_3$ was observed to influence the surface conductivity of a p-type NiO film [17]. The surface conductivity was observed to be higher for thin films deposited on positive polar substrates than for films deposited on negative polar substrates. These observations were explained using the model by Wurfel

and Batra [65]. As shown in Fig. 2.24, the ferroelectric $LiNbO_3$ induces band bending in the NiO film and because the film is thinner than the space charge region, the band bending extends to the film surface. Hence, the positive $LiNbO_3$ polarization promotes hole transport to the NiO surface, while the negative $LiNbO_3$ polarization promotes electron transport to the film surface. As the NiO was p-type (holes were the majority carrier), a greater surface conductivity was observed for the positive polar substrate. As film thickness was increased, the difference in film surface conductivity between the positive and negative poled substrates diminished. This analysis suggests that for films that are thin enough, polarization induced band bending is present at the film surface and charge carriers photogenerated in the film will be preferentially driven to domain dependent locations on the surface. This implies that domains from ferroelectric substrates could still promote specific half reactions on thin film surfaces.

In the work of Inoue et al. [17], only one type of domain polarization (i.e. negative or positive) was present at a time, so the effect of having both half reactions promoted simultaneously at different locations was not studied. Additionally, the domain polarization was not directly correlated with the reaction location on the film surface. In the current work, both types of domain polarizations will be present and the site of the reaction will be correlated with the domain structure.

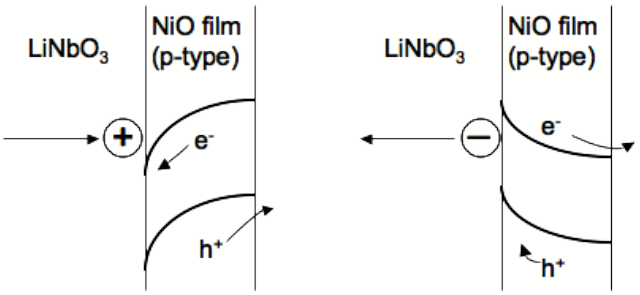


**Figure 2.24.** Figure from a study by Inoue et. al. explaining higher surface conductivity for a NiO film grown on top of a positively poled ferroelectric surface. Redrawn from [17].

*2.5.5 Effect of Thin films*

In the preceding sections, the ability of a ferroelectric to induce band bending in a film was discussed. The work of Inoue et al. [17] described above suggests that band bending in thin films may be essential in creating spatially localized reactions on thin film surfaces. However, based on theoretical predictions of the band bending possible in small particles, we expect that for very thin films, band bending in the $TiO_2$ will be small compared to a very thick film or bulk material [70]. Consider the schematic in Fig. 2.25. Figure 2.25 a shows a bulk n-type semiconductor in contact with a solution. Here, bands bend up at the interface and then return to equilibrium at some point in the material. Fig. 2.26 shows a small particle (n-type) in contact with the solution. This contact results in the formation of depletion layers in the particle at both solid-solution interfaces. The width of these depletion layers depend on donor density, dielectric constant and temperature. The Poisson equation is a description of the dependence. If the particle is much smaller than the required depletion width, then the full extent of band bending will not occur inside the particle and the entire particle will be depleted of carriers.

Applying these considerations to thin films, it is possible that the thinnest films will not be able to accommodate the full extent of band bending necessary to screen the

charge. For example, on one side of the thin film, carriers will screen the polarization charge from the ferroelectric. For $BaTiO_3$, we know that the surface polarization charge is 26 $\mu C/cm^2$. For a depletion layer, the width of material needed to screen this charge can be predicted by balancing the charge introduced by the ferroelectric with the compensating charge in the semiconductor:

$$P_S = qN_{SC}w \qquad (2.12)$$

where, $P_S$ is the charge from polarization and $N_{SC}$ * q * w is the amount of compensating charge for a semiconductor depth of w. $N_{SC}$ is the density of compensating charge (oxygen vacancies) in the semiconductor and is equivalent to the electron concentration and q is the elementary charge. Solving for w, we get:

$$w = \frac{P_S}{qN_{SC}} \qquad (2.13)$$

As the equation shows, depletion width is inversely proportional to the carrier concentration, so depletion widths will be shorter for higher carrier concentrations. Since the charge is compensated in a smaller region, band bending is also expected to be steeper for higher carrier concentrations.

Using a reasonable estimate of carrier concentration for $TiO_2$ of $n=1x10^{18}$ -$1x10^{19}$ $/cm^3$ [71], the depletion width would be between 1620 and 162 nm. It is likely that the $TiO_2$ does not compensate all of this charge, since charge can also be compensated by interface states or by carriers in $BaTiO_3$. However, in this study, film thicknesses range

from 10 nm to 100 nm so it is likely that the depletion layer will still be much greater than the thickness of the thinnest films (10-15 nm) and consequently, that band bending in these films will be smaller than in bulk materials. Experimental observations of photochemical reactions on thin films supported by ferroelectric substrates are discussed in detail in Chapters 5 and 7.

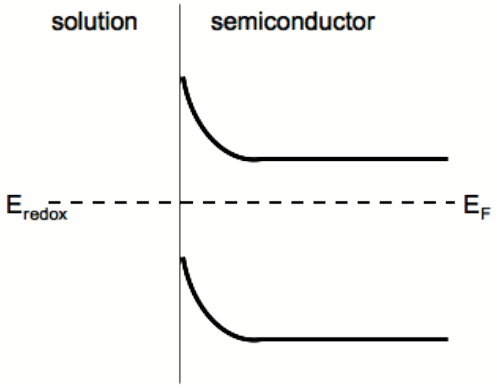


**Figure 2.25.** Band bending at the solution/electrolyte interface for a bulk material. Redrawn from [70]

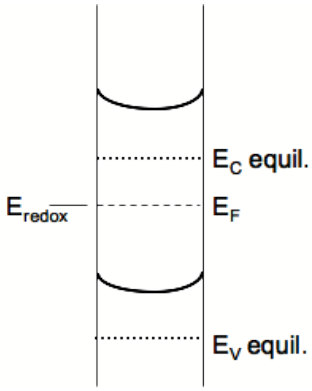


**Figure 2.26.** Band bending at the solution/electrolyte interface for a small particle. Redrawn from [70]

## 2.6 Other factors affecting photochemical reactivity of the heterostructure

### *2.6.1 Orientation of $BaTiO_3$*

The orientation of $BaTiO_3$ may influence spatially selective reactivity. One important difference between different orientations is the alignment of the polarization vector. Recall that for $BaTiO_3$, polarization can occur in any of the <100> directions. The polarization vector is then only normal to the surface for {100} orientations of $BaTiO_3$. For a polycrystalline sample this will not always be the case (see Fig. 2.27). Some grains will be oriented so that the polarization vector (for reactive domains) is normal, or close to normal, to the surface (grain 1), while others (grain 2) will have their polarization vector at a considerable angle to the surface. When the polarization vector is closer to normal, a larger component of the field should reach the surface and the effect of spatially selective reactivity should be enhanced.

However, it has also been shown that the dielectric constant of $BaTiO_3$ varies with crystal orientation [72]. The dielectric constant increases as the crystal is rotated away from the <001> spontaneous polarization direction and reaches a maximum at around 50° away from <001>. Since a higher dielectric constant correlates to an increase in the space charge depth (see eq. 2.10), the ability of a specific crystal orientation to separate charge (and consequently, to spatially localize reaction products) may be affected by this.

In a study of reaction behavior of faceted $BaTiO_3$ crystals, anisotropic reactivity was observed [59]. Some crystal faces had a higher reactivity than others. The reactivities were ranked from highest to lowest as follows: {100} > {111} > {110}. The significance of substrate crystal orientation for spatially selective reactivity is detailed in Chapter 10 of this document.

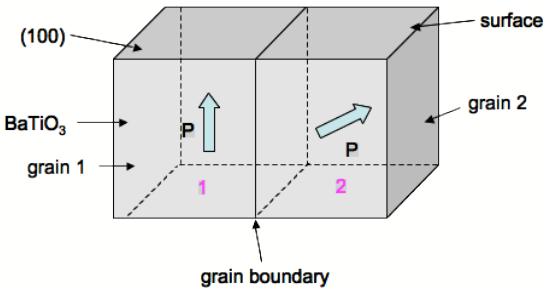


**Figure 2.27**. Schematic of polarization vectors in a polycrystalline sample. Domains 1 and 2 are shown to lie in grains of different orientations.

### *2.6.2 Orientation/phase of $TiO_2$*

Since polycrystalline samples are being used, the $TiO_2$ film is also expected to be polycrystalline. If film growth is epitaxial, then there will be a correlation between the orientation of the substrate and that of the film. This orientation relationship exists because the film-substrate interface energy is minimized when the substrate and film are closely lattice matched. In addition, for the film growth temperature used in this research (700°C), it is possible for two different phases of $TiO_2$, rutile or anatase, to form. The crystal structures of both are shown in Fig. 2.28. Lattice constants for rutile are a = 4.5941 and c = 2.9589 and lattice constants for anatase are a = 3.7845 and c = 9.5143 [37]. As in the case of orientation, a certain phase of film could be preferred for each substrate orientation.

Previous work has been done to obtain the epitaxial relationship between $TiO_2$ and $BaTiO_3$ as well as between $TiO_2$ and $SrTiO_3$ for certain crystal orientations [41-46]. $SrTiO_3$ has the same crystal structure as $BaTiO_3$ and the lattice constants are similar (for $BaTiO_3$, a = 3.98 Å, c = 4.03 Å; $SrTiO_3$, a=3.905 Å), so orientation relationships between $SrTiO_3$ and $TiO_2$ expected to be similar to those obtained for $BaTiO_3$ and $TiO_2$. The results obtained in these studies are summarized below. The epitaxial relationship

between{100} $SrTiO_3$ and {001} anatase $TiO_2$ is well established for temperatures up to 1000°C [73-76]. Epitaxial relationships for other orientations are presented in a study of $SrTiO_3$ and $BaTiO_3$ thin films deposited by vapor-solid reactions on (100) and (110) rutile single crystals [77, 78]. For (100) rutile and $SrTiO_3$ at reaction temperatures ranging from 700-900° C, (111) $SrTiO_3$ was the dominant film orientation. At 800° C, the (551) $SrTiO_3$ orientation was also present and at 900°C (112) and (558) $SrTiO_3$ were also formed. For (100) rutile and $BaTiO_3$ at temperatures between 600°-900°C, (111) $BaTiO_3$ was the primary film orientation, which is consistent with results for $SrTiO_3$. (112) $BaTiO_3$ was also formed at 800°C. For (110) rutile and $SrTiO_3$ at 700° C, both (110) and (118) $SrTiO_3$ were formed. For (110) rutile and $BaTiO_3$ at 700°C, the main orientation of the film was (001) $BaTiO_3$ which is discordant with the results obtained for $SrTiO_3$. However, at higher temperatures (800°-900°C), the (110) and (119) orientations $BaTiO_3$ also formed on (110) rutile. These results are similar to those obtained for $SrTiO_3$.

Both film phase and orientation could influence reactivity. In general, anatase is believed to be more reactive than rutile. This has been attributed to the Fermi level of anatase being higher than that of rutile by about 0.1eV [79]. Orientation is expected to influence reactivity since $TiO_2$ has been previously observed to have an anisotropic photochemical reactivity [80-85]. The anisotropic reactivity of $TiO_2$ as demonstrated by Lowekamp is presented in Fig. 2.28 [83]. Figure 2.29 (a) shows an AFM image of polycrystalline bulk $TiO_2$. Several grains of different orientation are present in the image. In (b), an AFM image of the same location after photochemical reaction is presented. Here, the white contrast indicates the presence of insoluble reaction products,

which are clearly present in greater amounts on some of the grains. Lowekamp quantified and compared the relative reactivities of a variety of orientations and showed the results on a standard stereographic triangle for rutile. In Fig. 2.30, the results illustrate that the most reactive orientations are near {111}, {001} and {011}. A similar study of $TiO_2$ thin films confirmed that the {001}, {101} and {111} faces were more reactive for the photochemical reduction of $Ag^+$ to Ag than the {100} and {110} faces [81].

There are several possible explanations for the orientation dependent reactivity of $TiO_2$. One explanation is that different orientations exhibit differences in surface morphology (surface area, Ti site density and coordination, amount and orientation of facets) that affect reaction behavior and thus cause an anisotropic reactivity [81]. Differences in surface chemistry (ex. mechanisms of adsorption and desorption) could also play a role. Variance in electrical properties of different surfaces is another possible explanation. For example, the energy required for carrier photogeneration is different for carriers with different wave vectors. Hence, it is easier to excite carriers that are traveling in certain directions. In this case, reaction is favored for orientations that are normal to these directions. Similarly, carrier mobility has been demonstrated to differ for different crystal directions. For example, for rutile titania, Hall mobility of photogenerated electrons is greater along the [001] direction than along the [100] [86]. Photochemical reactivity could be enhanced for surfaces perpendicular to directions with high carrier mobilities. Thus, the reasons for the anisotropic reactivity are not fully understood.

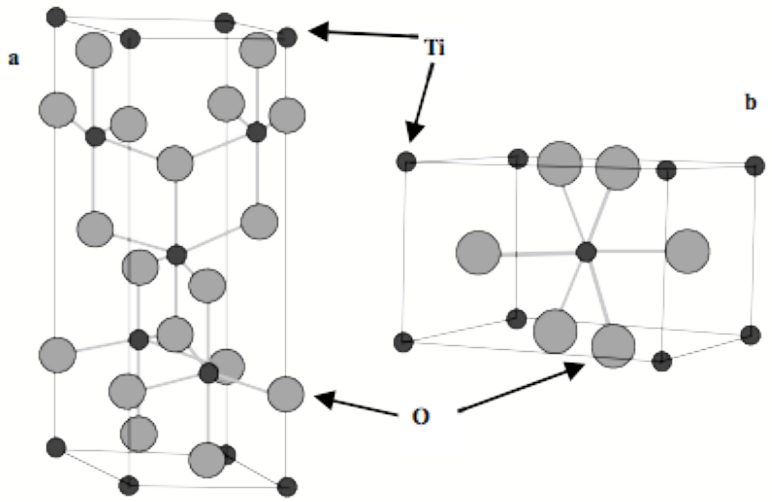


**Figure 2.28.** The crystal structures of (a) anatase and (b) rutile. Reproduced from [83].

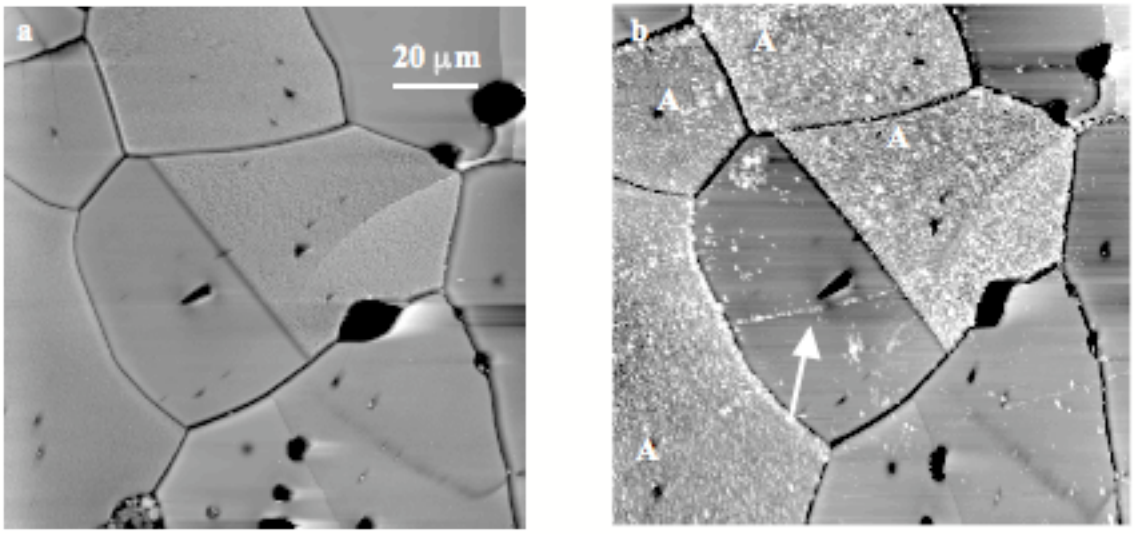


**Figure 2.29.** Images illustrating the anisotropic reactivity of $TiO_2$. (a) is an AFM image of the surface of $TiO_2$ before reaction. (b) shows the surface after reaction in silver nitrate solution. In image b, the arrow points to a polishing scratch and grains with higher reactivity are marked with an "A". Reproduced from [83]

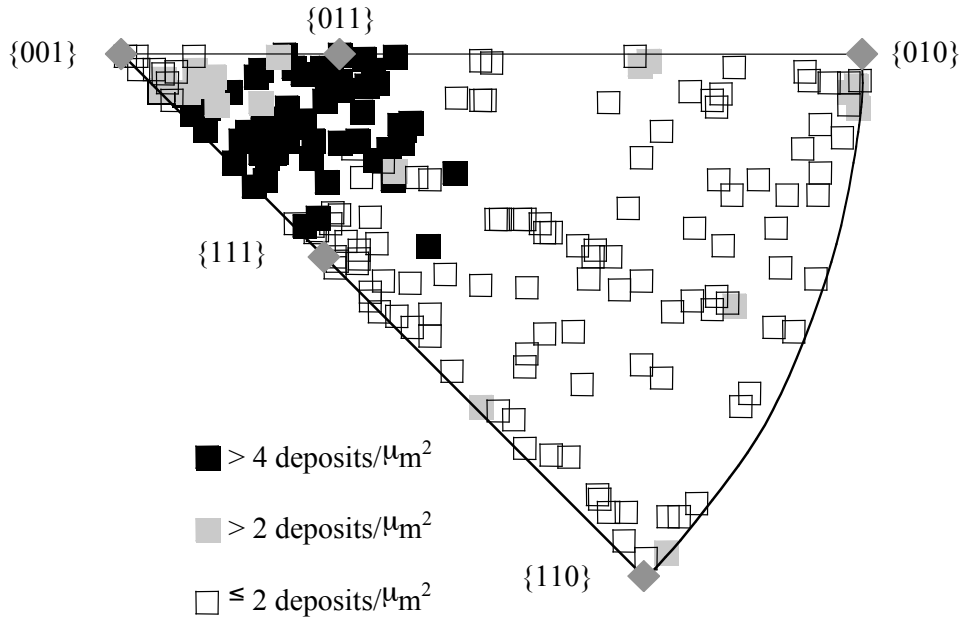


**Figure 2.30.** Photocatalytic activity versus orientation. Reproduced from [83].

# 3 Experiment

## 3.1 Substrate Preparation

### *3.1.1 $BaTiO_3$ preparation*

$BaTiO_3$ polycrystalline substrates were prepared from $BaTiO_3$ powder (Alfa Aesar, 99.7%). After grinding, the powder was uniaxially compressed under approximately 230 MPa to form cylindrical pellets with thicknesses ranging from 2 mm to 5 mm and a diameter of 11 mm. The pellets were then placed in an alumina crucible along with some excess $BaTiO_3$ powder to ensure that the pellets did not contact the crucible. Pellets were first heated to 900°C for 10 hours to remove any residual organics, then sintered at 1230°C for 10 hours, and finally heated to 1360°C to grow the grains to an average size of around 50 μm. After sintering, pellets were lapped flat using 9 μm $Al_2O_3$ aqueous solution (Buehler) and polished with a 0.02 μm colloidal silica solution (Buehler). Samples were then thermally etched at 1200°C for 4 hours.

Figure 3.1 shows images of $BaTiO_3$ substrates prepared using the procedure detailed above. Typical features of the $BaTiO_3$ microstructure are marked in the images.

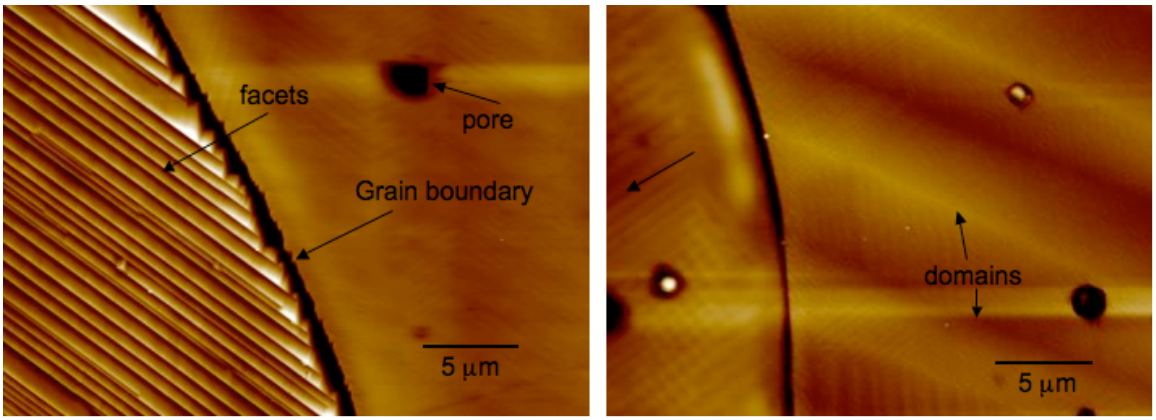


**Figure 3.1.** AFM images of polycrystalline $BaTiO_3$. Black-to-white contrast=70 nm

### *3.1.2 $BiFeO_3$ preparation*

$BiFeO_3$ polycrystalline substrates were prepared by combining stoichiometric amounts of $Bi_2O_3$ (Alfa Aesar, 99.99%) and $Fe_2O_3$ (Alfa Aesar, 99.945%) powders. The powders were mixed by ball milling for 24 hours in ethanol. The mixed powder was dried and then heated in an alumina crucible at 650°C for 1 hr [87]. The powder was then ball milled again for 24 hours, dried, and uniaxially compressed (under 230 MPa) to form cylindrical pellets with a diameter of 11 mm. Pellets were sintered at 850°C for 2 hours and polished using the procedure described above for $BaTiO_3$.

Figure 3.2 shows an AFM image of a $BiFeO_3$ substrate prepared using the procedure detailed above. Typical features of the $BiFeO_3$ microstructure are marked in the image.

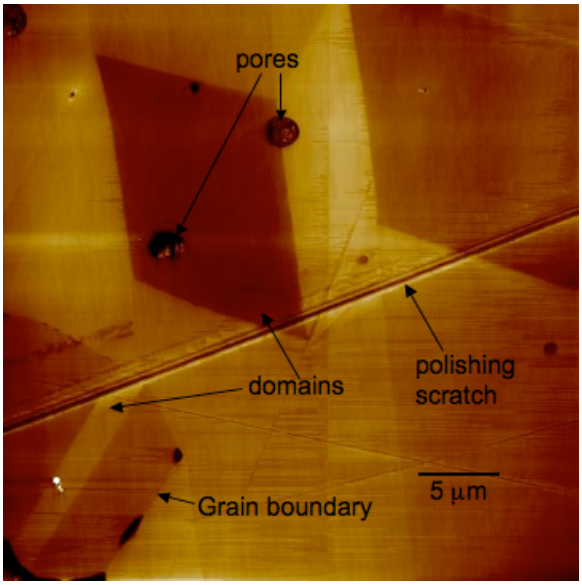


**Figure 3.2.** AFM image of polycrystalline $BiFeO_3$. Black-to-white contrast =40 nm

## 3.2 Thin Film Growth

### *3.2.1 Pulsed Laser Deposition (PLD)*

Thin films of $TiO_2$ were grown using a Neocera PLD system with a KrF laser ($\lambda$ =248 nm) operating at a frequency of 3 Hz and at an energy density of 2 J/cm$^2$. A schematic of the setup of the PLD chamber is presented in Fig. 3.3. The target to substrate distance was maintained at 6 cm for all experiments. A base pressure of $10^{-6}$ Torr was established at room temperature before heating to 700°C and depositing for times ranging from 5 min to 90 min. All films were cooled to room temperature in a static pressure of 5 Torr of $O_2$. Because film deposition rates were inconsistent, film thicknesses were determined using X-ray reflectivity (explained in more detail in Section 3.3.1). Since polycrystalline samples cannot be used for this technique, X-ray reflectivity was instead performed on single crystal $SrTiO_3$ substrates that were placed next to the sample during film growth. Figure 3.4 shows an AFM image of a $TiO_2$ film deposited on $BaTiO_3$. The film inherits the topography of the substrate so the film surface looks similar to the $BaTiO_3$ surface.

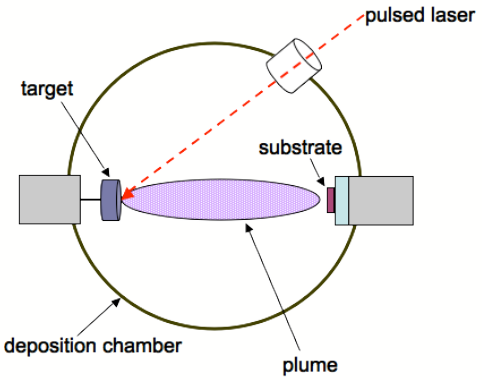


**Figure 3.3.** Schematic of PLD setup. A pulsed laser ablates the surface of a target (composed of the film material) and a plume of ablated material is directed towards the surface of the substrate, which is heated to a certain temperature.

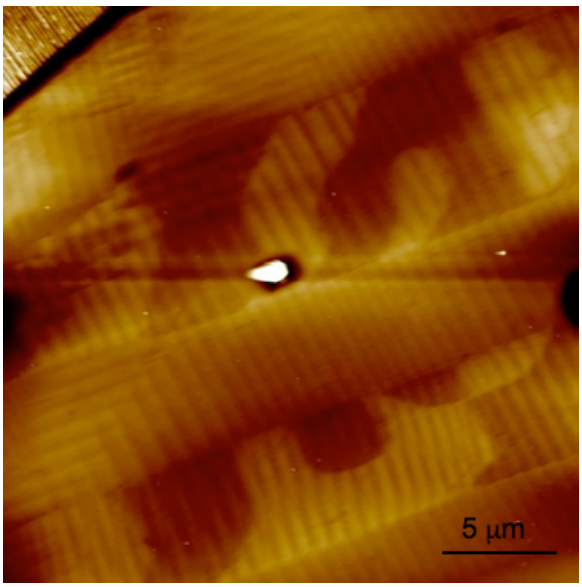


**Figure 3.4.** AFM image of $TiO_2$ film on $BaTiO_3$. The film inherits the topography of the substrate. Black-to-white contrast=70nm

### *3.2.2 Target Preparation*

For undoped films, the PLD target was prepared using $TiO_2$ powder. To produce doped films, the target was prepared by adding a specific amount of $Nb_2O_5$ to the $TiO_2$. The $Nb_2O_5$ introduces n-type conductivity in accordance with the following equation [43].

$$Nb_2O_5 = 2Nb_{Ti}^{\bullet} + 4O_O^{*} + 1/2O_2 + 2e- \qquad (3.1)$$

Where $Nb_{Ti}^{\bullet}$ represents a substitutional Nb ion on a Ti site, $O_O^{*}$ is an oxygen ion on an oxygen site and $e^-$ is an electron in the conduction band. Based on the amount of impurity added (and assuming full ionization), the carrier concentration in the doped films is estimated to be $3X10^{20}/cm^3$, which is expected to exceed the intrinsic carrier concentration [71].

After wet (in ethanol) and dry grinding, powders were uniaxially compressed under 175 MPa to form cylinders with a diameter of 1 inch. The targets were sintered in an alumina crucible at 1600°C for 24 hours. After sintering, the undoped targets appeared yellow in color and the doped targets were dark blue. Test films were grown on $SrTiO_3$ single crystal substrates and X-ray diffraction was conducted to confirm that the films were, in fact, $TiO_2$.

## 3.3 Sample Characterization

### *3.3.1 Film Thickness*

An X'Pert diffractometer was used to conduct X-ray reflectivity on $SrTiO_3$ single crystal substrates that were placed near samples during film deposition. In this technique, a beam of x-rays strikes the surface at low angles and is reflected at both the film surface and the film-substrate interface. The two reflected rays constructively and destructively interfere with one another to form a beam with a new intensity. As the angle is varied, the intensity of the reflected beam changes and an intensity vs. angle ($2\theta$) plot can be

generated. An example of a typical reflectivity scan is shown in Fig. 3.5. As illustrated by the plot, the variations in interference with incident angle cause periodic oscillations in the curve. The frequency of the oscillations is dependent on the film thickness, so the thickness can be determined from the oscillation frequency. [88, 89]

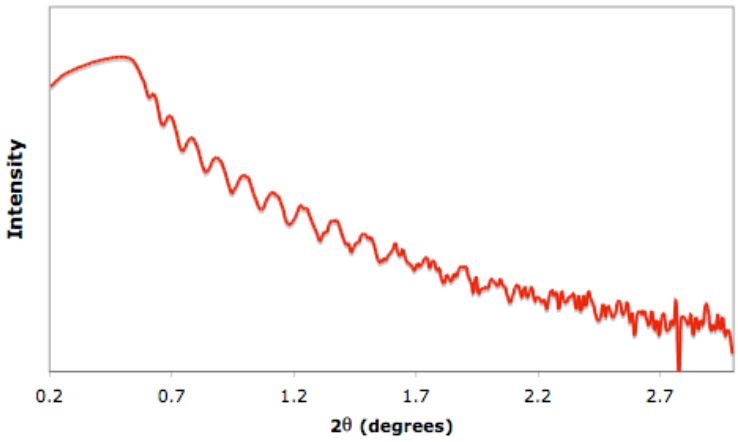


**Figure 3.5.** Reflectivity scan of a $TiO_2$ film grown on a $SrTiO_3$ single crystal substrate.

### *3.3.2 Grain Orientation of Substrate and Film*

Orientations of film and substrate grains were determined using electron backscatter diffraction (EBSD) patterns [90]. Patterns were acquired and analyzed using a XL40FEG SEM with TSL OIM (Orientation Imaging Microscopy) data collection and analysis software. EBSD patterns are generated by the interaction between the electrons and the crystal. This interaction is maximized if the sample is tilted so that its surface normal is 70° from the electron beam. The electrons interact with the sample and some electrons undergo backscatter diffraction. These diffracted electrons intersect with a phosphor screen and a pattern is formed. The pattern consists of a number of bands that correspond to the lattice planes from which the electrons diffracted. Each pattern is

characteristic of a specific crystal orientation, so it can be used to determine the crystallographic orientation of the region of the surface from which it was generated. EBSD patterns can be matched to their crystallographic orientation using TSL OIM software. Typical imaging conditions were: working distance = 10 mm, spot size = 5 or 6, and accelerating voltage = 20-30 kV.

An example of an EBSD pattern obtained from a $BaTiO_3$ substrate is shown in Fig. 3.6. The TSL software collects and indexes many patterns across a specific region of the sample to produce an orientation map, such as the one pictured in Fig. 3.7. Here, the grains on a $BaTiO_3$ sample are mapped according to the orientation of the surface normal of the grain. Typical accuracies for orientations are within 5°. In this thesis, grains are identified by the orientation of the low-index surface normal that is within 5° of their surface normal. For example, grains referred to as being of the "{100} substrate orientation" have a surface normal that is a maximum of 5° away from the <100> direction.

To determine the relationship between film and substrate orientation, previously indexed substrate grains were relocated and EBSD patterns were obtained for the films that formed on top of them. Compared to the substrate, bands in EBSD patterns obtained from the films were far less pronounced. Consequently, the TSL software was not able to produce an accurate orientation map for a large region of the sample. Instead, patterns were obtained and analyzed one by one for particular spots on the film surface. In this manner, the bands in each pattern could be maximized using image processing tools. Additionally, multiple patterns obtained from the same spot could be averaged to produce a better quality image of the pattern, making the pattern easier for the software to index.

An image of an EBSD pattern (after processing and image averaging) acquired from a $TiO_2$ film is presented in Fig. 3.8. The patterns were then identified individually by the TSL software to obtain the local crystallographic orientation. The relationship between substrate and film orientation is discussed in detail in Chapter 4. For each grain that was examined, at least 15 patterns were acquired from different spots on the grain. For all the grains examined, patterns from the film were consistent across the grain. It should be noted that the software offers several possible matches for each pattern. The user then chooses the best match.

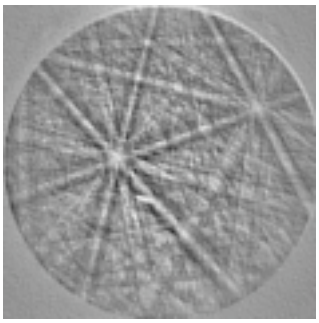

**Figure 3.6.** EBSD pattern from $BaTiO_3$ substrate.

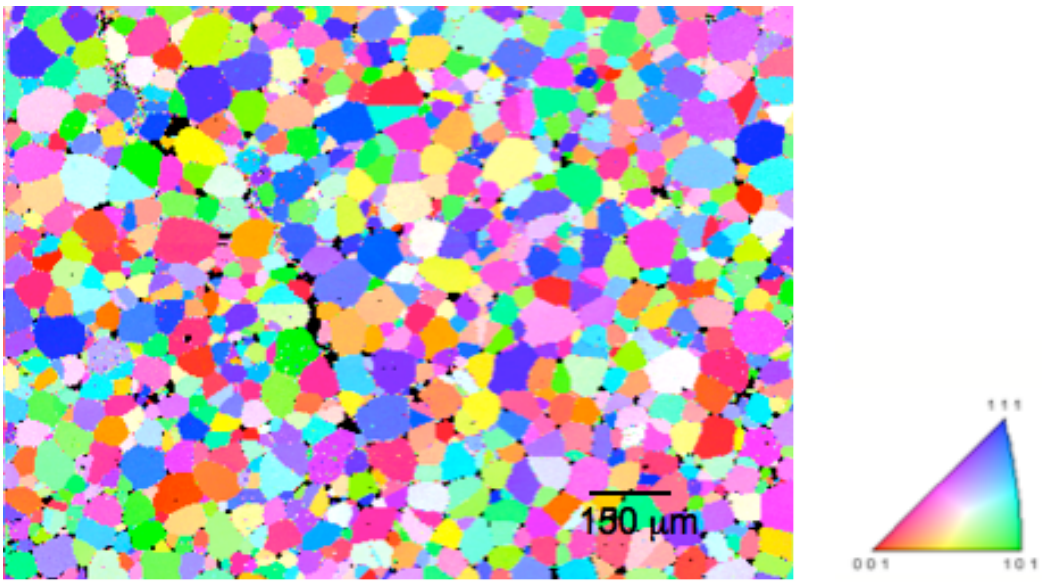


**Figure 3.7.** Orientation map generated for the substrate.

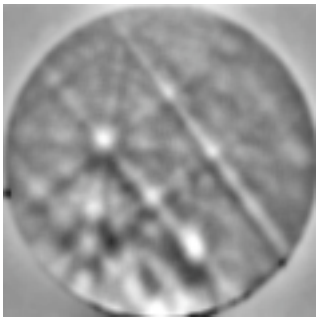

**Figure 3.8.** EBSD pattern from the $TiO_2$ film.

## 3.4 Photochemical Reactions

To determine whether reduction and oxidation reaction sites are spatially separated, it is necessary to perform photochemical reactions on the surface of the $TiO_2$ films. For this study, the photochemical reactions being used are:

$$Ag^+ + e^- = Ag \qquad (3.2)$$

$$Pb^{2+}\, 2H_2O + 2h^+ = PbO_2 + 4H^+ \qquad (3.3)$$

Reaction (1) is used to ascertain the location of the reduction half reaction and reaction (2) is used to determine the location of the oxidation half reaction. Both of these reactions leave insoluble products on the surface, and thus the reaction location is easy to identify [91-94]. $Ag^+$ ions are provided by a 0.115M $AgNO_3$ solution and $Pb^{2+}$ ions will come from a 0.0115M $Pb(C_2H_3O_2)_2$ solution. It should be noted that each of these reactions only represents half of the total redox reaction. To maintain charge neutrality, reduction half reactions must occur concurrently with oxidation half reactions. Furthermore both must occur at the same rate so that as electrons are produced by oxidation, they are consumed by reduction so that there is no net charge buildup on the surface. For the reduction half reaction ($Ag^+$ to Ag), the most likely complementary

reaction is the oxidation of $H_2O$. For the oxidation half reaction the complementary reaction is likely to be the reduction of $O_2$. Both complementary reactions are "invisible", i.e. they do not produce reaction products that are detectable through AFM.

The experimental setup is depicted in Fig. 3.9. An O-ring is placed on top of the surface and filled with either aqueous $AgNO_3$ or $Pb(C_2H_3O_2)_2$. A 300 W Hg lamp is used to shine UV light onto the sample, which generates charge carriers in the sample and allows photochemical reactions to occur on the surface. Exposure times for the reduction of silver ions are 3 seconds for reactions on bare substrates and 10 seconds for reactions on film surfaces. Exposure times for the oxidation of lead ions are 180 seconds for bare substrates and 270 seconds for film surfaces. For some experiments in this thesis, $Ag^+$ reduction and $Pb^{2+}$ oxidation are both carried out on the same region of the sample. For these experiments, the sample surface is cleaned with acetone after the reduction reaction, and then the oxidation reaction is performed.

The samples are then imaged using Atomic Force Microscopy (Park Scientific Instruments Cp or Veeco Dimension 3100), which allows reaction locations to be ascertained. Images obtained using the Cp were taken in contact mode using gold-coated, sharpened pyramidal $Si_3N_4$ probes. For the Veeco Dimension, imaging was carried out in tapping mode, using antimony doped silicon probes with Pt/Ir coating. All images were taken at a resolution of 512 X 512.

Control experiments in a work by Giocondi [23] confirm that these reactions only occur when the light source contains photons with an energy exceeding the band gap, and that the reaction products do not formed homogenously in the solution during illumination and then attach to the surface in certain locations (i.e., the reaction occurs on

the surface where reaction products are observed). The elemental compositions of the deposits were also confirmed in a work by Giocondi et al.; deposits from silver reduction were observed to contain Ag and deposits from lead oxidation were observed to contain Pb [40].

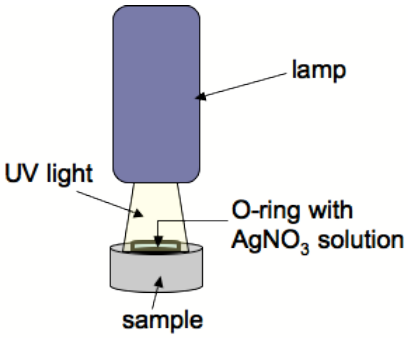


**Figure 3.9**. Experimental setup for reactions.

Fig. 3.10 presents a schematic that explains the experimental approach. The polarization vector of a domain is what determines whether or not a particular type of photochemical reaction (i.e. reduction or oxidation) will occur on its surface. The polarization vectors in the domains marked 1 and 3 are oriented so as to promote reduction on the $BaTiO_3$ surface. For the domain marked 2, the ferroelectric field does not influence carrier flow to the surface, so reaction is less likely. As reduction will occur preferentially on those domains whose polarization vector is favorably oriented (1 and 3), it is expected that a greater quantity of insoluble reaction products will be present on these domains. Reaction products will hence be observed to mimic the pattern of the domain structure. In this case, the silver will deposit in a striped pattern corresponding

to the striped pattern of the 90° domain boundaries. An AFM image of a striped pattern of reaction products on a $BaTiO_3$ substrate is presented in Fig. 3.11.

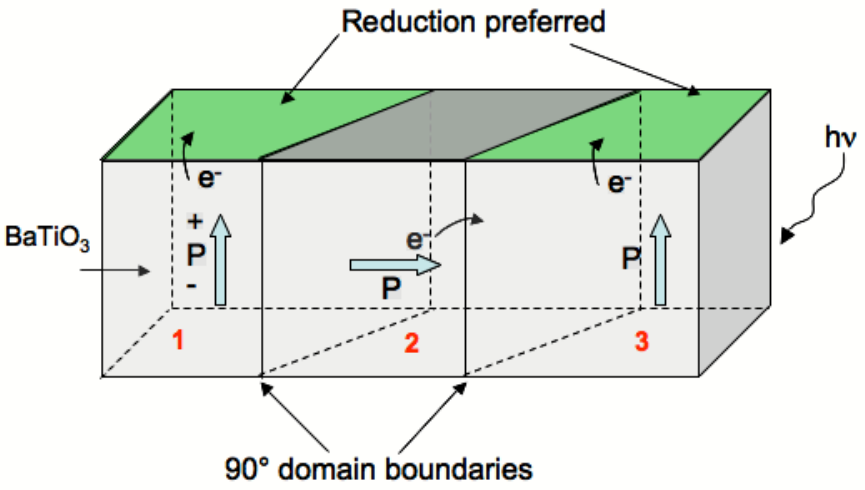


**Figure 3.10**. Schematic illustrating photochemical reaction behavior on ferroelectric $BaTiO_3$.

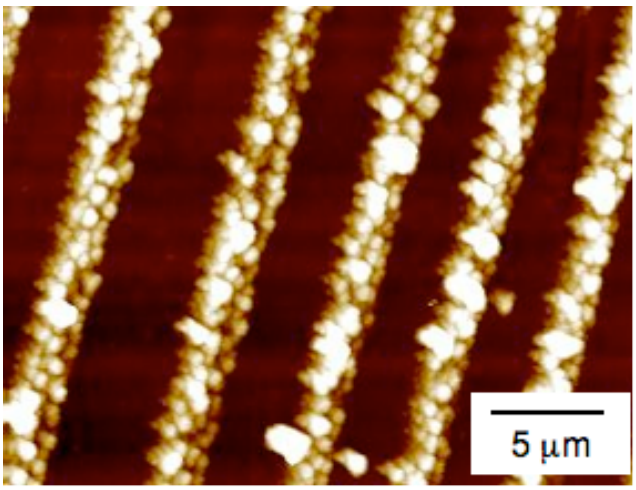


**Figure 3.11.** AFM image of a $BaTiO_3$ substrate surface after reaction in silver nitrate solution. Silver metal reaction product has deposited selectively on certain domains, producing a striped pattern on the surface.

### *3.4.1 Quantifying Spatially Selective Reactivity*

To compare the relative reactivities of two samples, it is necessary to quantify the extent of spatially selective reactivity. Determinations of which sample displays "more" spatially selective reactivity are made based on height profiles taken along ferroelectric domains. This is illustrated with the aid of Fig 3.12. Here, an image of domain selective reactivity on a $BaTiO_3$ substrate surface is shown in (a). In (b) a height profile for the red line marked in (a) is shown. Spatially selective reactivity is a measure of how well ferroelectric domains promote (or hinder) specific reactions. So, ideally there is a large amount of reaction product on one domain and a very small amount on the complementary domain. So, in the image we see a large amount of reduced Ag on "reactive" domains and very little reaction product on the complementary domains. For the work in this thesis, the greater the difference (in the amount of reaction product) between the "reactive" and complementary (or neutral) domains, the more effective a material is in spatially localizing reactions. The difference is quantified using the height profile. For example, in height profile shown in the figure, we can see that differences in height of reaction product for reactive and neutral domains average around 50 nm.

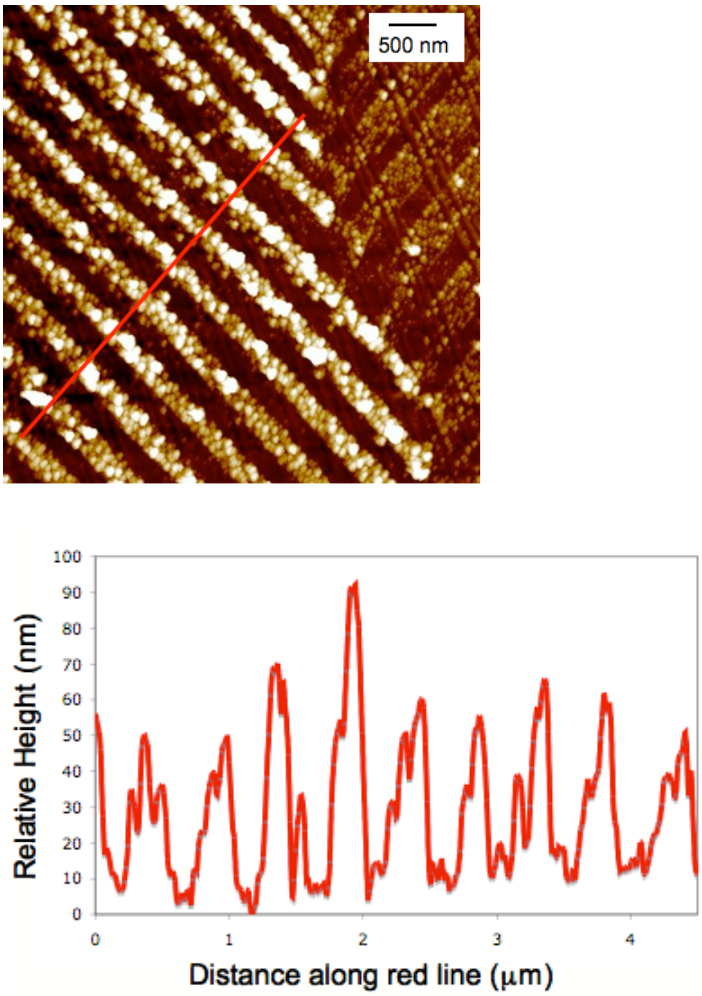


**Figure 3.12.** Illustration of how spatially selective reactivity is quantified.

## 3.5 Scanning Potential Microscopy

In addition to photochemical reactions, Scanning Potential Microscopy (SPM) can be used to establish a correlation between ferroelectric domain structure and reaction behavior. SPM is an AFM technique that can be used to obtain qualitative potential measurements of a sample surface. Since ferroelectric domains are associated with a surface charge, surface potential images have been used effectively to reveal the underlying domain structure of ferroelectric materials such as $BaTiO_3$.

In scanning potential microscopy, relative surface charge is detected by applying a bias to a tip that is oscillating at a certain resonant frequency. When the voltage of the tip differs from that of the sample surface, there is an electric force on the cantilever that causes a change in the resonant frequency, which can be detected by the microscope. If there is no voltage difference, the change in the resonant frequency is zero. So, for each point on the surface, the tip voltage is varied until the change in the resonant frequency is zero (i.e. until the tip and sample are at the same voltage). When this occurs, the tip voltage is recorded as data and a voltage map of the surface can be generated. It should be noted that before a bias is applied to the tip, a topographical scan of each line is performed. The tip then knows the surface topography and moves accordingly, so that the cantilever is only being affected by potential differences (and not by height variations).

An example of a surface potential image of $BaTiO_3$ is shown in Fig. 3.13. In (a), a topographical image of polycrystalline $BaTiO_3$ is shown. In addition to contrast arising from the polycrystalline $BaTiO_3$ microstructure (ex. grain boundary), there is some noticeable contrast from the ferroelectric domain structure. Fig. 3.13(b) shows a surface potential image of the same location. Here, contrast results primarily from differences in surface charge (note that the light to dark contrast is in mV not nm as in the topographical images). Both 90° (stripes) and 180° (curved lines) domain boundaries are observed. In this image, the relative charge of the domains can be used to indicate the direction of the domain polarization vector. Lighter areas correspond to a relatively positive measured surface charge compared to darker regions, so it would make sense to assume that the positive end of the domain polarization vector is pointed towards the surface in light

areas. This is, however, not the case. Analysis of surface potential images collected from ferroelectric materials has shown that the measured charge is actually related to screening charges that collect on the surface rather than to the charge of the domain dipole itself (in ferroelectric materials, charge screening can be provided by adsorbates, surface states or free charges).[95, 96] Consequently, the measured charge is actually the opposite of the charge created by ferroelectric polarization, i.e. light areas correspond to regions where the domain dipole has its negative end oriented towards the surface.

Since the surface potential image gives us information about the orientation of the domain polarization vector, it is possible that this information could then be used to predict which reaction (i.e. reduction or oxidation) will be preferred at a specific spatial location. If this is indeed the case, reaction behavior could be determined through AFM imaging. In this thesis, SPM imaging was conducted on a Vecco Dimension 3100 AFM in tapping mode. Probes were antimony doped silicon with Pt/Ir coating.

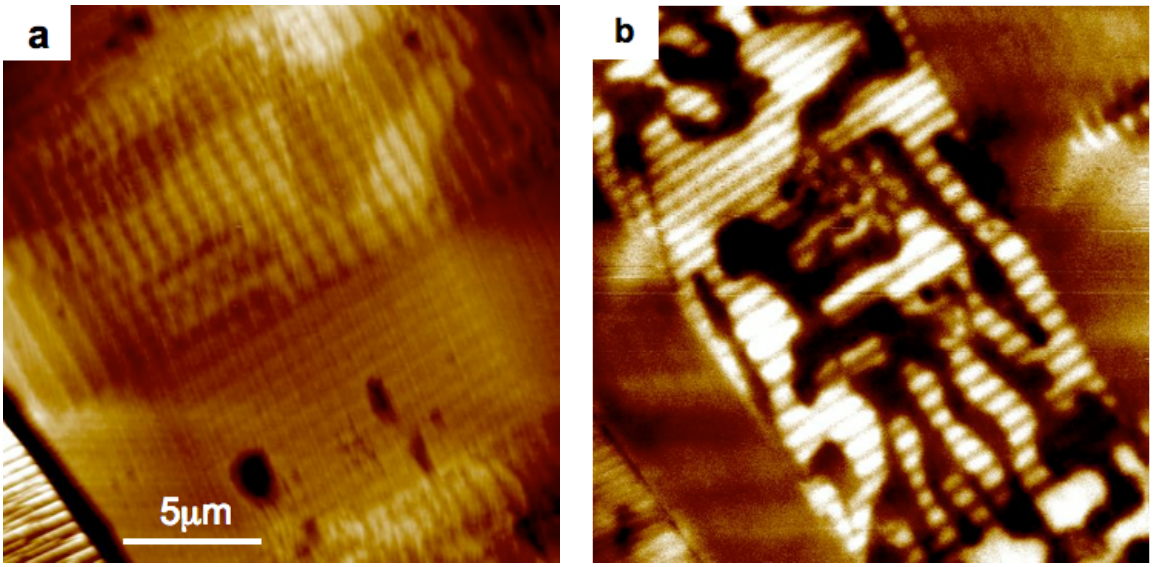


**Figure 3.13.** In (a), a topographical AFM image of the surface of $BaTiO_3$ is pictured. In (b), a surface potential image of the same exact location is shown. The domain structure can be observed in this image. Black-to-white contrasts are 60nm and 70mV, respectively.

# 4 Results: Characterization of $TiO_2$ films

## 4.1 Introduction

The purpose of this section is to present results that characterize the $TiO_2$ films that are grown on the $BaTiO_3$ substrate. Since the purpose of the films is to protect the $BaTiO_3$ surface, it is important that the interface between the two materials is continuous and smooth. This is discussed in section 4.2. Additionally, since both film and substrate orientation will influence photochemical reactivity, it is important to determine the relationship between them. For this experiment, the orientations of several grains on a $BaTiO_3$ substrate were first obtained. Then, a $TiO_2$ film (approximately 100 nm thick) was grown on the substrate. Previously indexed substrate grains were relocated and electron backscattered diffraction (EBSD) patterns were obtained to determine the corresponding film orientation and phase. Results for this are presented in section 4.3.

## 4.2 Film/substrate interface

To determine if the film/substrate interface is continuous, a FEI Nova 600 Focused Ion Beam (FIB) was used to cut out a cross section from a sample with a $TiO_2$ thin film. The cross section was taken from a {100} oriented substrate grain. The cross section was then imaged using a Transmission Electron Microscope (TEM). Shen Dillon performed cross section preparation and TEM imaging. Images of the film/substrate interface in cross section are presented in Fig. 4.1. From these images it is evident that the interface is continuous. Additionally, the TEM was used to collect diffraction

patterns for several spots along the length of the film. Patterns were consistent across the film, suggesting that film growth is epitaxial, at least for this orientation.

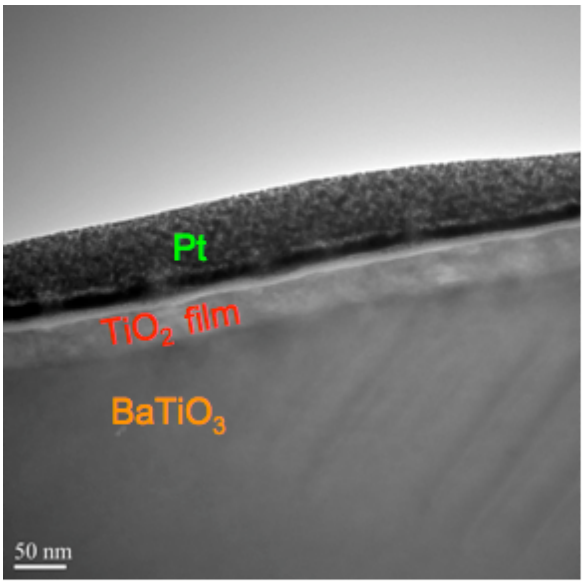


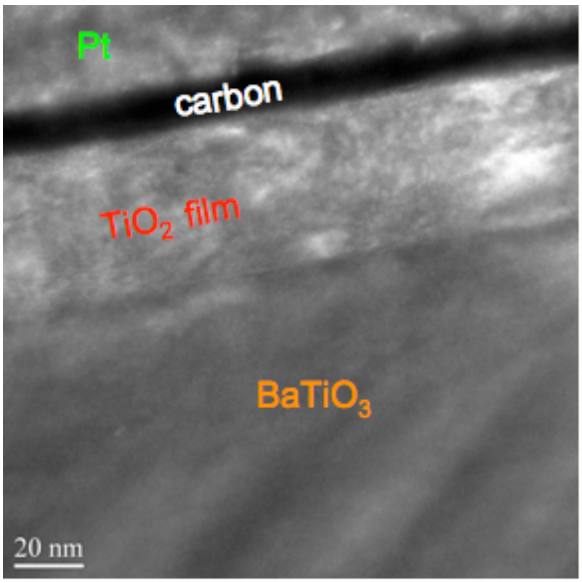


**Figure 4.1.** TEM images showing the cross section of the $BaTiO_3/TiO_2$ interface.

## 4.3 Film/substrate orientation relationship

Both film and substrate orientations were identified using EBSD patterns. A detailed description of the experimental procedure is provided in Section 3.3.2 of this document. The EBSD system returns a set of Euler angles that describe the transformation relating the crystal reference frame to the sample reference frame. These Euler angles can be expressed as a 3x3 matrix, *g*, that represents the transformation and will be referred to as the orientation [97]. In the sample reference frame, the vector representing the surface normal is **n'** = [001]. This vector in the crystal reference frame, **n**, is then given by:

$$c_i g \mathbf{n}' = \mathbf{n} \qquad (4.1)$$

Where $c_i$ are the symmetry operators of the crystal system. For the cubic substrate orientations, there are 24 proper symmetry operators and therefore, 24 equivalent vectors and we select the one with three positive components such that $n_3 > n_2 > n_1$, where $n_3$, $n_2$, and $n_1$, are the components of **n** along the c, b, and a crystal axes, respectively. For the tetragonal film, there are eight equivalent vectors and we select the one with three positive components and $n_2 > n_1$. The results are shown in Fig. 4.2.

In Fig. 4.2 (a), the orientations of several substrate grains are plotted. Each point indicates the orientation of one $BaTiO_3$ substrate grain. Here, the points are organized roughly according to color; for example, blue is used for orientations that are close to {111}, green is used for orientations close to {110}, and red is used for orientations close to {001}.

In Figure 4.2 (b), the corresponding orientations of the film are plotted. The data points for the film are organized into the same color groups as in Fig. 4.1(i.e. blue data points on the film plot correlate with blue points on the substrate plot). Anatase and rutile phases were both observed to form, depending on the orientation. Note that anatase and rutile film orientations are plotted together for simplicity. Data points to the right of the line marked on the graph represent rutile orientations, while those to the left are anatase orientations. From the plots we see that clear orientation relationships exist between {001} anatase and {100} $BaTiO_3$, between {010} rutile and {111} $BaTiO_3$ and between {110} rutile and {110} $BaTiO_3$.

The misorientation between the substrate and the film can also be calculated from the orientation data. The 3x3 matrix describing the misorientation ($\Delta g$) between the two crystals is:

$$\Delta g = c_i g_s (c_i g_f)^T \qquad (4.2)$$

where $c_i$ are the proper symmetry operators associated with the material with the lower symmetry ($TiO_2$) and $g_s$ and $g_f$ are the orientations of the film and substrate, respectively. Equation 2 produces $c_i^2 = 64$ equivalent representations of the misorientation. The misorientation can be represented as an axis angle pair, where the axis is a common direction in both crystals and the angle is a rotation about that axis which brings the two crystals into coincidence. In this case, we select the eight representations for which the three components of the misorientation axis are positive and $n_2 > n_1$.

This analysis was performed on all of the data in Fig. 4.1. Analysis of the nine pairs in the vicinity of (001) yielded 72 axis angle pairs meeting the condition described above. Of these, 45 (5 for each substrate/film pair) had a misorientation between 336 and 359 °. Eighteen more has misorientation angles between 171 ° and 189 °. The final nine were between 0 and 24 °. In other words, all of the rotation angles are approximately 0, $\pi/2$, or $\pi$. A plot of the distribution of misorientation axes is shown in Fig. 4.2. Note that the plot excludes the 9 points near zero misorientation; there is a singularity at this point in misorientation space and the axis orientation data is not reliable. The plot clearly shows that the misorientations can be described as rotations about the [001], [110], or [001] axes. In other words, the film is biaxially orientated with both the c and a axes aligned parallel to the same orientations in the substrate.

The above analysis was repeated for the other substrate-film pairs in Fig. 1 (those colored blue, green, and blue-green), but no consistent orientation relationship emerged. Based on this, it appears that the films with these orientations are oriented, but not biaxially.

## 4.4 Discussion

Schematic representations of the orientation relationships between polycrystalline $BaTiO_3$ and $TiO_2$ discussed above are provided in Fig. 4.4. These orientation relationships are in some agreement with previous observations of epitaxy between $TiO_2$ and perovskite single crystals. Previous studies on the orientation relationships between $TiO_2$ and perovskites were discussed in detail in Sec. 2.6.2. As mentioned in Sec. 2.6.2 the orientation relationship between the perovskite {100} orientation and {001} anatase

is well established [73-76]. Our results were consistent with this, as {001} anatase was observed to form on $BaTiO_3$ grains of the {100} orientation. For the {111} substrate orientation, the film was of the {100} rutile orientation, which is in close agreement with the works of Lotnyk et al. [77, 78], in which the {111} $BaTiO_3$ and $SrTiO_3$ orientation was observed to be the primary orientation formed on {100} rutile single crystals. And, for the {110} substrate orientation, rutile {110} was observed to form, which is somewhat consistent with the observations of Lotnyk et al. [77, 78]. In their studies, the {110} orientation was one of the orientations of $BaTiO_3$ and $SrTiO_3$ formed on {110} rutile.

As discussed in Sec. 2.6.2, $TiO_2$ is known to have an anisotropic reactivity [81-83]. Hence, it is possible that the orientation of the $TiO_2$ film could impact reactivity. The influence of $TiO_2$ film orientation on reactivity for the {100}, {110}, and {111} substrate orientations is examined in Chapter 10 of this document.

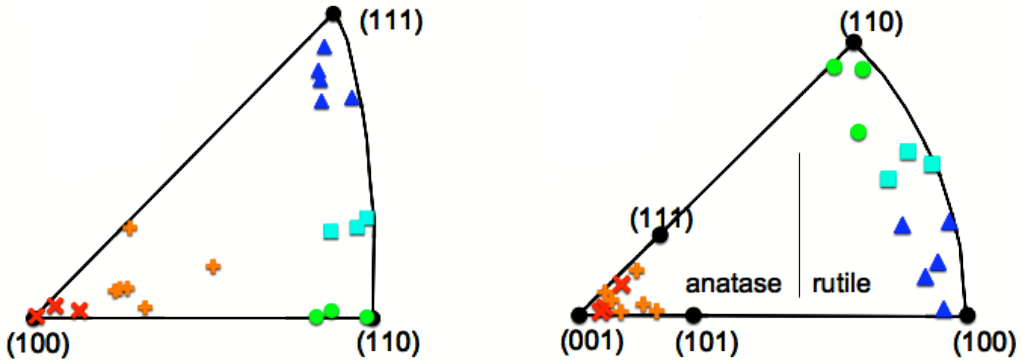


(a) BTO orientations (b) $TiO_2$ film orientations

**Figure 4.2.** (a) Orientation of the $BaTiO_3$ substrate grains. The corresponding $TiO_2$ film orientations are shown in (b) and the substrate-film pairs have the same coloring.

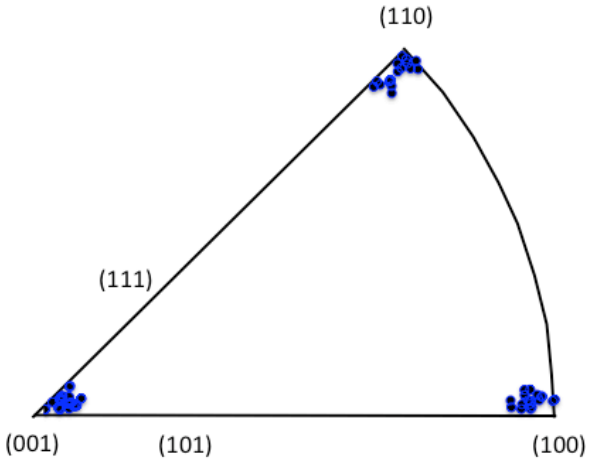


**Figure 4.3.** Distribution of the common crystallographic axes between the substrate and film for the nine pairs of observations near (001) in Fig. 1b (these are the red and orange points).

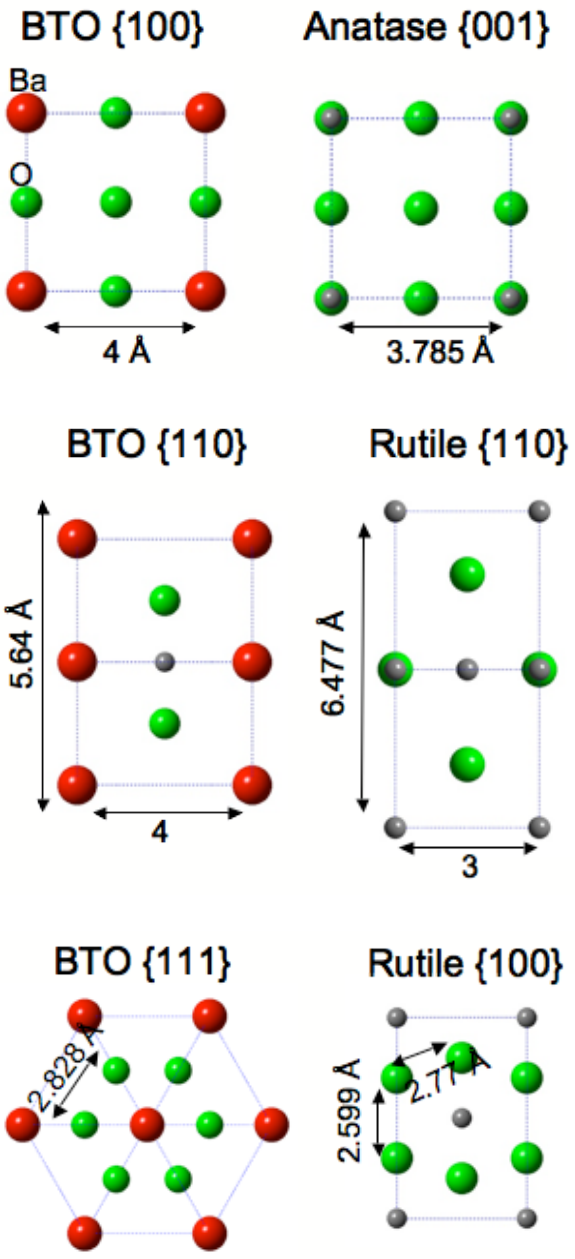


**Figure 4.4.** Schematics showing surface planes for the three orientation relationships established in this chapter.

# 5 Results: Effect of Ferroelectric Substrates on Film Reactivity

## 5.1 Introduction

For $BaTiO_3$, ferroelectric polarization causes reduction and oxidation reactions to occur in spatially distinct locations on the surface [13]. The primary aim of this study is to determine whether ferroelectric substrates ($BaTiO_3$ and $BiFeO_3$) can create a spatially localized distribution of oxidation and reduction products on $TiO_2$ film surfaces that correlate to the substrate domain structure. To investigate this, 15 nm films of $TiO_2$ were grown on $BaTiO_3$ and $BiFeO_3$ substrates. Photochemical oxidation and reduction reactions were then performed on the thin film surfaces and reaction locations were ascertained using AFM.

## 5.2 Results for Barium Titanate substrates

Figure 5.1 shows AFM images of a 15 nm thick film surface before and after reaction in silver nitrate and lead acetate solutions. In (a), some contrast results from features associated with the $BaTiO_3$ polycrystal microstructure; for example, a grain boundary is marked in the image. Additionally, within the grains, there is noticeable contrast resulting from the ferroelectric domain structure. The solid arrows in the figure indicate the direction of some of the apparent 90° domain "stripes". Recall that there are two possible sources of this domain contrast. Some contrast could result from topography created by differential polishing. Also, the sample is heated during film growth, so some contrast could be related to surface relief from domains created during cooling from the growth temperature. Hence, although some of the contrast could be

indicative of existing domain structure, some is purely historical and will not correlate with actual domains. The graph in Fig. 5.1 (b) shows the height profile of the blue line marked in the image.

In Fig. 5.1(c), height contrast results from the presence of silver deposits (white spots) from the reduction reaction. Much of the height contrast from Fig. 5.1(a) has disappeared, as the heights of the silver deposits are comparatively large, and thus dominate the image topography. This is evident in the graph in Fig. 5.1 (d), which compares the height profile from the blue line in (a) to the red line in (c). Silver is observed to deposit in a striped pattern that matches some of the domain structure seen in (a). Additionally, on the right side of the image (for example, within the red box), silver has deposited in patterns that resemble 180° domains. Thus, it is clear that ferroelectric domains are creating preferred sites for reduction on the thin film surface.

In Fig. 5.1(e), height contrast results from the presence of lead oxide (white contrast) that has been left behind on the surface after the oxidation reaction. Again, we observe that reaction products deposit in patterns consistent with the $BaTiO_3$ domain structure. Furthermore from these images we see that lead oxide and silver deposit in different, complementary locations. Areas in which this is easily observable are marked in the images. For example, within the blue box, silver is deposited on thin domains and lead oxide is deposited on the thicker domains in between. Within the red box, some 180° domains are visible. It is evident that the areas where the silver deposited in the reduction experiments are bare during the oxidation experiments, and vice versa. Several other regions were also examined and observations were consistent with the images presented in Fig. 5.1.

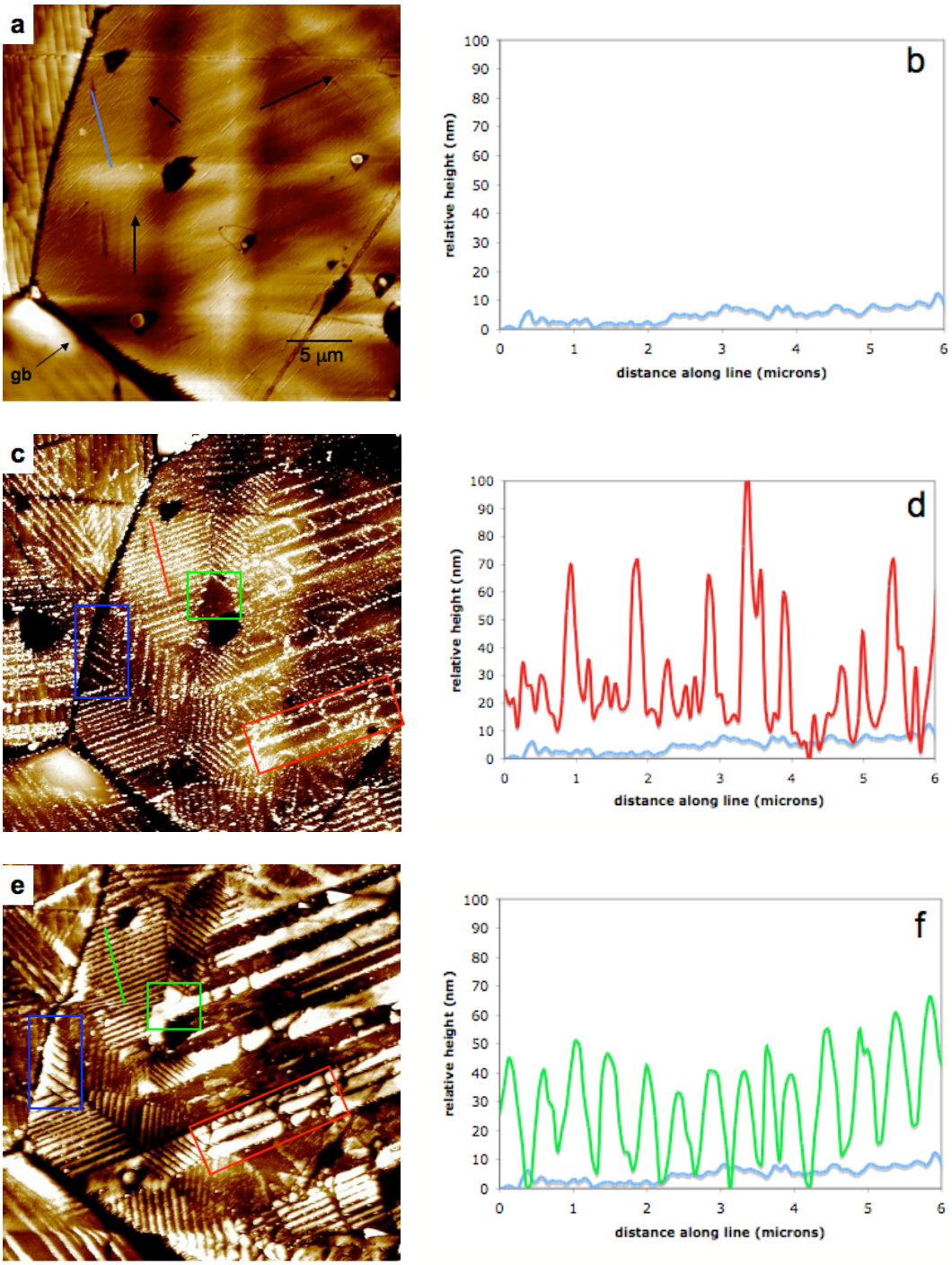


**Figure 5.1.** Topographical AFM images of a 15 nm thick $TiO_2$ film surface (a) before reaction (b) after reaction with silver nitrate solution and (c) after reaction in lead acetate solution. Solid arrows in (a) show the direction of some 90° domain "stripes. In (b) and (c) boxes show regions where it is evident that silver and lead oxide have deposited on opposite domains. Black-to-white contrasts are 70 nm, 55 nm and 80 nm, respectively.

## 5.3 Results for Bismuth ferrite substrates

Fig. 5.2 shows images of a 15 nm $TiO_2$ film surface supported by a $BiFeO_3$ substrate before and after being photochemically reacted in silver nitrate and lead acetate solutions. In (a), some contrast results from features associated with the $BiFeO_3$ polycrystal microstructure; for example, several pores are apparent in the images. Additionally, within the grains, there is noticeable contrast resulting from the ferroelectric domain structure. The green box delineates some of this domain contrast. In Fig. 5.2(b), silver deposits are observed to deposit preferentially in certain locations on the film surface. For example, within the green box, silver has deposited preferentially on top of the domain on the left. Spatially selectivity is also observed for the oxidation half reaction. In Fig. 5.2(c), lead oxide is observed to deposit preferentially in certain areas. Comparison of the two images reveals that the oxidation and reduction half reactions occur on complementary domains. For example, within the green box, the lead oxide has deposited on the domain on the right, which was the unreactive domain in the case of $Ag^+$ reduction. Hence, it is clear that for thin films supported by $BiFeO_3$ substrates, reduction and oxidation half reactions occur on top of different domains. This is consistent with results obtained for thin films on $BaTiO_3$ substrates.

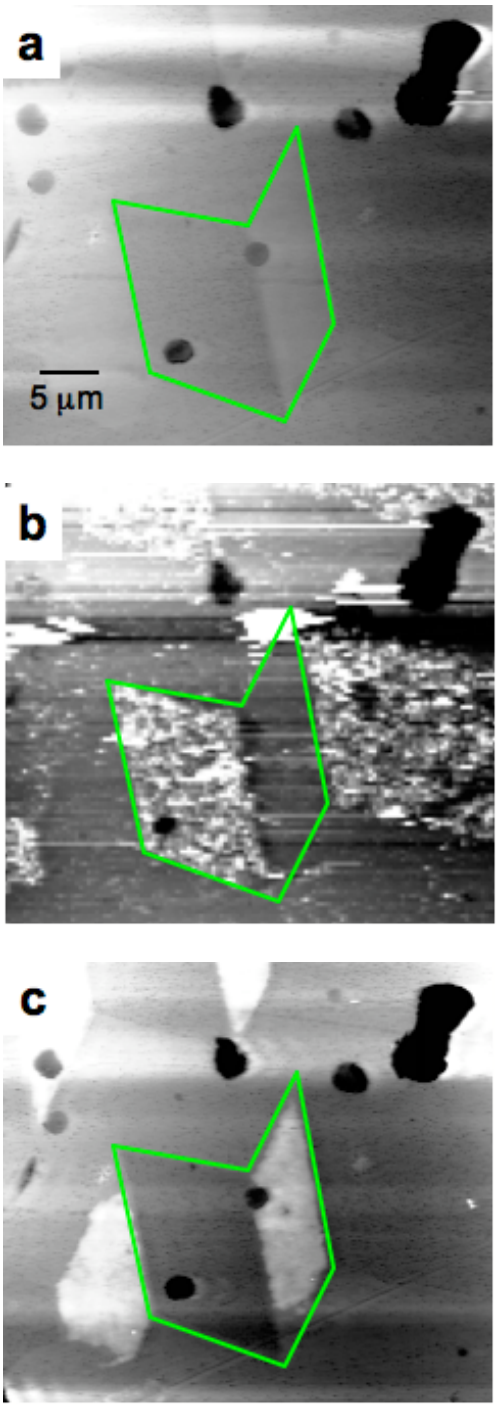


**Figure 5.2.** Topographical AFM images of a 15 nm thick $TiO_2$ film surface (a) before reaction (b) after reaction with silver nitrate solution and (c) after reaction in lead acetate solution. The green box marks the same location on each image. Within the box, reduction (b) occurs on domain on the left and oxidation (c) occurs on the domain on the right. Black-to-white contrast is 150 nm or all images.

## 5.4 Discussion

Photochemical reduction and oxidation reactions were observed to occur in spatially distinct, complementary regions on $TiO_2$ film surfaces supported by both $BaTiO_3$ and $BiFeO_3$ substrates. Patterns of reaction products on these film surfaces closely resemble reactions on bare ferroelectric surfaces and show little resemblance to reactions on $TiO_2$ surfaces (see Fig. 2.29 and Sec. 2.6.2 for a description of reactivity for $TiO_2$) [81-83]. Since the reactions on the thin films are so similar to those on bare $BaTiO_3$, it is reasonable to conclude that the ferroelectric polarization is the most influential factor in determining the reactivity on these 15 nm film surfaces. Possible effects from heterojunction formation (for both n/n and p/n junctions) or interaction between $TiO_2$ and the solution appear to be overwhelmed by the presence of the polarization.

Thus, results presented in this chapter show that ferroelectric substrates can, in fact, influence reactivity on thin films, which confirms the hypothesis proposed in Section 1.1 of this document. To better understand this effect, it is useful to correlate specific substrate domains to specific half reactions on the film surface. The next two chapters focus on establishing this correlation.

# 6 Results: Scanning Potential Microscopy and Reaction Location

## 6.1 Introduction

The purpose of this section is to evaluate the usefulness of Scanning Potential Microscopy (SPM) as a technique in correlating reaction behavior of thin films with underlying substrate domains. As mentioned in Sec. 3.5, SPM can be used to ascertain the domain structure of a material. In the first part of this chapter, the successful use of SPM in predicting half reaction locations on $BaTiO_3$ is demonstrated. Then, correlation of reactions on film surfaces to substrate domain structure is attempted. For this experiment, specific locations were first imaged using surface potential microscopy. These same locations were then reacted in the presence of silver nitrate solution (and lead acetate solution, for $BaTiO_3$ substrates) and imaged with topographical AFM.

## 6.2 $BaTiO_3$ Results

Fig. 6.1 and 6.2 show AFM and SPM images for a $BaTiO_3$ polycrystalline sample. Fig. 6.1(a) shows a topographical AFM image of the unreacted $BaTiO_3$ surface and Fig. 6.1(b) shows a surface potential image of the same location (the images were produced simultaneously). In Fig. 6.1(a), contrast arises from features associated with the barium titanate microstructure, such as a grain boundary (marked in the image) and surface facets, which are observed in the grain on the left-hand side. In (b), contrast results primarily from differences in surface charge (note that contrast is in mV). However, subtraction of the topography from (a) is not perfect, so some height related contrast is still apparent in this image. The pattern produced by the surface potential

measurements is characteristic of the $BaTiO_3$ domain structure and both 90° and 180° domain boundaries are observed. The plus and minus symbols in the image denote domains with polarization pointing towards and away from the surface, respectively. These pluses and minuses were assigned based on the interpretation of SPM images established by previous works [95, 96] as discussed in Sec. 3.5.

Silver reduction should be preferred in darker regions, where the positive end of the dipole is pointed towards the surface. In Fig. 6.1(c), it is clear that silver has preferentially deposited in a pattern that closely matches the domain structure seen in (b). Selective silver deposition is observed in locations corresponding to the darker regions of the surface potential image. Hence, surface potential images accurately predicted preferred sites for reduction.

After the silver reaction, the surface was cleaned with acetone and reacted in lead solution to confirm that the oxidation reaction would be preferred in locations corresponding to the lighter regions in the surface potential image. Fig. 6.2(a) and (b) show topography and surface potential images for the $BaTiO_3$ after cleaning. Fig. 6.2(a) shows that the surface is free of silver deposits from the previous reaction and Fig. 6.2(b) shows the domain structure after cleaning. Although domain motion is possible during handling and cleaning, the SPM image shows that the domains are unchanged. Fig. 6.2(c) shows a topographical image of the surface after reaction with lead acetate solution. The white contrast in this image results from deposits of $PbO_2$. It is obvious that the deposition of lead oxide occurs in areas that closely correspond to light regions on the surface potential image. It can thus be concluded that surface potential

measurements accurately predict preferred sites for oxidation and reduction for $BaTiO_3$ substrates.

## 6.3 Results from $TiO_2$ films

The next step is to determine whether surface potential microscopy can be used to predict preferential sites for reaction on a $TiO_2$ film surface. Fig. 6.3(a) and (b) show topographical and surface potential images of a 15 nm thick film surface. In (a), contrast again results from topography associated with features of the polycrystalline $BaTiO_3$ microstructure and the film. In (b), some surface potential contrast is observed. The surface potential image for the film is obscure compared to that of the substrate, but the pattern of surface charge does bear some resemblance to the 180° $BaTiO_3$ domain structure. In Fig. 6.3(c), a topographic image of the film surface after silver reaction is presented. Silver is observed to deposit on the film surface in a pattern consistent with the $BaTiO_3$ domain structure, however it is evident that there is no clear correlation between the surface potential measurements and the regions where reduction is favored. Similar results were obtained for the other film samples tested. These results indicate that while the ferroelectric field from $BaTiO_3$ is influencing reactivity on the thin film surface, the effect of the domain polarization is not apparent above the film surface where the probe senses potential. Thus, surface potential measurements are not useful in predicting reaction behavior for titania thin films on $BaTiO_3$ substrates.

## 6.4 Discussion

SPM is useful in predicting reaction behavior for $BaTiO_3$, but is not effective in correlating reactions on $TiO_2$ thin film surfaces with the domain structure of the underlying ferroelectric. SPM images of the film surfaces were obscure and did not clearly indicate the presence of ferroelectric domains. Since SPM measures the charge of surface adsorbates, these results indicate that the remnant polarization at the film surface is not significant enough to affect adsorbates at the film-vapor interface. Or, the effect isn't strong enough to be detected by SPM. However, reactions on the film surface are still clearly being influenced by the polarization. Thus, the polarization in the substrate must still be affecting charge carrier transport to the surface.

The relationship between substrate polarization and reactions on the film is still unclear. The next section presents results of another experiment designed to correlate polarization with reactivity on the film.

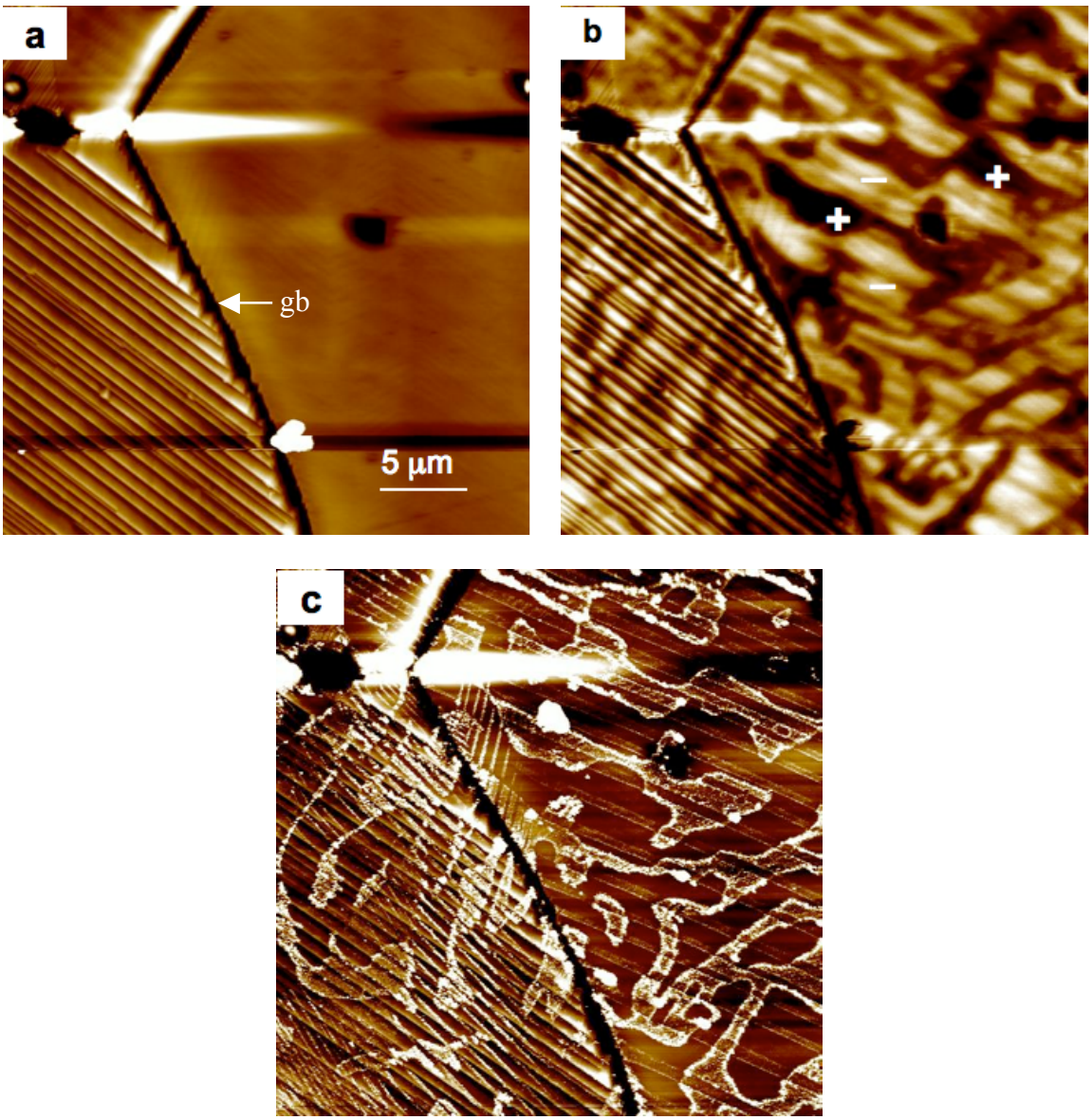


**Figure 6.1.** Topographical AFM images of $BaTiO_3$ surface (a) before reaction and (c) after reaction (silver nitrate, 3 seconds). In (b), a surface potential image of (a) is presented. Areas of preferential silver deposition correlate to the darker regions of the surface potential image. Black-to-white contrasts are 100nm, 175mV and 60nm, respectively.

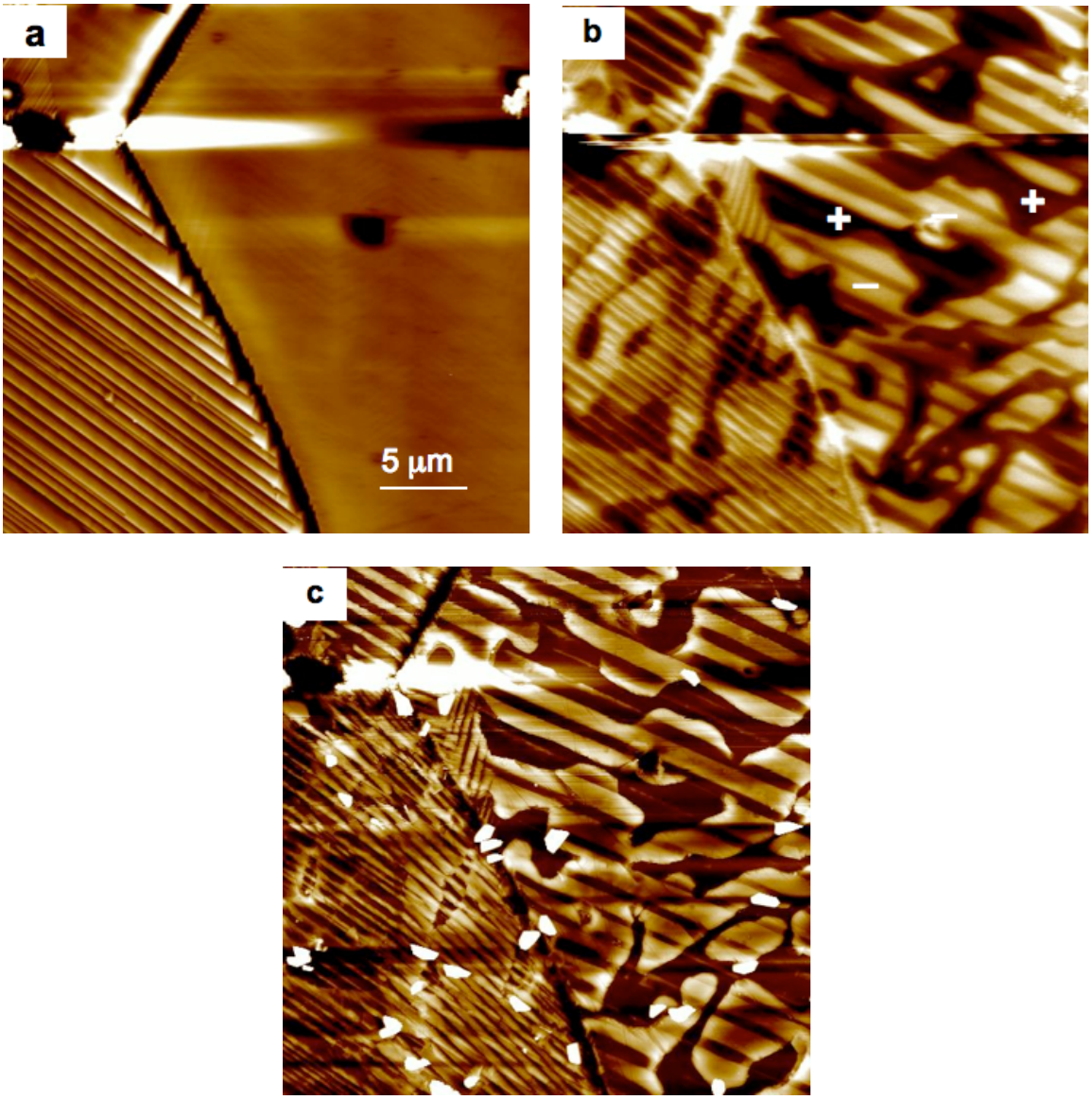


**Figure 6.2.** Topographical AFM images of $BaTiO_3$ surface (a) before reaction and (c) after reaction (lead acetate, 3 minutes). In (b), a surface potential image of (a) is presented. Areas of preferential lead oxide deposition correlate to the lighter regions of the surface potential image. Black-to-white contrasts are 100nm, 175mV and 60nm, respectively.

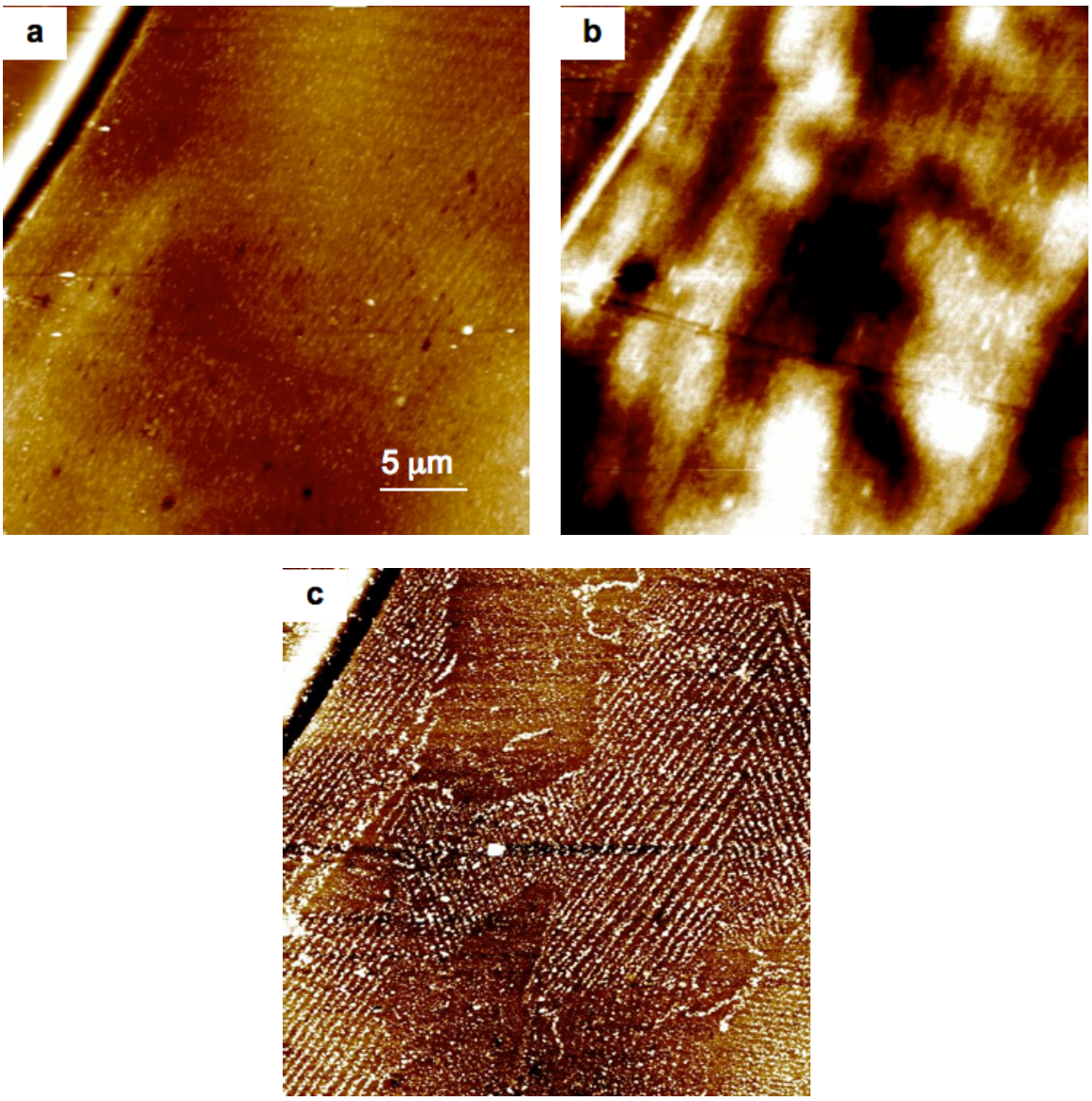


**Figure 6.3.** AFM images of 15 nm thick $TiO_2$ film surface (a) before reaction and (c) after reaction (silver nitrate, 15 seconds). In (b), a surface potential image of (a) is presented. No clear correlation is observed between reaction behavior and surface potential. Black-to-white contrasts are 80nm, 90mV and 70nm, respectively.

# 7 Results: Correlating Substrate Domain Polarization to Photochemical Reactions on the Film

## 7.1 Introduction

In Chapter 5, we demonstrated that oxidation and reduction half reactions occur on spatially distinct locations on a $TiO_2$ thin film grown on a ferroelectric substrate. Because the pattern of reaction products mimics the $BaTiO_3$ domain structure, it is assumed that the substrate domain polarization is responsible for the spatial separation of reactions on the film surface. However, it is unclear how domains from the substrate influence reactions on the film surface. The purpose of this section is to describe results of experiments that were designed to ascertain the relationship between the orientation of the substrate domain polarization and photochemical reactions on the film surface.

## 7.2 Results for $BaTiO_3$ substrates

The easiest way to relate substrate domain polarization to reactions on the film surface is to perform a reaction on a specific location on the surface of bare $BaTiO_3$, record (with AFM) which domains are preferred for oxidation and reduction reactions and then perform the same reaction on a $TiO_2$ film grown on top of the same exact location. However, for $BaTiO_3$, the experiment cannot be done in this manner. This is because domain structure can change during film growth (since films are deposited at a temperature exceeding the Curie temperature). Thus, domains in $BaTiO_3$ after film growth are not expected to be the same as they were before the film is deposited. As a result, the experiment was conducted in reverse order. First a 15 nm thin film of $TiO_2$ was grown on $BaTiO_3$. The film was then illuminated in the presence of lead acetate solution.

For a specific location on the film surface, reaction locations were recorded by AFM.

Next, the film was removed by polishing on a Logitech pm5 autopolisher for 30 seconds using 0.2 micron colloidal silica polishing solution. The polishing time was chosen based on an approximate rate of material removal that was experimentally determined (by Yiling Zhang) to be 20 nm/second (for $BaTiO_3$). Based on this, 30 seconds of polishing should remove 600 nm of material, which is approximately 40 times the amount of material that needs to be removed (15 nm). Thus, 30 seconds of polishing should be sufficient for the removal of a 15 nm film of $TiO_2$.

In Fig. 7.1(a), the reaction locations for the film surface are presented. Lead oxide (white contrast) has deposited preferentially in certain locations. Two domain stripes are marked with blue arrows. Fig. 7.1(b) shows an image of the same location after polishing with colloidal silica solution. In this image, the domain contrast matches the pattern of lead oxide from Fig. 7.1(a). As discussed in Section 2.2.1, it is likely that this domain contrast is present after polishing as a result of differential polishing effects (different domains polish at different rates). The same two domains are again marked with blue arrows.

In Fig. 7.1(c), an image of the substrate surface after reaction in lead acetate solution is shown. Here, we observe that lead oxide has deposited on the substrate surface in the same locations as on the film surface (again, blue arrows mark the positions of the same two domains). For these domains, the oxidation half reaction is preferred for both the bare substrate and the film. So, the domain polarization that promotes oxidation on the substrate also promotes oxidation on a thin film. Hence, the film is not altering which carrier is being preferentially driven to the surface.

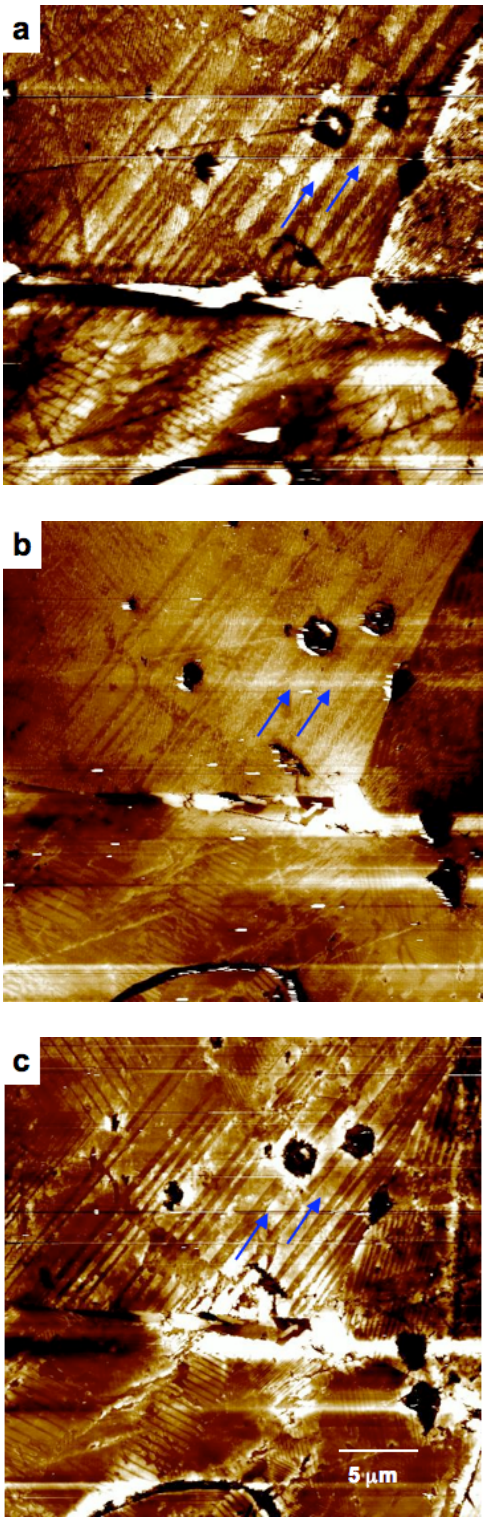


**Figure 7.1.** Topographical AFM images of (a) a 15 nm thick $TiO_2$ film surface after reaction in lead nitrate solution, (b) the same location after removing the film by polishing(c) the same location after polish and after reaction with lead acetate solution. Black-to-white contrast is 50 nm, 30 nm and 40 nm, respectively.

## 7.3 Results for $BiFeO_3$ substrates

For bismuth ferrite, the Curie temperature is high (~800°C), so the domain structure is preserved during film growth. Hence, the relationship between the substrate polarization and the preferred reaction on the film can be found by reacting the substrate, growing a film and then reacting the same location of the film. In Fig. 7.2(a), a visible light image of the bismuth ferrite surface taken using an optical microscope is shown. In this image, some domain contrast is apparent. A green box outlines a set of two domains. Fig. 7.2(b) is an image of the same location after reaction in lead acetate solution. Light contrast results from the presence of lead oxide deposits on the surface. It is evident that the lead oxide has only deposited on certain domains. Within the green box, the lead oxide is observed to deposit preferentially on the domain on the left. Silver reactions were also attempted but were unsuccessful and inconsistent.

After these two images were taken, a 15 nm film was grown on the substrate. In Fig. 7.2(c), an image of the film surface after reaction in silver nitrate solution is presented (note: different half reactions were performed on the film and substrate surfaces). Silver is observed to deposit preferentially on certain domains. Within the green box, silver has preferentially deposited on the domain on the right, which is the relatively unreactive domain in Fig. 7.2(b). At this point, it would make sense to conduct lead oxidation in this location, however, the sample cracked during cleaning after the silver reduction experiment, so the oxidation experiment was not performed.

By comparing the images presented in (b) and (c), it is evident that reduction on the **film** surface and oxidation on the **substrate** surface occur on opposite domains. In section 5.3, we showed that for a film grown on a $BiFeO_3$ substrate, reduction and oxidation reactions occurred on opposite domains. Thus, we can conclude that in Fig.

7.2(c), the oxidation-favoring domain (in the green box) would be the domain on the left. This is the same domain that promoted oxidation on the substrate surface. Thus, the same domain promotes oxidation or reduction on both the substrate and film surface, which confirms the results obtained from $BaTiO_3$.

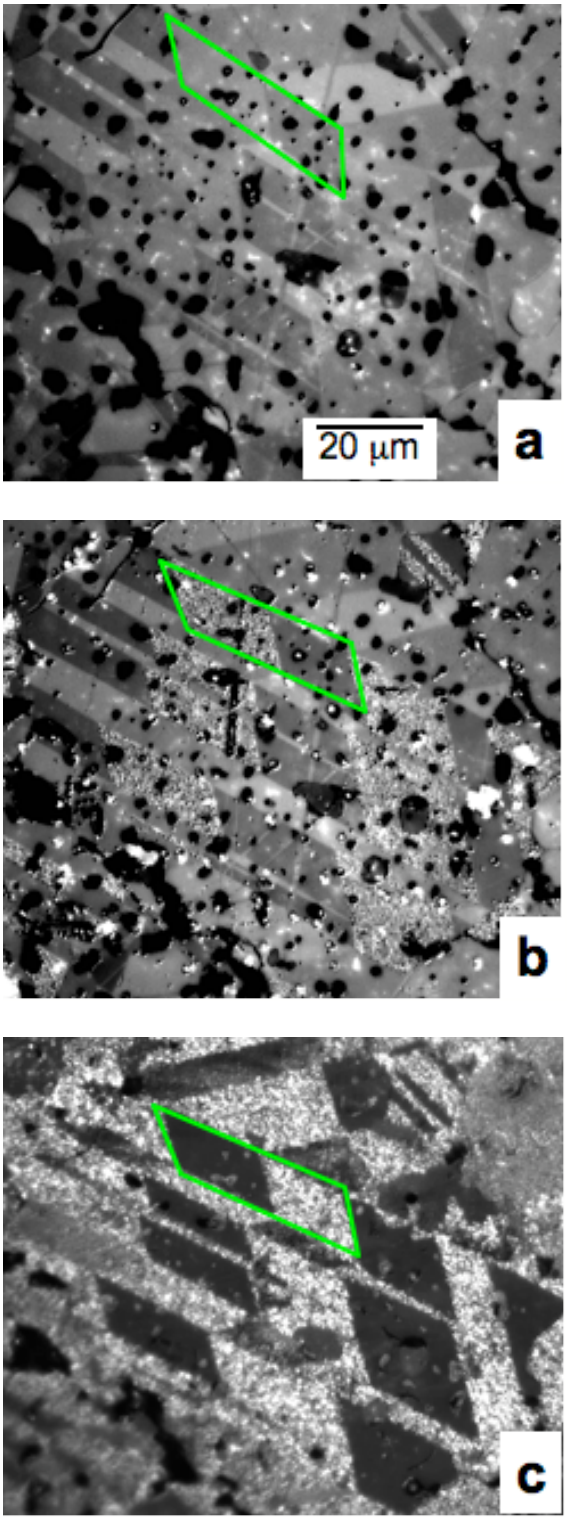


**Figure 7.2.** Optical microscope images of (a) $BiFeO_3$ substrate surface, (b) the same location after reaction in lead acetate solution. (c) is an image of the same location after film growth and after reaction in silver nitrate solution. The green box marks the same location in each image.

## 7.4 Discussion

In this chapter, it was demonstrated that domains that favor a certain half reaction on bare ferroelectric surfaces promote the same reaction on a thin film surface. This is illustrated schematically in Fig. 7.3. In this diagram, we see that the presence of the thin film does not affect which carrier is preferentially promoted to the surface and that polarization in the substrate plays a dominant role in determining which reaction is preferred on the thin film surface.

In a previous work [17], the enhancement in photocatalytic activity of a thin film supported by a ferroelectric was explained by the schematic shown in Fig. 2.24. According to the model in Fig. 2.24, the ferroelectric material induced band bending in the semiconducting film. Since the film was thin, the band bending extended to the surface of the film. As a result, when carriers were photogenerated in the film, only one type of carrier (electron or hole) was promoted to the surface and thus one type of half reaction was favored. As shown by Figure 2.24, the reaction favored on the film surface was the opposite of the reaction that would be favored on the bare substrate surface (for the same domain polarization). In the present experiment, this was not observed; the half reaction preferred on the film surface was the same that would be preferred on the bare substrate.

In order to explain our observations, we will first examine expected band diagrams for heterostructures immersed in solution. In Fig. 7.4, the band diagrams for a $BaTiO_3/TiO_2$ heterostructure are depicted (background information for construction of these diagrams was presented in Section 2.5). In (a), the polarization dipole is aligned with its negative end at the substrate-film interface; in (b), the dipole is aligned with the positive end at the substrate-film interface. Bands in the ferroelectric are shown to bend

at the interface in accordance with the polarization direction. Also at the interface, we see that bands in $TiO_2$ and $BaTiO_3$ are separated by conduction and valence band offsets (0.6 eV and 0.4 eV, repectively). The bulk Fermi energy is located 0.1- 0.2 eV below the conduction band edges [62]. Inside the film, space charge layers must form at both the substrate-film and solid-solution interfaces. For both (a) and (b), at the solid-solution interface, the surface voltage, $V_S$, must be screened by the semiconductor. For a n-type material, $V_S$ is a few tenths of an eV above the equilibrium conduction band position [47] and hence bands at this interface bend up. At the ferroelectric-$TiO_2$ interface, a space charge layer results from heterojunction formation as well as from the presence of a polarization. For the negative polarization, bands bend up at the interface, while for a positive polarization, bands bend down at the interface. Since the film is sufficiently thick, charge screening at both interfaces is achieved and bands in the bulk of the material are at their equilibrium positions.

Figure 7.5 presents an analogous situation for the case of a thinner $TiO_2$ films (like the ones in this experiment). Here, the presence of charge at both interfaces requires screening. The position of the conduction band edge at the solid-solution interface is set by $V_S$. At the ferroelectric-semiconductor interface, the conduction band position is set by the bottom of the conduction band offset between the two materials. From these set positions, the bands attempt to approach their bulk, equilibrium positions (indicated in the figures by a dashed line marked $E_C$ equil. $TiO_2$). However, the film is not thick enough to accommodate the full extent of band bending, so bands never return to their equilibrium positions [70] (for a more detailed discussion of expected band bending in thin films, see Section 2.5.5). The schematic in Fig. 7.5 shows a plausible example of

band bending in the thin film. As shown, the conduction band edge extends continuously between the boundary conditions set by the two interfaces.

As mentioned above, it is likely that band bending in the film is not responsible for the observation of spatially selective reactivity (since the preferred carrier at the surface is not reversed). Thus, the schematic in Fig. 7.6 illustrates another plausible explanation for the observations presented in this chapter. The yellow shading in the figure represents the depth of light penetration into the material. For a 15 nm film, only around 10% of the incident light intensity is absorbed in the film. Hence, almost 90% of the incident light reaches the substrate and we can assume that the majority of electrons and holes are photogenerated in the substrate (see Section 2.4 for a discussion of light absorption in $TiO_2$).

Since the majority of electrons and holes are photogenerated the substrate, it is plausible that electrons and holes generated in the substrate are responsible for observed spatially selective reactivity on the thin film surface. As illustrated in the figure, the polarization causes an excess of one carrier type to move to the interface. So, for example, in Fig. 7.6 (a), an excess of holes are promoted to the interface while electrons are driven away towards the bulk. Since a majority of electrons are being driven away from the $TiO_2$ surface, it is possible that, for a negative charge at the interface, the majority of carriers available for reaction are photogenerated holes (since only a small fraction of carriers are photogenerated in the film). In this case, oxidation would still be the preferred reaction for this domain.

It should be noted that the fact that the majority of carriers are generated in the substrate does not necessarily imply that these carriers make it to the surface to react; it is

possible that they recombine before reaching the surface or that they are scattered at the interface. Additionally, for both cases the band diagrams show that there are potential wells at the ferroelectric-substrate interface, which could act as traps for electrons and holes moving towards the surface from the substrate. However, based on the experimental results, it is clear that a preferred carrier is being driven towards the surface. Since it is unlikely that band bending in the film is responsible for this, it is reasonable to assume that an excess of one type of carrier is available at the surface because of band bending in the substrate. It is hence concluded that enough of the carriers photogenerated in the substrate make it to the film surface to produce the spatial localization of reactions.

For the case depicted in Figure 7.6 (b), bands are shown to bend up, which is a barrier to the flow of electrons toward the surface. This upward band bending is also present at the surface of bulk $TiO_2$ and previous research [82, 85] has shown that significant reduction of silver does occur on the surface of $TiO_2$. Although the upward band bending favors the transport of holes to the surface (oxidation is the "easy" reaction), some electrons do also make it to the surface. These electrons can nucleate clusters of silver and once formed these metallic clusters create downward band bending in the semiconductor (see Fig. 7.7) and effectively draw more electrons into the particle and to the surface to react [46, 47, 98]. For this domain polarization, an excess of electrons are available to move into the metal clusters, so the reduction reaction is effectively promoted. For catalysts used in water splitting, metallic reaction products are not formed from the reduction reaction. In this case, metallic co-catalysts (such as Pt) could be deposited on the surface above negatively polarized domains, so that the reduction reaction can occur preferentially [46].

It is also possible that electrons move through the barrier by tunneling. In a study by Dunn et al. [15], the reduction of silver ions was performed on ferroelectric PZT surfaces. For lower energy radiation, reduction was observed to occur preferentially on domains in which the positive end of the dipole intersected the surface. When the energy of the radiation was increased, significant amounts of silver also began to form on domains in which the negative end of the dipole was pointed towards the surface (recall that at negative surfaces, domains are generally bent up and electron flow to the surface is hindered). This observation was attributed to an altering of the band structure during illumination. Illumination creates an excess of electrons and holes that can occupy states in space charge regions and can thus change the space charge layer width [15, 35]. In this case, the authors stated that the higher energy radiation created many more photogenerated carriers then the lower energy radiation, As a result, more carriers were available to compensate for charge in the space charge layer, and, consequently, the width of the space charge layer was decreased. This decreased the width of the barrier (to electron flow) enough that electrons were able to tunnel through and reduce silver ions. It is possible that a similar effect is occurring in the thin films in the present study. If the barrier to electron flow is thin enough, electrons may just be able to tunnel through the barrier and reduce silver ions at the surface.

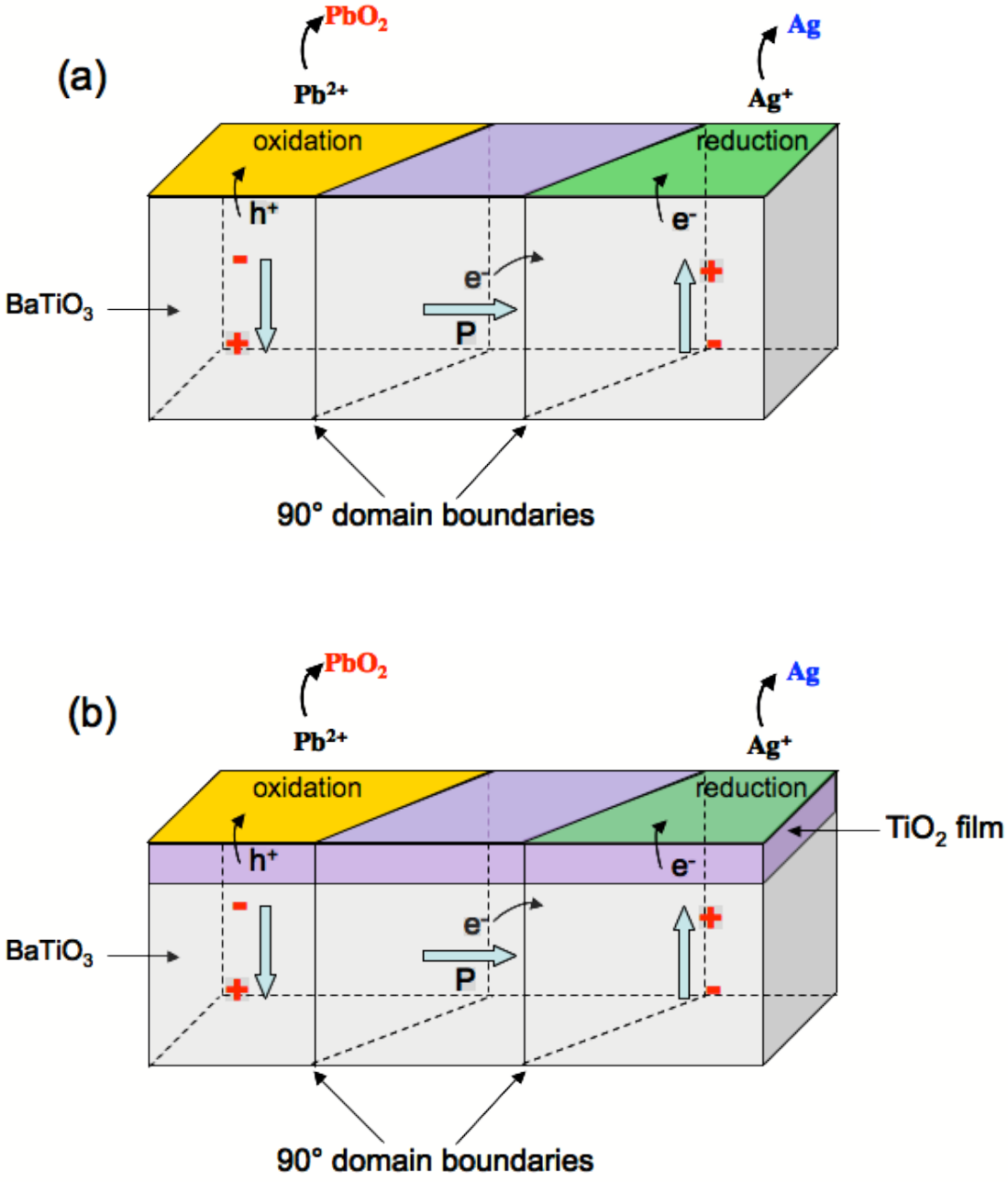


**Figure 7.3.** Schematic demonstrating that domains in substrate promote the same half reactions on both the bare substrate (a) and film (b) surfaces.

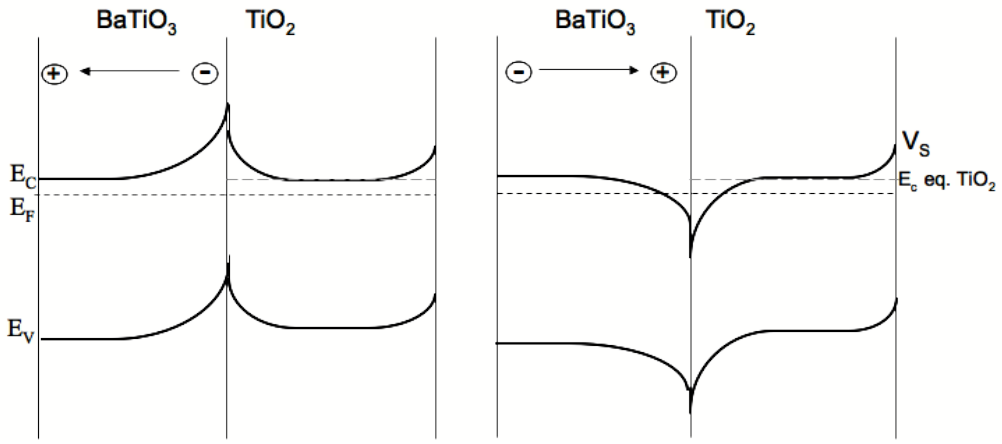


(a) (b)

**Figure 7.4.** Schematic showing proposed band diagram for a $BaTiO_3/TiO_2$ (thick film) heterostructure. Note that band bending in the film proceeds to the full extent and bands in the bulk of the film are at their equilibrium positions. $E_C - E_F \sim 0.1\text{-}0.2$ eV, and $V_S$ is several tenths of an eV above $E_C$ [47, 62]. Conduction and valence band offsets are 0.6 eV and 0.4 eV, respectively.

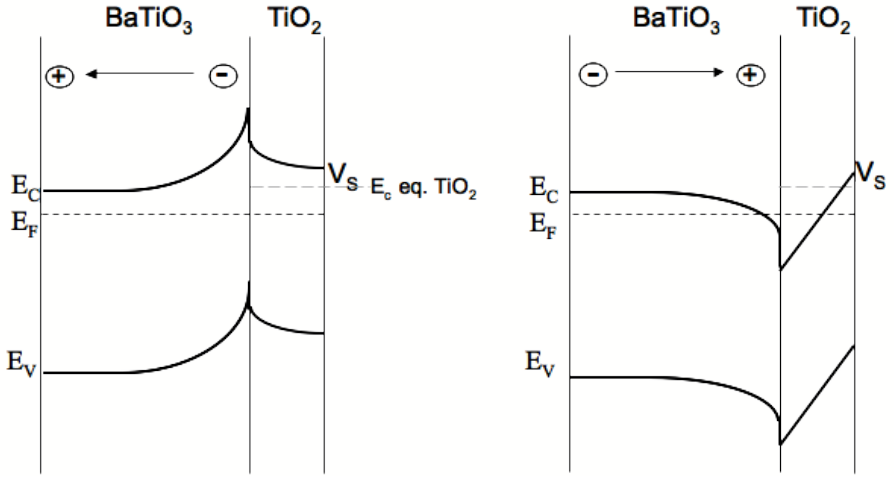


(a) (b)

**Figure 7.5.** Schematic showing proposed band diagram for a $BaTiO_3/TiO_2$ (thin film) heterostructure. Note that band bending in the film does not proceed to the full extent and bands in the film do not reach their equilibrium positions.

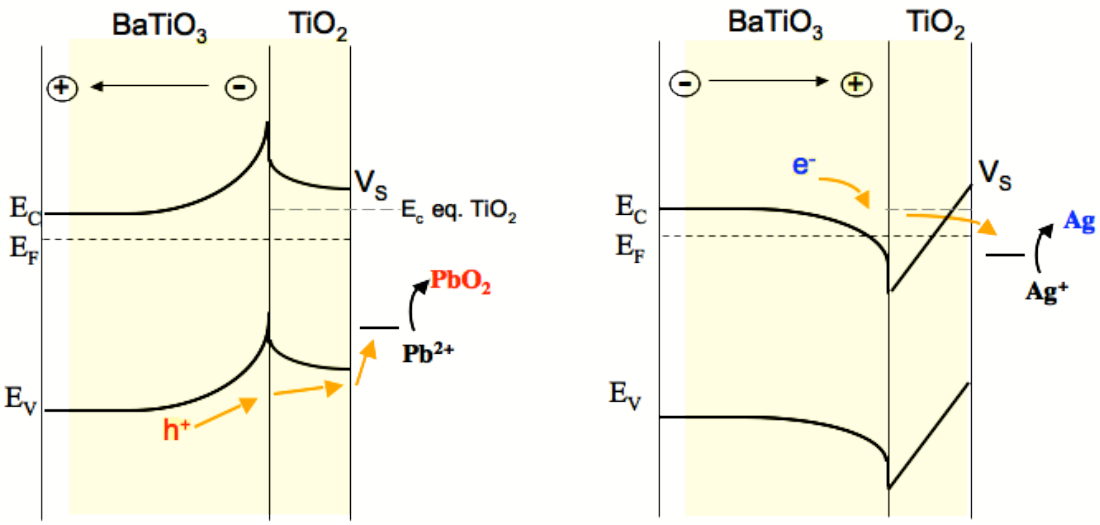


**(a)** **(b)**

**Figure 7.6.** Schematic showing proposed behavior of charge carriers in heterostructures.

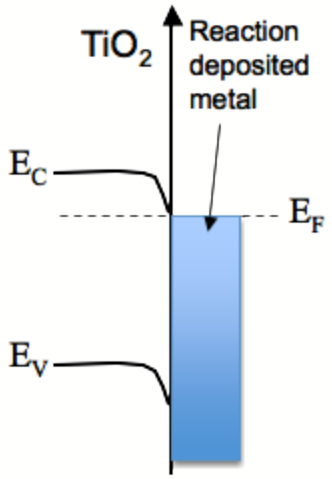


**Figure 7.7.** Schematic showing downward band bending at the interface between the semiconductor and metal clusters.

# 8 Results: Effect of Film Thickness on Reactivity

## 8.1 Introduction

The results presented in Chapter 5 illustrate that $BaTiO_3$ and $BiFeO_3$ substrates do affect photochemical reaction behavior on thin films, creating spatially localized oxidation and reduction sites on the film surface. The purpose of this section is to see if the thickness of the titania film on the ferroelectric substrate affects the spatial selectivity of reactions on the film surface. In Chapter 7, it was proposed that carriers that are photogenerated in the substrate are responsible for the observed spatially selective reactivity on the film surface. As film thickness is increased, a smaller percentage of carriers will come from the substrate, thus it is expected that the effect of the substrate on reactivity on the film surface will diminish as the thickness of the film is increased.

## 8.2 Results for grains of unknown orientation

Because reactivity can be anisotropic [83], it is important to note that the orientation of grains observed in this experiment are unknown. Inspection of grains on samples with 10 nm, 50 nm, and 100 nm thick films suggested that spatially selective reactivity diminishes with film thickness. In Figs. 8.1-8.3, images of several locations for thin (10 nm), medium (50 nm) and thick (100 nm) film samples after reaction in silver nitrate solution are presented. For the thinnest film, spatially selective reactivity was easily identified; in fact, it was clearly observed for all of the grains examined. For a 50 nm film, however, spatially selective reactivity was apparent for some of the grains, but absent on others. For the thickest films (Fig. 8.3), spatially selective reactivity was

encountered very infrequently and was much less marked when observed. For images of the thickest film, where spatially selective reactivity is no longer observed, it is important to note the difference in reactivity between the grains in the image. For example, in the bottom image of Fig. 8.3, it is clear that the top grain is much more reactive than the bottom one. This suggests that when the ferroelectric field is screened to the point that it no longer affects surface reactivity, the behavior is controlled by the orientation dependent photochemical reactivity of $TiO_2$ (the anisotropic reactivity of $TiO_2$ is discussed in more detail in Sec. 2.6.2) [83].

Height differences taken of random grains also confirmed that spatially selective reactivity decreases with increasing film thickness. Average height differences between reactive and neutral areas were 127 nm, 80 nm, and 57 nm for film thicknesses of 10 nm, 50 nm, and 100 nm, respectively.

## 8.3 Results from grains of known orientation

Results from randomly oriented grains strongly suggest a decline in spatial selectivity as film thickness is increased. To more effectively isolate the effect of film thickness, the experiment was carried out on grains of known orientation. Orientations were determined using EBSD as described in Sec. 3.3.2. Figs. 8.4-8.7 show results for film thicknesses of 10nm, 30nm, and 50nm, and 110nm respectively. For each figure, (a) shows an image of the film surface before reaction and (b) shows the same location after reaction in silver nitrate solution. The central grain in each set of images is of the {100} substrate orientation, which is covered by anatase {001}.

In Fig. 8.4(a), some of the height contrast appears to be associated with both 90° and 180° ferroelectric domains. For example, the solid arrows indicate the direction of some of the 90° domain "stripes". In Fig. 8.4(b), it is clear that silver has deposited in a striped pattern matching the $BaTiO_3$ domain structure. Between the stripes, there appears to be considerably less reaction product, which indicates that the ferroelectric field is effectively confining the reaction to specific spatial locations. Further evidence for this is shown in Fig. 8.8(a) and (b). Here, height data for a specific line of the reacted image is plotted. Fig. 8.8(b) shows a height profile for the line marked in (a). The line has been drawn over a set of "stripes" in order to highlight the difference in reactivity between preferred and neutral areas. The profile shows a considerable difference in reactivity; heights for silver "stripes" are between 50 and 150 nm more than heights for the neutral areas in between.

In Fig. 8.5, before and after images for a 30 nm thick film are shown. As in the case of the 10 nm film, silver is observed to deposit in a striped pattern characteristic of 90° domains. However, a height profile (Fig. 8.8(d)) taken across the silver stripes suggests that the spatial preference is slightly less pronounced. Height differences between reactive and neutral areas are smaller compared to those for the thinnest film.

For a film thickness of 50 nm (Fig. 8.6), preferred locations for reduction reactions are still apparent, as silver deposits in a pattern resembling the 180° domain structure of $BaTiO_3$. However, it is clear that the influence of the ferroelectric field is diminishing. As shown by the height profile in Fig. 8.8(f), height differences between reactive and unreactive areas are closer to 50 nm, with only a couple areas having heights near 100 nm. These height differences are significantly smaller than for the 10 nm film.

For the thickest film (Fig. 8.7), spatially selective reactivity is no longer apparent as the reaction in (b) is observed to be uniform. For this case where spatially selective reactivity is no longer observed, we again observe that reaction behavior is controlled by the anisotropic photochemical reactivity of $TiO_2$.

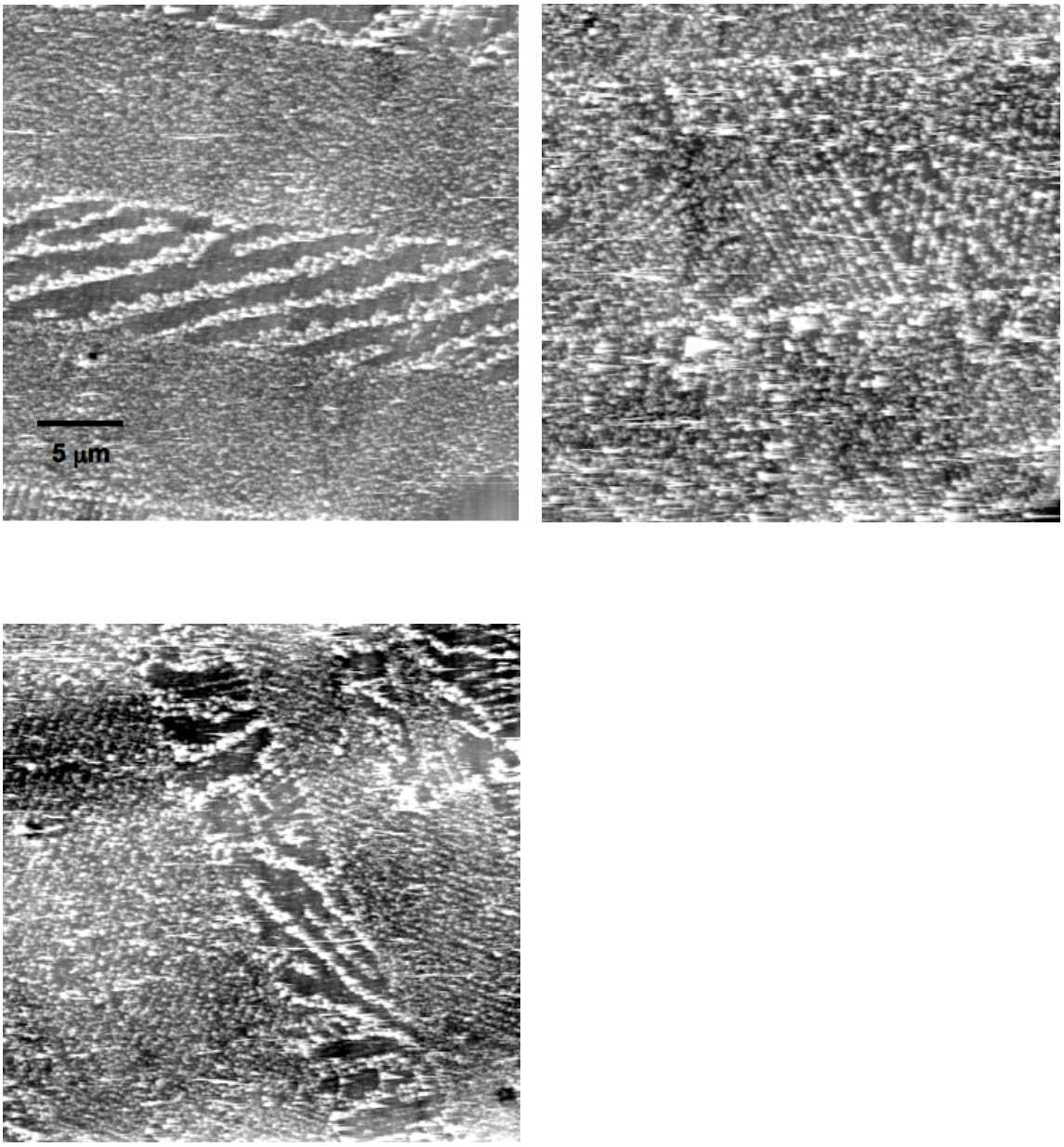


**Figure 8.1.** Topographical AFM images of 10 nm thick $TiO_2$ film surfaces after reaction. Silver is clearly observed to deposit preferentially in a pattern corresponding to the $BaTiO_3$ domain structure in all three images. Black-to-white contrasts are 210 nm (top left), 250 nm (top right) and 160nm (bottom).

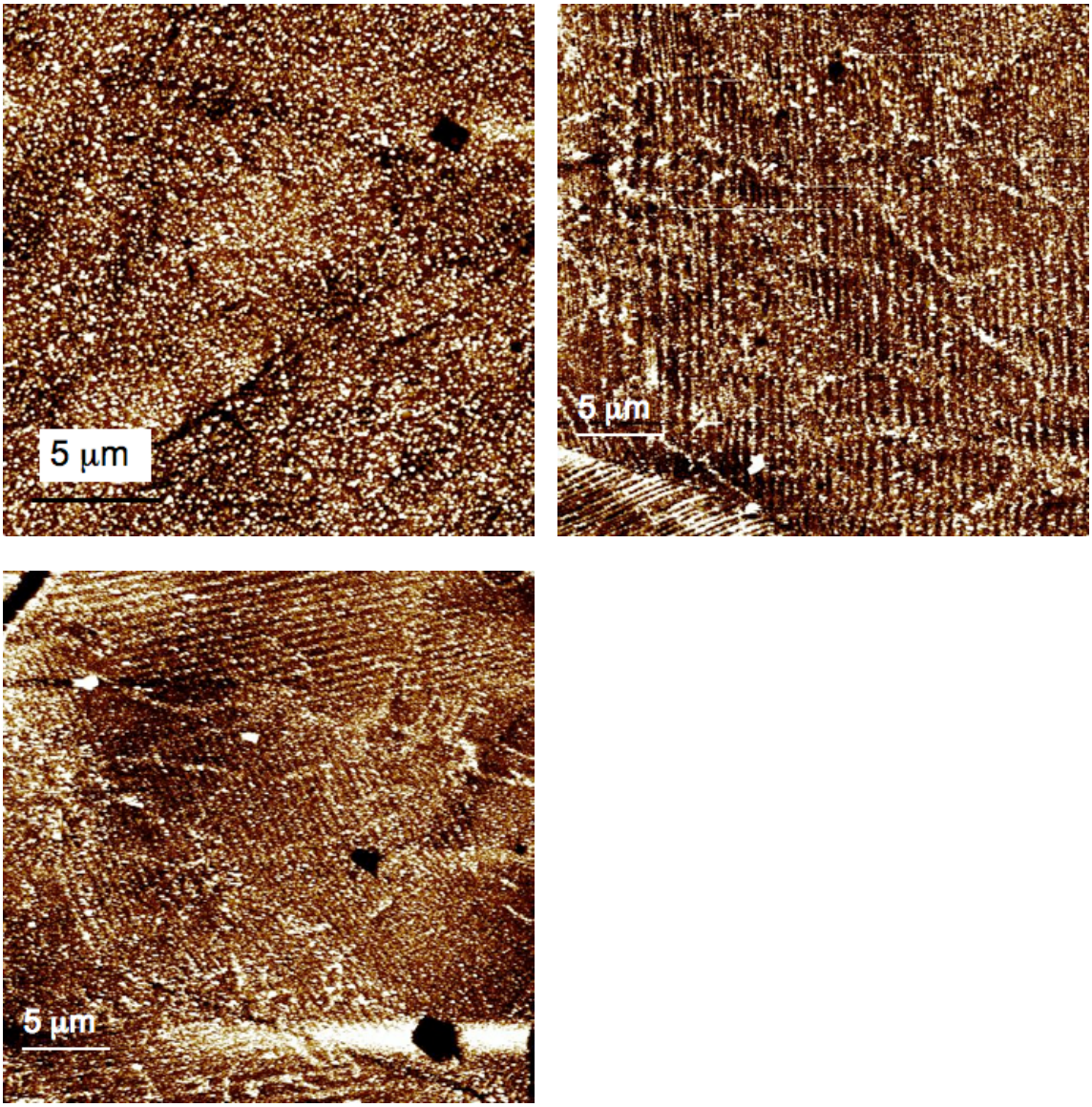


**Figure 8.2.** Topographical AFM images of 50 nm thick $TiO_2$ film surfaces after reaction. Silver is observed to deposit preferentially in the bottom and top right images. Deposition is uniform for the grain in the top left. Black-to-white contrasts are 80 nm (top left), 70 nm (top right) and 70 nm (bottom).

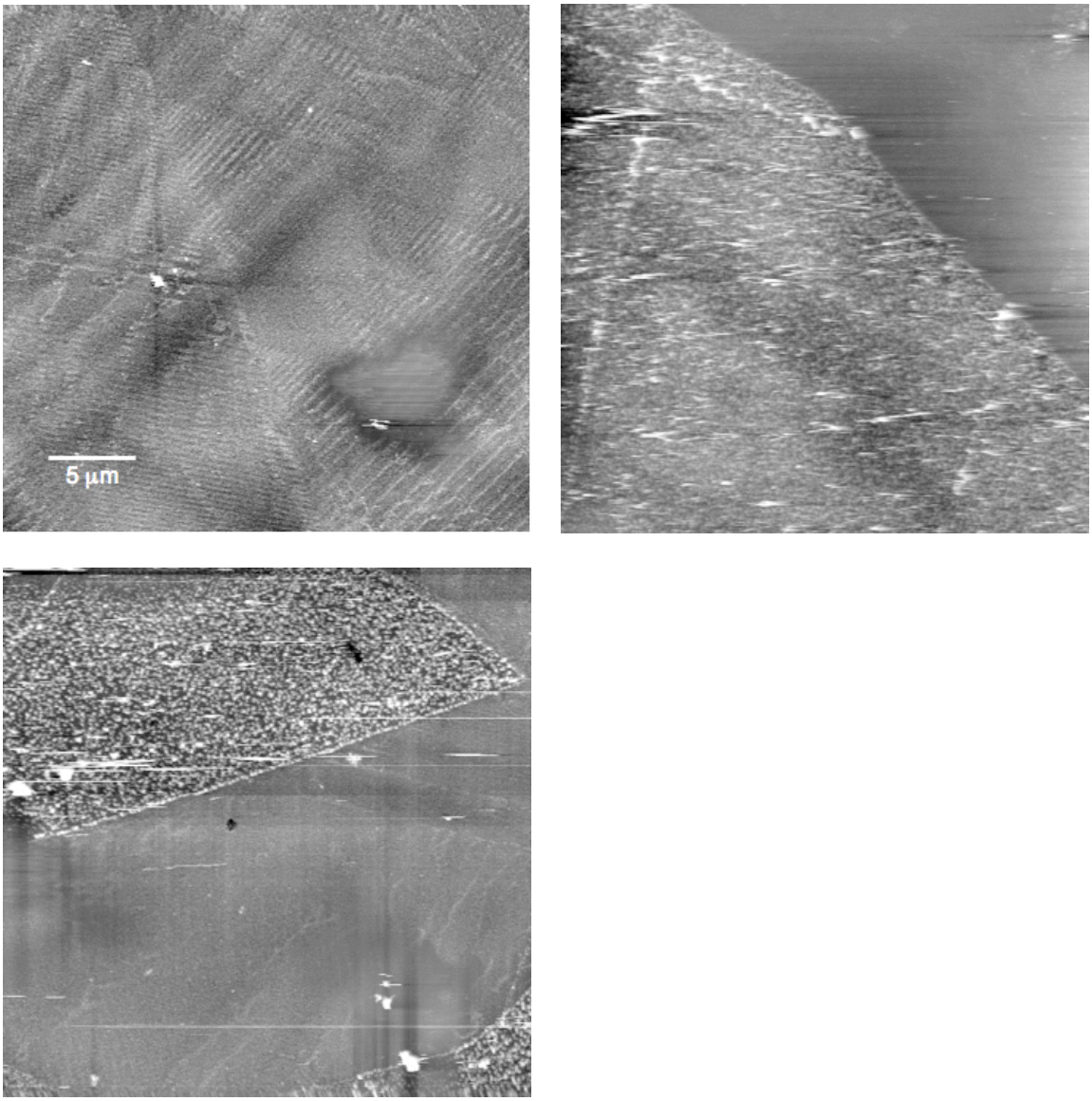


**Figure 8.3.** Topographical AFM images of 100 nm thick $TiO_2$ film surfaces after reaction. Slight spatial localization is observed in the top left image. For the other two images, reactivity seems to be based on $TiO_2$ orientation, as some grains appear considerably more reactive than others. Black-to-white contrasts are 130 nm (top left), 200 nm (top right) and 200 nm (bottom).

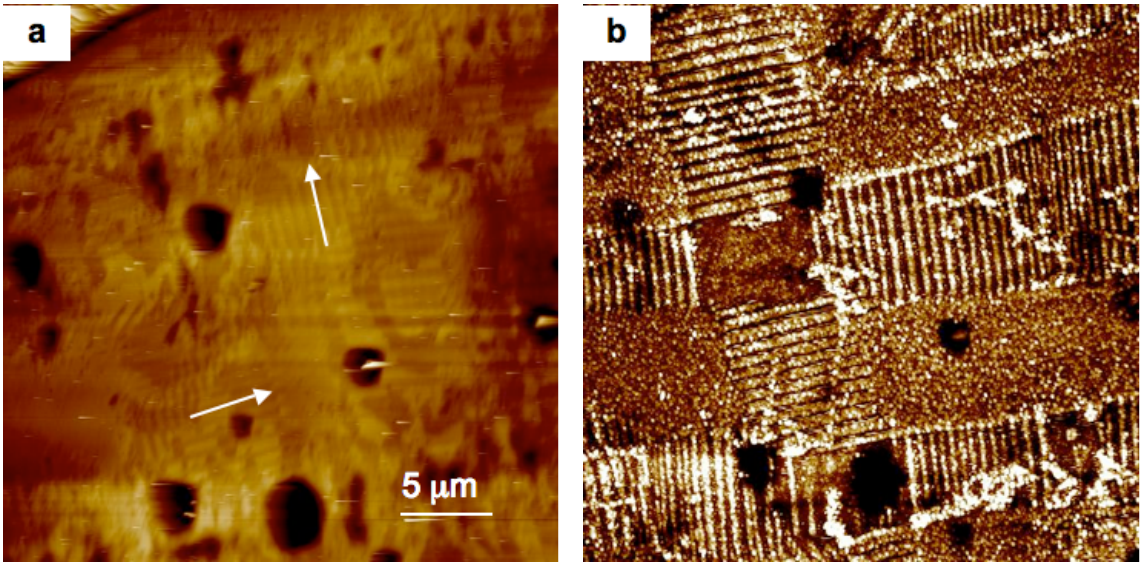


**Figure 8.4.** Topographical AFM images of 10 nm thick $TiO_2$ thin film surface (a) before reaction and (b) after reaction (silver nitrate, 15 seconds). Silver is observed to deposit preferentially in a pattern corresponding to the $BaTiO_3$ domain structure. Black-to-white contrasts are 100 nm and 120nm for (a) and (b), respectively.

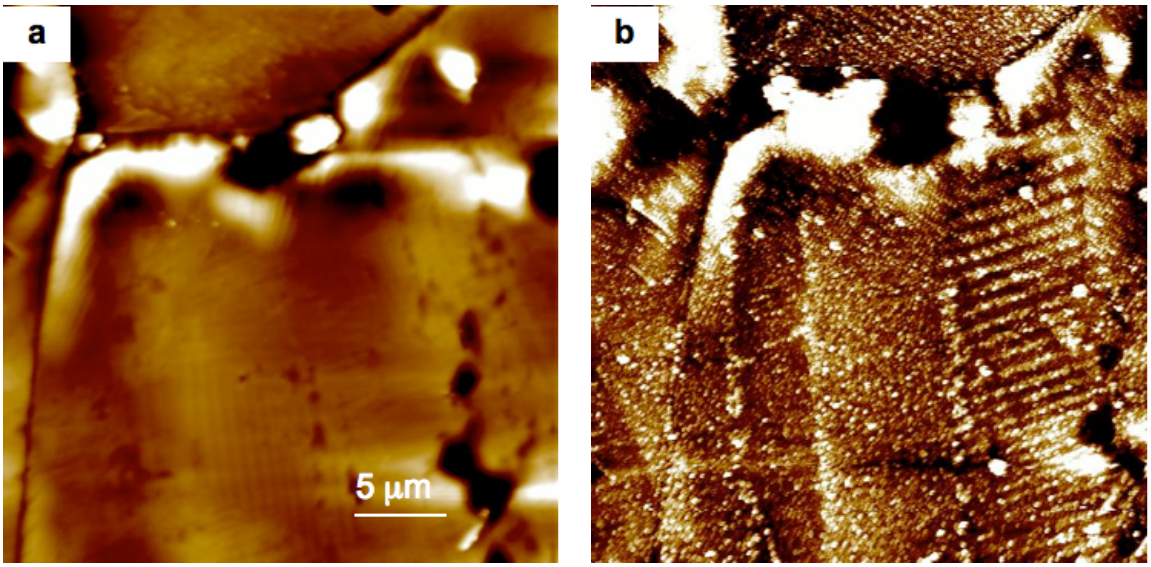


**Figure 8.5.** Topographical AFM images of 30 nm thick $TiO_2$ thin film surface (a) before reaction and (b) after reaction (silver nitrate, 15 seconds). Black-to-white contrasts are 200 nm and 150nm for (a) and (b), respectively.

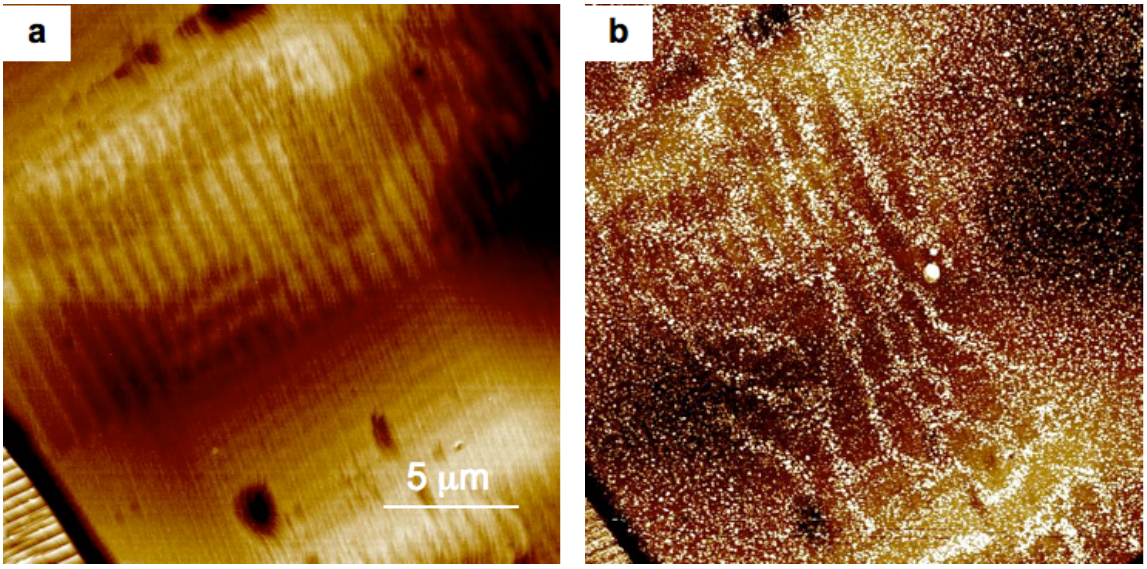


**Figure 8.6.** Topographical AFM images of 50 nm thick $TiO_2$ thin film surface (a) before reaction and (b) after reaction (silver nitrate, 15 seconds). Spatially selective reactivity is observed, but its effect has diminished as compared to the 10 nm film. Black-to-white contrasts are 70 nm and 80 nm for (a) and (b), respectively.

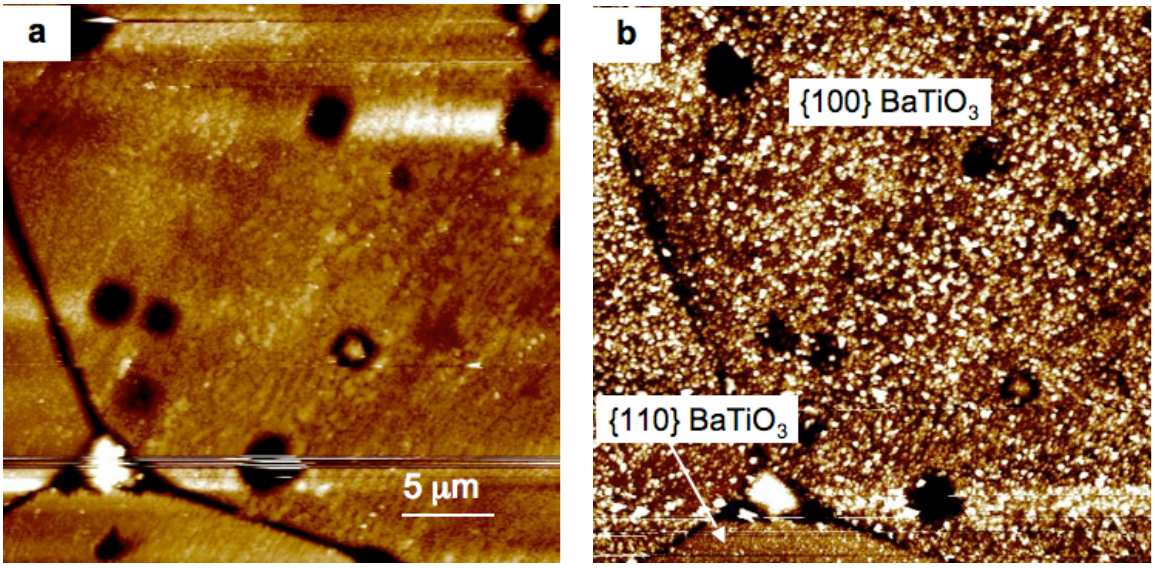


**Figure 8.7.** Topographical AFM images of 100 nm thick $TiO_2$ thin film surface (a) before reaction and (b) after reaction (silver nitrate, 15 seconds). Spatial localization of reaction product is not observed for this film. However, some $TiO_2$ orientation dependent reactivity is observed. It is apparent that the top two grains in the image are considerably more reactive than the grain in the bottom of the image. Black-to-white contrasts are 200 nm and 175 nm for (a) and (b), respectively.

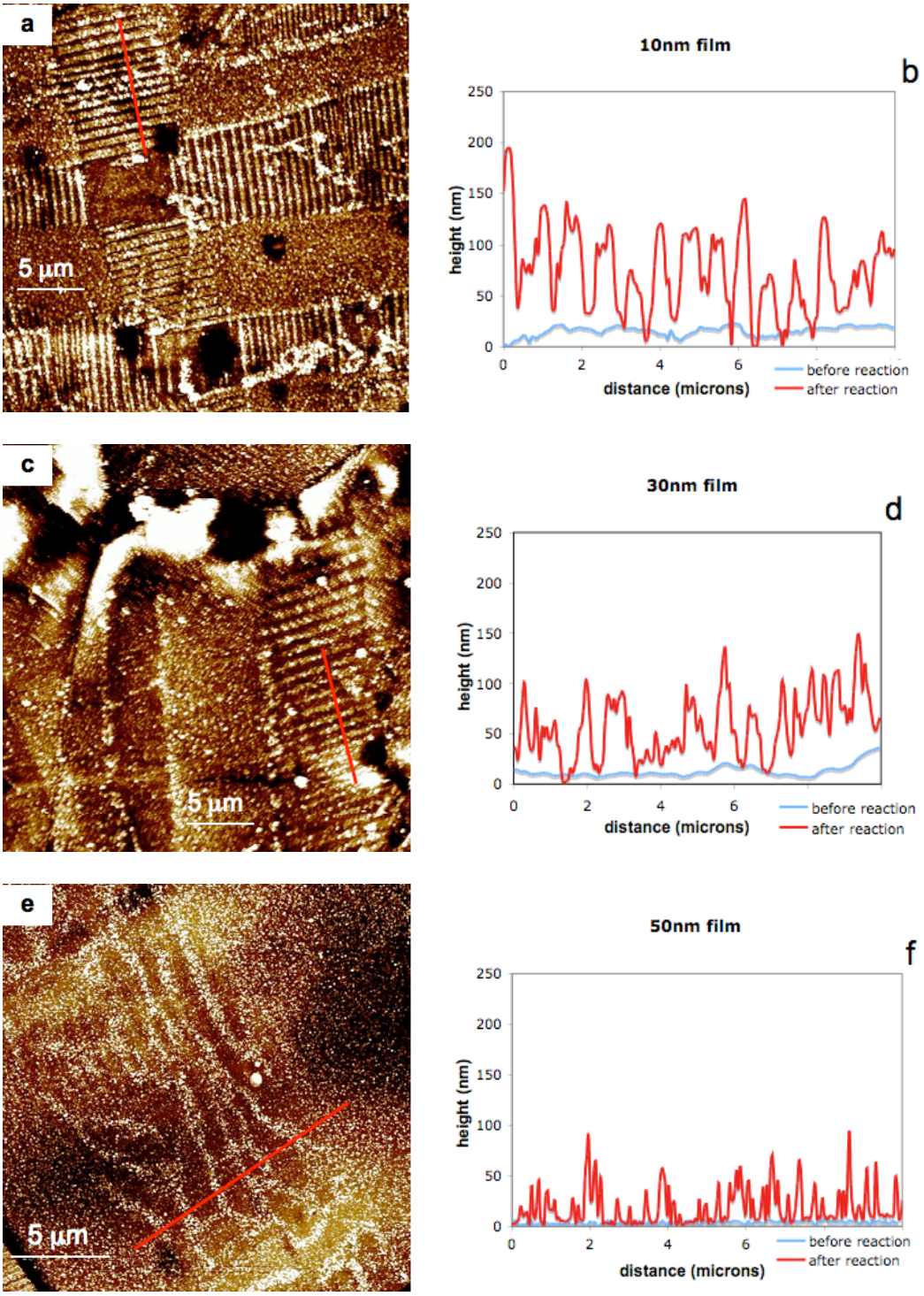


**Figure 8.8.** Topographical AFM images (a), (c) and (e) and height profiles (b), (d) and (f) for reacted $TiO_2$ films. (a) and (b) are for a 10 nm thick film, (c) and (d) are for a 30 nm thick film and (e) an (f) are for a 50 nm thick film. Spatial selectivity diminishes with increasing film thickness.

## 8.4 Reduction and Oxidation Half Reactions as a function of film thickness

In the sections 8.2 and 8.3, we observed that spatial selectivity of the reduction of $Ag^+$ to Ag metal diminished as $TiO_2$ film thickness was increased. In this section, we will compare spatial selectivity of the reduction half reaction ($Ag^+ + e^- = Ag$) and the oxidation half reaction ($Pb^{2+} + 2H_2O = PbO_2 + 4H^+ + 2e^-$) as a function of film thickness. For thin films of $TiO_2$, we observed (in Section 5.2) that oxidation and reduction half reactions occurred in spatially distinct locations and that different domains promoted each reaction. Figure 8.9 shows the two reactions on 15 nm thick $TiO_2$ surfaces. Clear spatial selectivity is evident for both half reactions.

In Fig. 8.10, images of three locations on a thicker film surface (50 nm thick) after reaction in both silver nitrate and lead acetate are shown. For each pair of images, it is still apparent that reduction and oxidation occur on different domains. In the first pair of images (Fig. 8.10(a) and (b)), a set of domain "stripes" is marked by an arrow in both images. It is evident that the reduction reaction has occurred preferentially on thin stripes while the oxidation reaction occurred on the thicker stripes in between. However, spatially selective reactivity seems much more marked for the oxidation reaction than for the reduction reaction. When compared with the thin film case (Fig. 8.9), spatial selectivity of silver deposits seems more diminished than in the case of lead oxide deposits. This is more apparent within the green box drawn in each image. In the case of oxidation, lead oxide has clearly preferentially deposited in a pattern resembling 180° domains. For the reduction half reaction, however, these domains are barely apparent. Similar observations can be made for the other pairs of images (Fig 8.10(c) and (d) and Fig. 8.10(e) and (f)). In general, for the $Pb^{2+}$ oxidation reaction, the difference in

reactivity between preferred domains and neutral domains is clear and the boundary between these domains is crisp, because neutral domains are almost bare. For the reduction reaction the difference between preferred domains and neutral domains is much less significant and the boundary between the two is obscured.

## 8.5 Discussion

The primary result in this chapter is that spatially selective reactivity (for the reduction half reaction) on a film surface diminished as the film thickness was increased from 15 nm to 100 nm. The schematics presented in Fig. 8.11 illustrate a plausible explanation of these observations. Spatially selective reactivity on a thin film surface (a) was explained in Chapter 7. For a film of medium thickness (b), the diminished spatial localization could be attributed to several factors. First, as discussed in Chapter 7, it was proposed that electrons and holes photogenerated in the substrate were responsible for the occurrence of spatially localized reactions on thin film surfaces. For films of medium thickness, a much lower percentage of photogenerated carriers are excited in the substrate. From eq. 2.7, for the 50 nm film, approximately 36% of the total photogenerated carriers are excited in the substrate. Thus, a significant amount of carriers are generated in both the substrate and the film. So, while some carriers (those from the substrate) may still be promoting spatial selectivity of reactions, other carriers (those from the film) will move to the surface and react as on the surface of bulk $TiO_2$. An image of the non-spatially selective reactivity on the surface of $TiO_2$ is provided in Fig. 2.29. Another factor may be the increase in band bending in the film near the interface. From eqs. 2.8-2.10, we know that as the film gets thicker, it is able to screen more charge from the interface so band bending is more pronounced than in the thin film case. As

shown in the diagram, this band bending creates a potential well at the interface (that is deeper than in the case of the thin film). This potential well may act as a trap for photogenerated electrons from the substrate, which would decrease spatially selective reactivity for the reduction reaction. Additionally, as the band bending in the film increases, it is possible that the film band bending is promoting a specific carrier to the surface (as in the work by Inoue et al. [17] discussed in Sections 2.5.4 and 7.4). So, for example, for the case illustrated in Fig. 8.11 (d), the band bending in the film would promote hole transport to the film surface. This counteracts the effect of the substrate (which is providing excess electrons), so spatially selective reactivity could also be diminishing because these two effects are counteracting one another.

For a thick film (c), the majority (60%) of carriers are generated in the film and since reaction behavior is similar to bulk $TiO_2$ we can assume that carriers are no longer being affected by polarization induced band bending in either the substrate or the film.

These results also help shed some light on the observed discrepancies between this study and the works by Inoue et al. [17, 69]. As discussed in Chapter 7, in a study by Inoue et al., the enhancement in photocatalytic activity of a thin film supported by a ferroelectric was explained by the schematic shown in Fig. 2.24. According to the model in Fig. 2.24, the ferroelectric material induced band bending in the semiconducting film. Since the film was thin, the band bending extended to the surface of the film. As a result, when carriers were photogenerated in the film, only one type of carrier (electron or hole) was promoted to the surface and thus one type of half reaction was favored. As shown by Figure 2.24, the reaction favored on the film surface was the opposite of the reaction that would be favored on the bare substrate surface (for the same domain polarization). In the

present experiment, this was not observed; the half reaction preferred on the film surface (for thin films) was the same that would be preferred on the bare substrate.

In the works by Inoue, the ferroelectric substrate used was $LiNbO_3$, which has a much wider band gap (3.9 eV [55]) than the ferroelectric substrates used in this study. In this case, carriers might not be generated in the substrate and would only be generated in the film. In their studies, the effect of the substrate on photocatalytic activity of films was a strong function of film thickness. Photocatalytic activity of films on polar substrates was similar to that of films on non-polar substrates for thin films (~10 nm-20 nm). As the thickness was increased, the photocatalytic activity of films on polar substrates rose dramatically, while that of films on non-polar substrates remained fairly constant. After a certain film thickness was reached, the activity of the films on polar substrates began to decrease until it was again comparable to that of films on non-polar substrates. Contrastingly, in our experiments, the thinnest films (10-20 nm) showed the most enhancement in reactivity from the substrate. A possible explanation for these discrepancies is discussed below.

For the thin films in their studies, the effect from the polar substrate was not substantial enough to affect the reactivity of the film. This could be because the films are very thin and only a small amount of light is absorbed. As a result, not many carriers are photogenerated. This is also the case for the thinner films in the present study, however we still see a spatial localization of reactions because of carriers that are photogenerated in the substrate. As mentioned above, their substrates have a much larger band gap, so it is possible that very few carriers are excited in the substrate. As film thickness is increased, more carriers are created in the film. Initially, as the thickness is increased

further, the amount of photogenerated carriers also increases, and the dipolar field from the ferroelectric is still influencing bands in the film. This may also be the case for the films in our study, however, the effects of carriers excited in the substrate and those excited in the film counteract one another (as explained above for the case of medium thickness films). This is not an issue in the works by Inoue because carriers are likely to only be generated in the film. Eventually, in both the current work and the work of Inoue, the thickness of the film reaches a point where carriers and reactivity are no longer affected by the dipolar field from the substrate.

In this chapter, we also observed that spatially selective reactivity seems to diminish more quickly when the $Ag^{+}$ reduction half reaction is the visible reaction than when the $Pb^{2+}$ oxidation half reaction is the visible reaction. As mentioned in Section 3.2, for each of these cases there is also an invisible half reaction occurring, for which the reaction location is unknown. One possible reason for this involves the deposition of Ag metal onto the surface after the $Ag^{+}$ reduction reaction. Experimentally it has been shown that metal deposited on a surface after reaction has the effect of bending bands downward at the surface near the metal particle (see Fig. 8.12) [47]. Thus, the formation of a metal particle encourages more electrons to come to the surface. In the case of medium thickness films (like the ones shown in Fig. 8.10), we know that carriers come from both the substrate and the film, so both types of carriers are promoted to the surface, regardless of the underlying domain polarization. This is why spatially selective reactivity diminishes with increasing film thickness. However, for $Ag^{+}$ reduction, when some Ag is formed on the "wrong" domain, more electrons are promoted to the surface by the

reaction product, which encourages more reduction reaction on the “wrong” domain. Thus, spatially selective reactivity would be expected to diminish faster in this case.

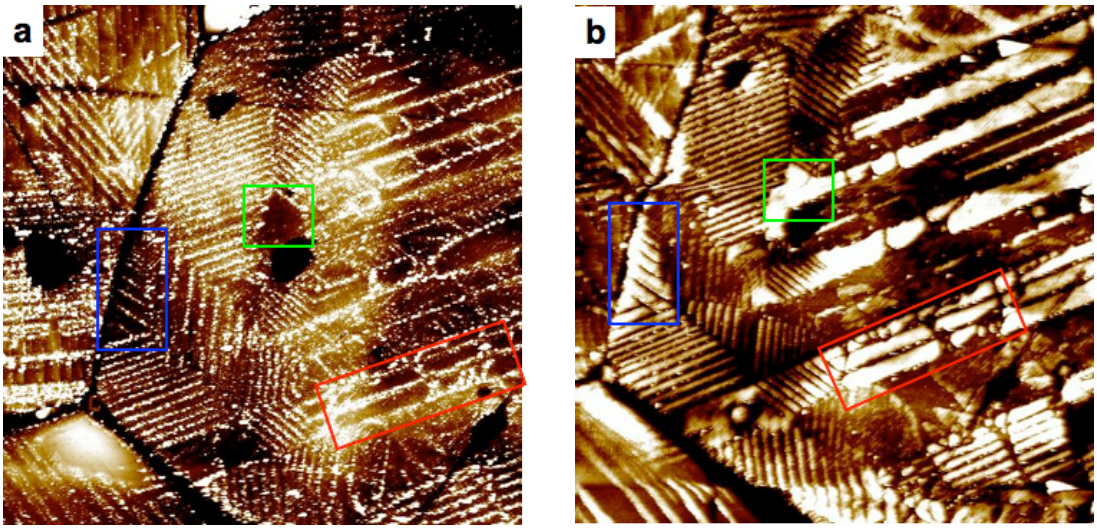


**Figure 8.9.** Topographical AFM images of a 15 nm thick $TiO_2$ film surface (a) after reaction with silver nitrate solution and (b) after reaction in lead acetate solution. Boxes show regions where it is evident that silver and lead oxide have deposited on opposite domains. Black-to-white contrasts are 55 nm and 80 nm, respectively.

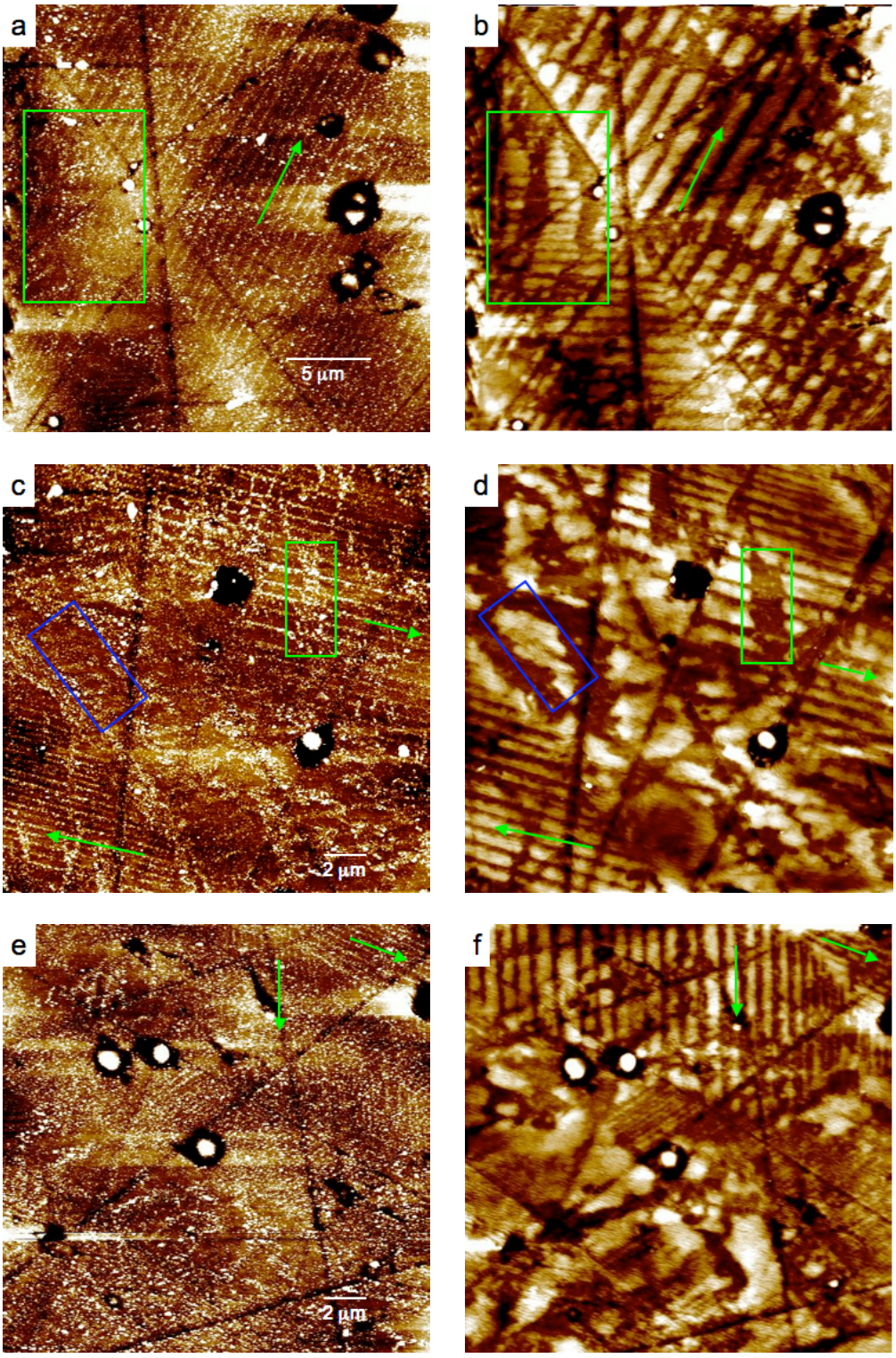


**Figure 8.10.** Topographical AFM images of a 50 nm thick $TiO_2$ film surface. Each row shows a pair of images taken in the same location after reaction with silver nitrate solution (a,c,e) and after reaction in lead acetate solution (b,d,f). Black-to-white contrasts are 80 nm, 70 nm, 40 nm, 40nm, 50 nm, 60 nm, respectively.

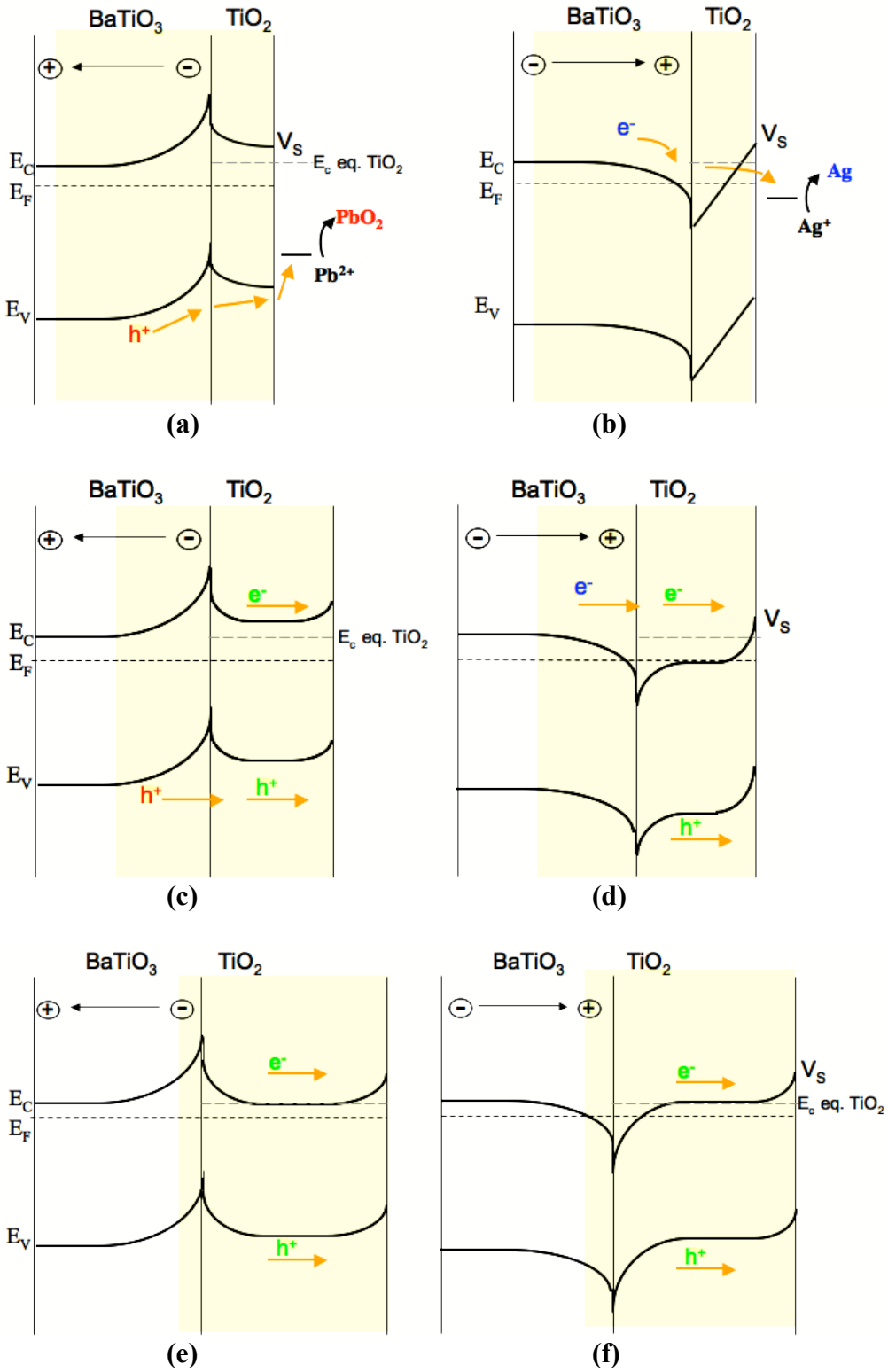


**Figure 8.11.** Schematics illustrating differences between thin (a,b), medium (c,d) and thick (e,f) films. Diagrams a, c, and e show band diagrams for the negative end of the dipole at the film-substrate interface and b,d,f show diagrams for the positive end of the dipole at the film-substrate interface.

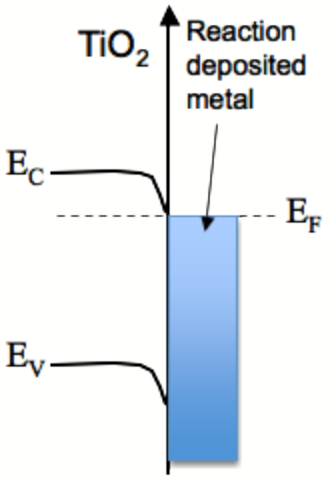


**Figure 8.12.** Schematic showing the effects of a deposited metal particle on the surface.

# 9 Results: Doped Films

## 9.1 Introduction

The purpose of this chapter is to demonstrate the effect of increasing the donor density of the $TiO_2$ films on spatially selective reactivity. As described in section 3.2.1, doped films were produced by dissolving a small amount of $Nb_2O_5$ in $TiO_2$. Nb substitutes on the Ti site and acts as a donor [43]. Based on the amount of impurity added, the carrier concentration in the doped films is estimated to be $3X10^{20}$ /$cm^3$. For undoped films, carrier concentration is estimated to be around $10^{18}$-$10^{19}$/$cm^3$ [71], where carriers probably arise from the presence of oxygen vacancies. This value for the carrier concentration in undoped films is based on values of carrier concentrations for $TiO_2$ measured in another work [71]. As discussed in Sec. 2.5.5, an increase in carrier concentration causes a decrease in the depletion layer width and consequently, band bending becomes steeper. In Chapter 8, increased band bending in the film was hypothesized to be a factor in reducing spatially selective reactivity. Thus, the increased band bending from the higher carrier concentration is expected to diminish spatially selective reactivity.

## 9.2 Results

In Fig 9.1, the distribution of reduced silver on the Nb-doped and undoped films after reaction is compared. All of the images in this figure are of 15 nm thick film surfaces after reaction in silver nitrate solution. The three images in the left column are of undoped films and the three images in the right column are doped films. Each row of

images shows results for a different substrate orientation; in (a) and (b) the substrate has a {100} orientation, in (c) and (d) the substrate has a {110} orientation and in (e) and (f) the substrate has a {111} orientation. In the case of the undoped films, spatially selective reactivity is clearly observed for all three orientations. For the doped films, spatially selective reactivity is not apparent for any of the three orientations. On the doped film surface, grains of unknown orientation were also inspected. Fig. 9.2 shows images of two grains of unknown orientation after reaction in silver nitrate solution. For these locations, spatially selective reactivity is noticeable, but the degree of spatially selective reactivity is clearly diminished compared with the undoped films.

## 9.3 Discussion

A plausible explanation for the difference in reactivity for doped and undoped films is provided by Fig. 9.3. For the same film thickness, it is expected that a much larger amount of band bending can be accommodated in a doped film as compared to an undoped film. As discussed in Section 2.5.2, the slope of band bending is predicted by the Poisson equation:

$$\frac{d^2V}{dx^2} = \frac{qN_{SC}}{\varepsilon} \qquad (9.1)$$

where V is the voltage at the interface (for example, from polarization), ε is the dielectric constant, q is the elementary charge and $N_{SC}$ is the density of compensating charge in the space charge layer (which is equivalent to the carrier concentration). As the carrier

concentration is increased, the slope of band bending becomes steeper. As a result, charge compensation occurs more quickly and the width of band bending is smaller.

In Section 2.5.5, the estimated depletion width for a carrier concentration of $1x10^{18}$ was calculated to be 1620 nm. Repeating this calculation for the current carrier concentration, we see that the estimated depletion width decreases to only 5.4 nm, which means that band bending is significantly steeper.

The steeper band bending in the film is depicted in the Fig. 9.3. We conclude that the steep band bending traps the preferred carrier at the interface, thus diminishing the spatially selectivity of reactions.

Another possibility is that the spatially selective reactivity diminishes because of the presence of ionized donor (Nb) impurities. If carriers photoexcited in the substrate are responsible for spatially selective reactivity, it is possible that the Nb dopant in the film scatters these carriers preventing them from being preferentially driven to the surface [99]. Additionally, Nb dopants may also acts as traps or recombination centers for photoexcited electrons and holes [100]. This could also cause spatially selective reactivity to diminish.

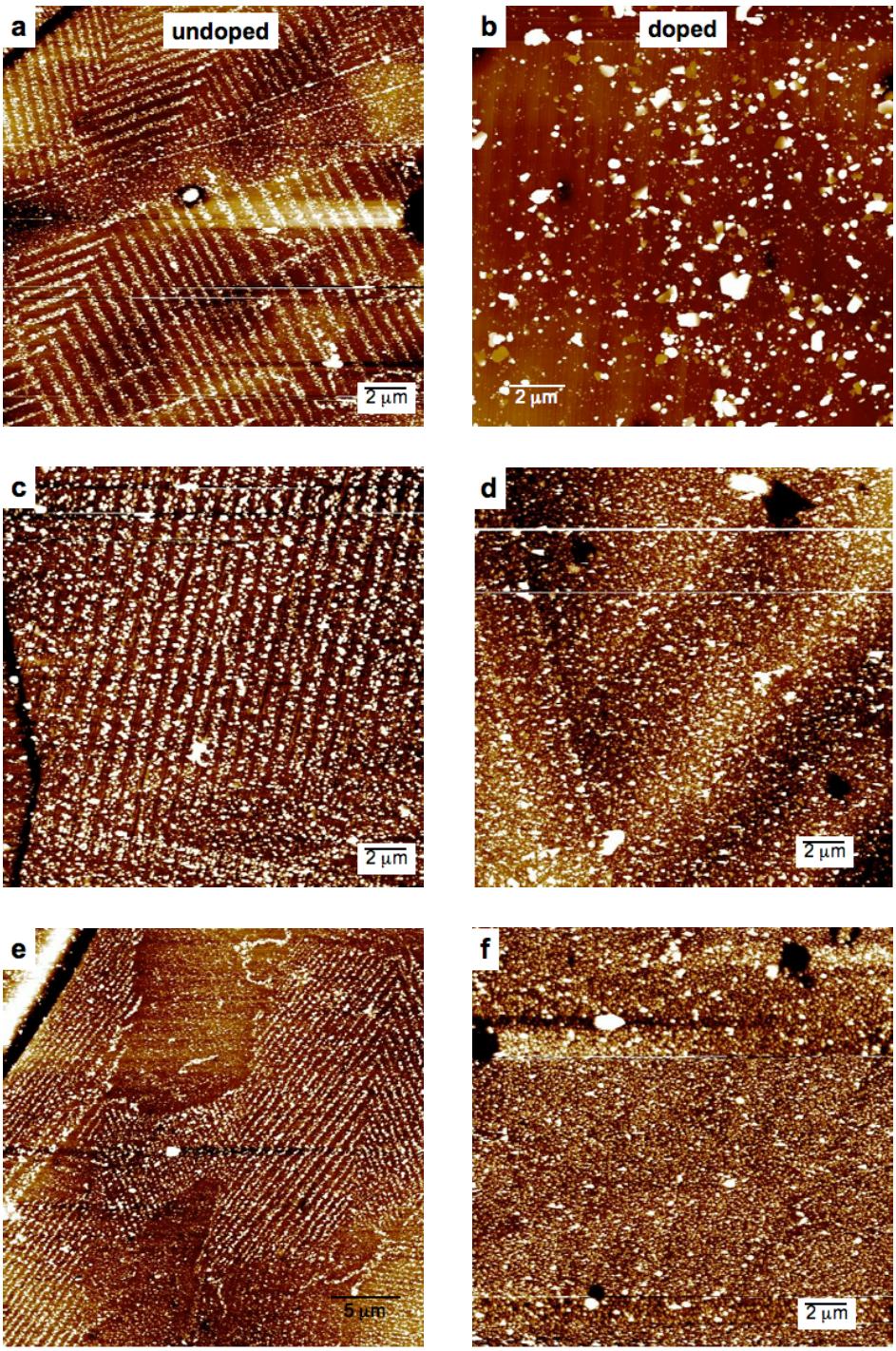


**Figure 9.1.** Topographical AFM images of (a), (c) and (e) undoped 15 nm thick $TiO_2$ film surfaces after reaction in silver nitrate solution (b), (d) and (f) doped 15 nm thick $TiO_2$ thin film surfaces after reaction in silver nitrate solution. Central grains in (a) and (b) are of the {100} substrate orientation, (c) and (d) {110} substrate orientation and (e) an (f) {111} substrate orientation. Black-to-white contrasts are 100 nm, 80 nm, 100 nm, 80 nm, 100 nm and 80 nm, respectively.

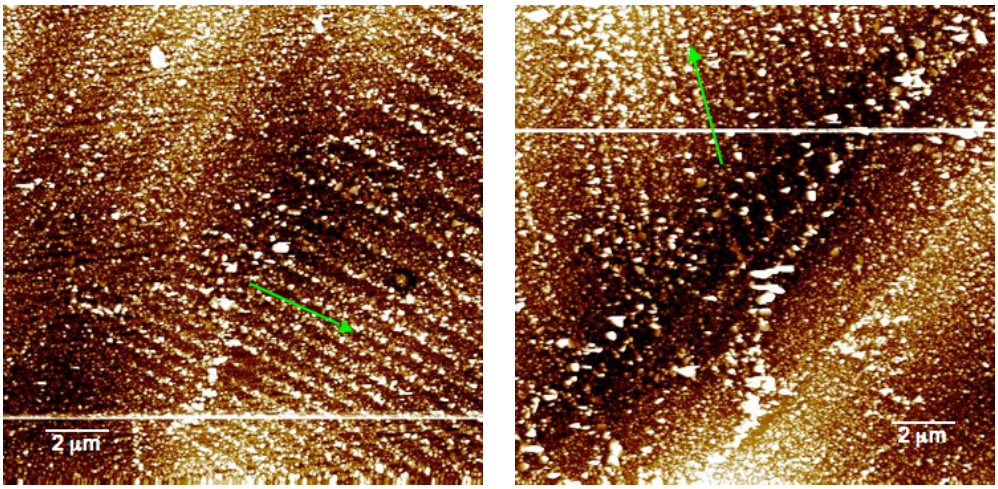


**Figure 9.2.** Topographical AFM images of doped 15 nm thick $TiO_2$ thin film surfaces after reaction in silver nitrate solution. Black-to-white contrasts are 80 nm for both images.

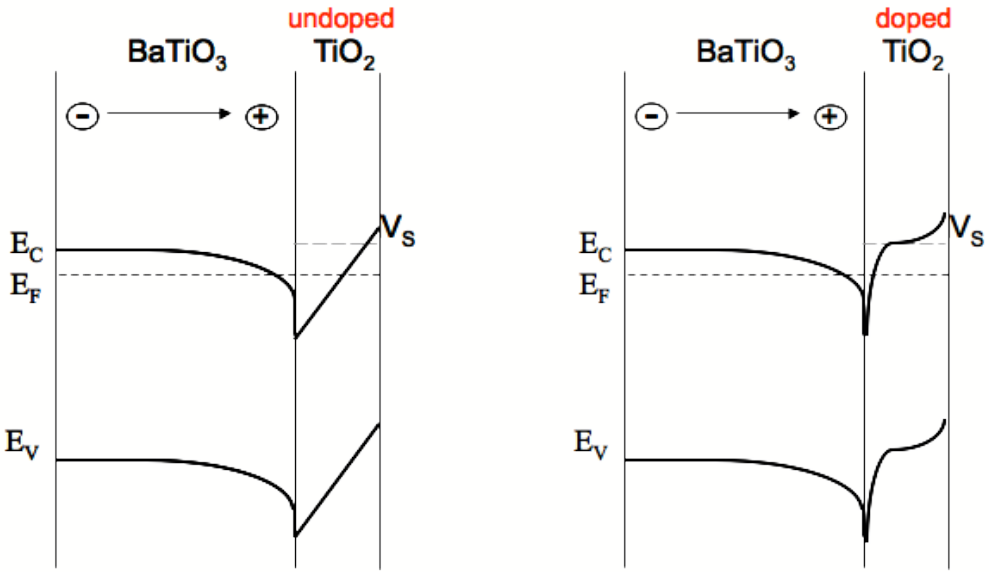


**Figure 9.3.** Schematics illustrating the proposed effect of doping on bands in the film.

# 10 Results: Effect of orientation on reactivity

## 10.1 Introduction

As mentioned in the background section, grain orientation can have a significant impact on reactivity [83]. Because we are interested in finding the conditions that lead to the highest reactivity, in this section we will examine the effects of substrate ($BaTiO_3$) and film orientation on reactivity.

## 10.2 $BaTiO_3$ Results

Fig. 10.1 shows images of {100}, {110} and {111} oriented substrate surfaces after reaction in silver nitrate solution. For all three orientations, spatially selective reactivity is clearly observed. The most noticeable difference in reactivity is observed for the {110} orientation. The amount of reaction product on the surface of this orientation seems smaller compared to the other two. Inspection of height differences between reactive and neutral areas on several {110} grains confirmed this visual observation. For {110} grains, height differences were near 25 nm. In comparison, differences for {111} and {100} orientations were 45 nm and 40 nm, respectively. These results are somewhat consistent with those obtained by Giocondi et al. [59] for faceted $BaTiO_3$ crystals. In this study, the relative reactivity for crystal faces were ranked from highest to lowest as: {100} > {111} >{110}.

As mentioned in Section 2.6.1 of this document, the orientation of the polarization vector with respect to a grain's surface normal is expected to influence the amount of spatially selective reactivity. When the polarization vector is oriented normal to or close

to normal to the surface (i.e. for {100} oriented grains), a larger component of the dipolar field will be directed towards the surface. This may be why the {100} orientation has more pronounced spatially selective reactivity than the {110} orientation, for which the polarization vector would be inclined at an angle of 45° to the surface. However, there is no significant difference in spatially selective reactivity between the {100} orientation and the {111} orientation even though the polarization vector would be inclined at an angle of 55° to the {111} surface normal. Thus, the orientation of the polarization vector with respect to the surface does not appear to have a dominant role in determining the relative photochemical reactivity of different orientations.

It was also mentioned in Section 2.6.1 that the dielectric constant for $BaTiO_3$ is highest for directions inclined at an angle of around 50° to the <100>. A high dielectric constant would increase charge separation. Because the <111> is close to 50° away from the <100>, this high dielectric constant could explain the high spatially selective reactivity of the {111} orientation, however, in this case the dielectric constant for the <110> would also be expected to be relatively high. Hence, the observable differences in reactivity may be partially attributed to the factors discussed above or could be a result of other orientation dependent characteristics, such as surface morphology.

## 10.3 $TiO_2$ films

Comparisons of reactivity were also made for samples with thin films of titania. Fig. 10.2 shows images for 15 nm thick $TiO_2$ film surfaces after reaction. The orientations of these films were determined based on the findings of Chapter 4. Images (a) and (b) are of the {001} anatase surface ({100} substrate orientation), (c) and (d) are of the {110} rutile surface ({110} substrate orientation), and (e) and (f) are of the {100}

rutile surface ({111} substrate orientation). For all three orientations, the amount of reaction product on the film surfaces appears to be slightly larger than on the bare surfaces of the same orientation. Quantitatively, the average height difference (between reactive and neutral areas) was 50 nm for {100} anatase films and {100} rutile films and 60 nm for {110} rutile films.

For films of medium thickness (~50 nm), spatially selective reactivity is diminished compared to that for thin films. Figure 10.3 shows images of medium films of several different unknown orientations after reaction in silver nitrate. Here, the most noticeable impact of orientation is that, for this film thickness, some orientations still show spatially selective reaction behavior, and some do not. For the images shown, two of the images contain some noticeable evidence of spatially selective reactivity, while for the other image, no spatially selective reactivity is observed. So, it is apparent that the effect of the ferroelectric polarization fades faster for some orientations than others.

In Fig. 10.4, an image of a thick (100 nm) film is presented. For this case where spatially selective reactivity is no longer observed, we observe that reaction behavior is controlled by the anisotropic photochemical reactivity of $TiO_2$ (see Fig. 2.29).

It is interesting to note that while reactivity is anisotropic for bulk $TiO_2$, there was no significant difference between reactivities for thin films of $TiO_2$ of varying orientation. Hence, it appears that the presence of the underlying ferroelectric polarization overwhelms the factors that generally cause orientation dependent reactivity on the $TiO_2$ surface. This is illustrated for one orientation in Figs. 10.5 and 10.6. Here, reactivity is compared for a thin film and a thick film of the same orientation ({110} rutile). In these figures, images of both a thin and thick film before and after reaction in

silver nitrate solution are shown. For each set of images, height profiles taken from before and after images are also shown. For the thick film, height profiles from the before and after images are very similar. Heights after reaction are generally less than 50 nm larger than heights before reaction. This suggests that only a small amount of silver has been deposited on the surface, which indicates that the {110} rutile orientation has a low reactivity. This observation is consistent with previous work by Lowekamp [83], in which a low reactivity was also observed for {110} rutile (see Fig. 2.30). In contrast, for the thin film, heights after reaction are much greater, typically between 50 and 150 nm larger than for the before image. Thus, the presence of the ferroelectric overwhelmed the effects of anisotropic reactivity, and furthermore, it appears to have improved the reactivity of {110} rutile.

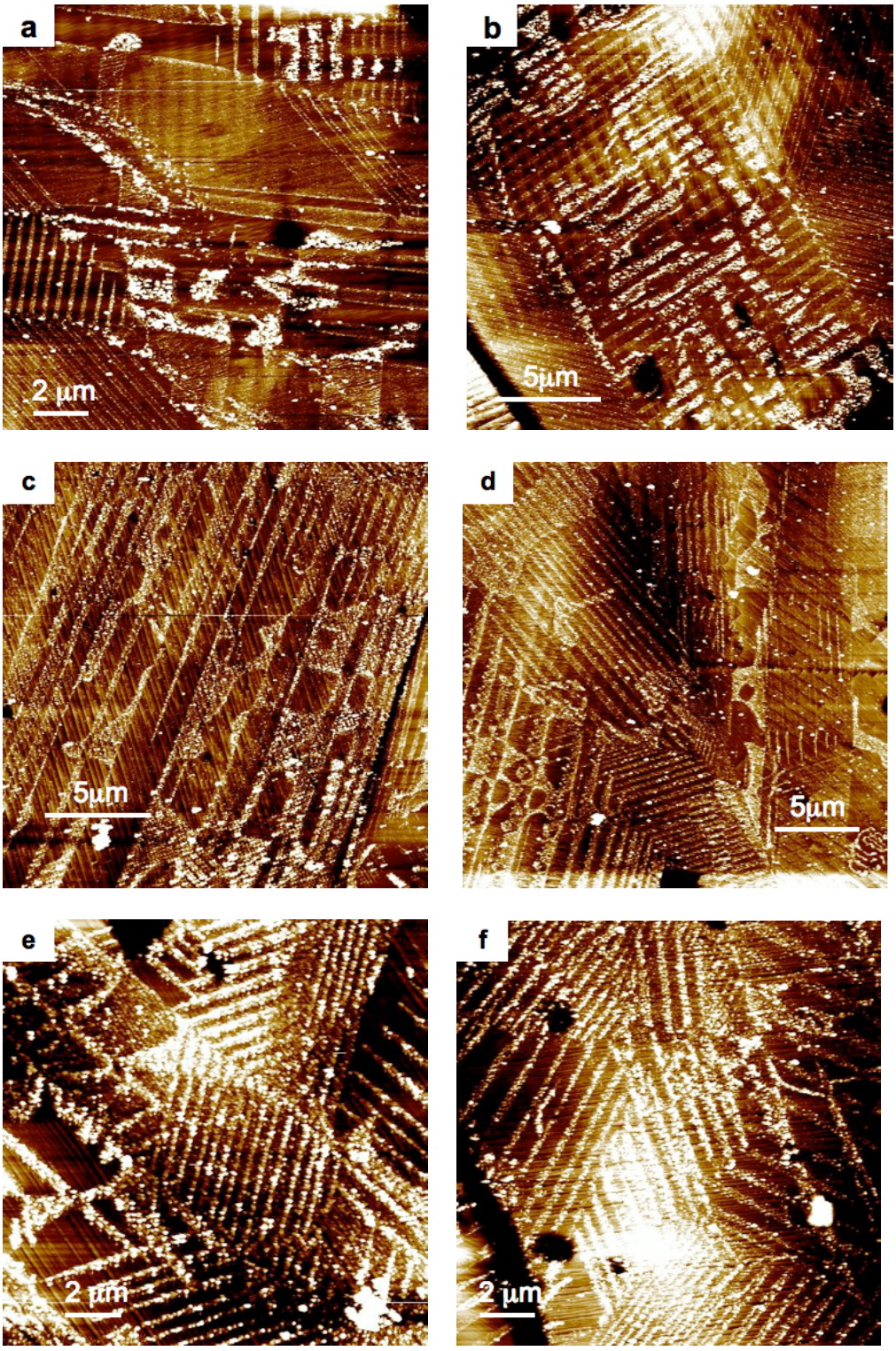


**Figure 10.1.** Images of $BaTiO_3$ surfaces after reaction in silver nitrate solution. Images (a) and (b) are of the {100} surface, (c) and (d) are of {110} and (e) and (f) are of {111}. Black to white contrasts are 40 nm, 40 nm, 50 nm, 50 nm, 60 nm, 60nm, respectively.

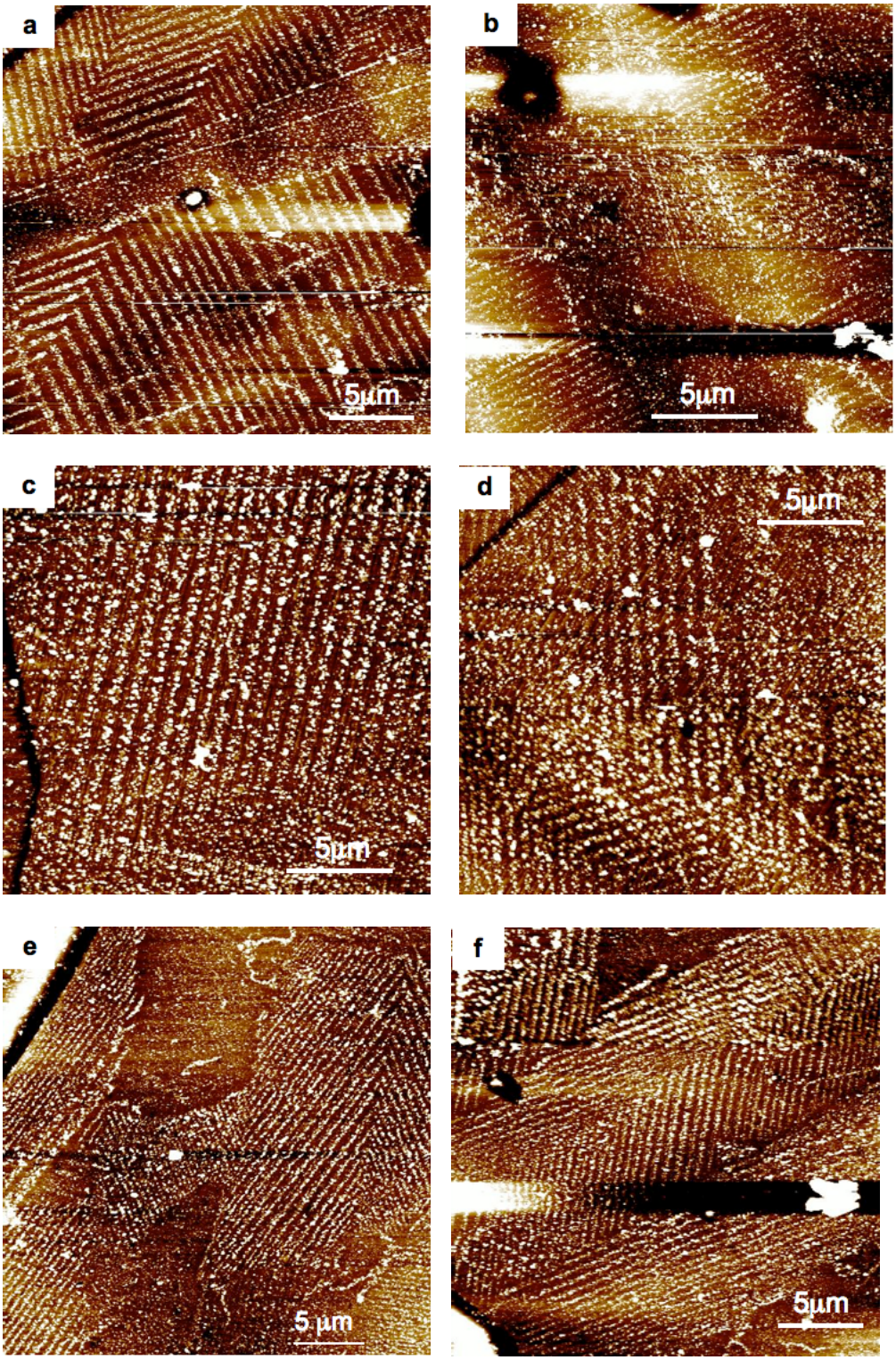


**Figure 10.2.** Images of $TiO_2$ surfaces after reaction in silver nitrate solution. Images (a) and (b) are of the film on the {100} $BaTiO_3$ surface, (c) and (d) are of the film on the {110} $BaTiO_3$ surface and (e) and (f) are of the film on the {111} $BaTiO_3$ surface. Black to white contrasts are 70 nm, 70 nm, 90 nm, 100 nm, 70 nm, 70nm, respectively.

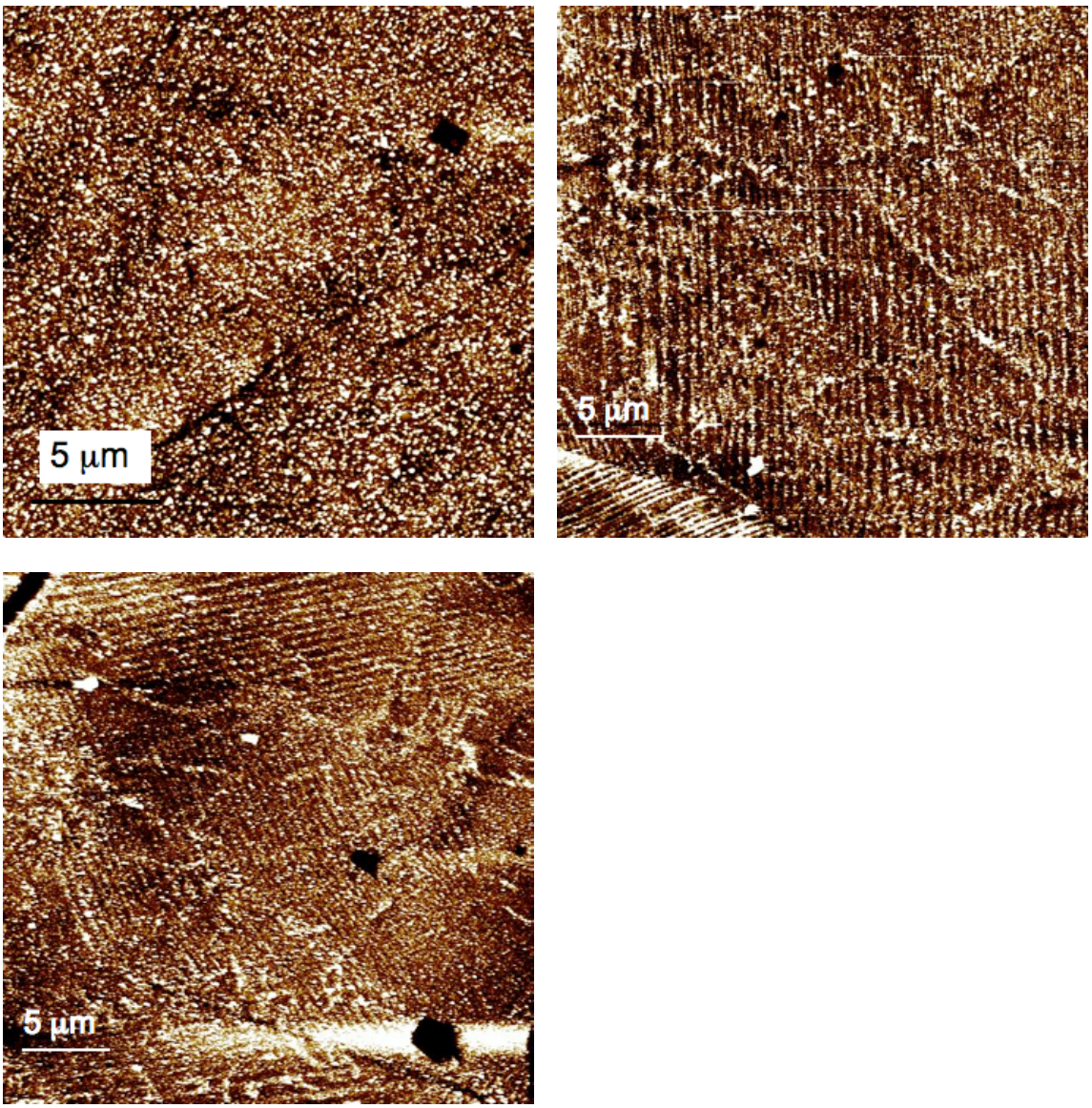


**Figure 10.3.** Topographical AFM images of 50 nm thick $TiO_2$ film surfaces after reaction. Silver is observed to deposit preferentially in the bottom and top right images. Deposition is uniform for the grain in the top left. Black-to-white contrasts are 80 nm (top left), 70 nm (top right) and 70 nm (bottom).

**Figure 10.4.** Image of a thick $TiO_2$ film illustrating anisotropic reactivity.

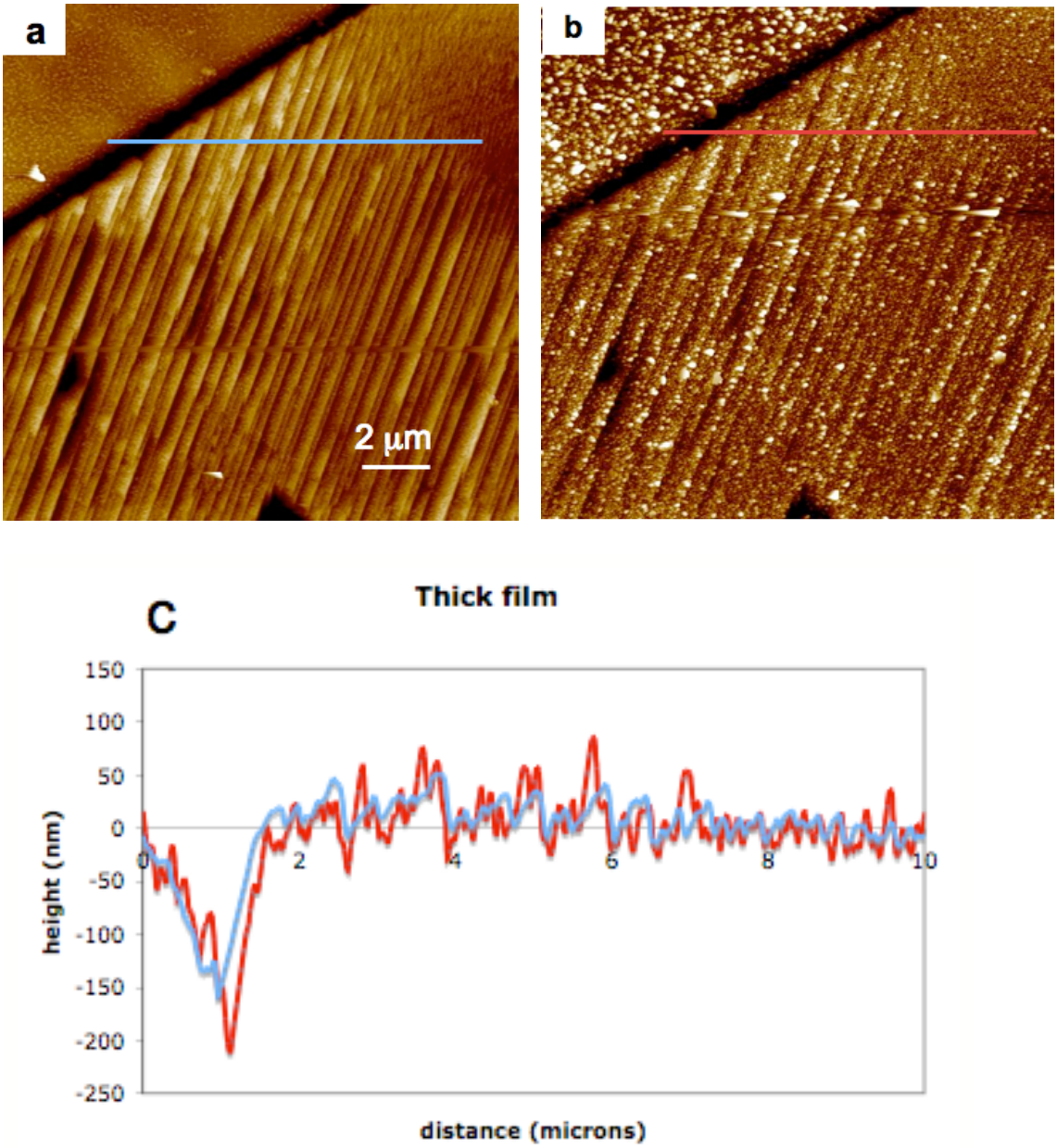


**Figure 10.5.** (a) is a topographical AFM image of the surface of a 100 nm thick film on {110} $BaTiO_3$, (b) is the same location after reaction with silver nitrate (15 seconds). In (c) height profiles of the blue line marked in (a) and the red line marked in (b) are shown. Black to white contrasts are 150 nm and 175 nm.

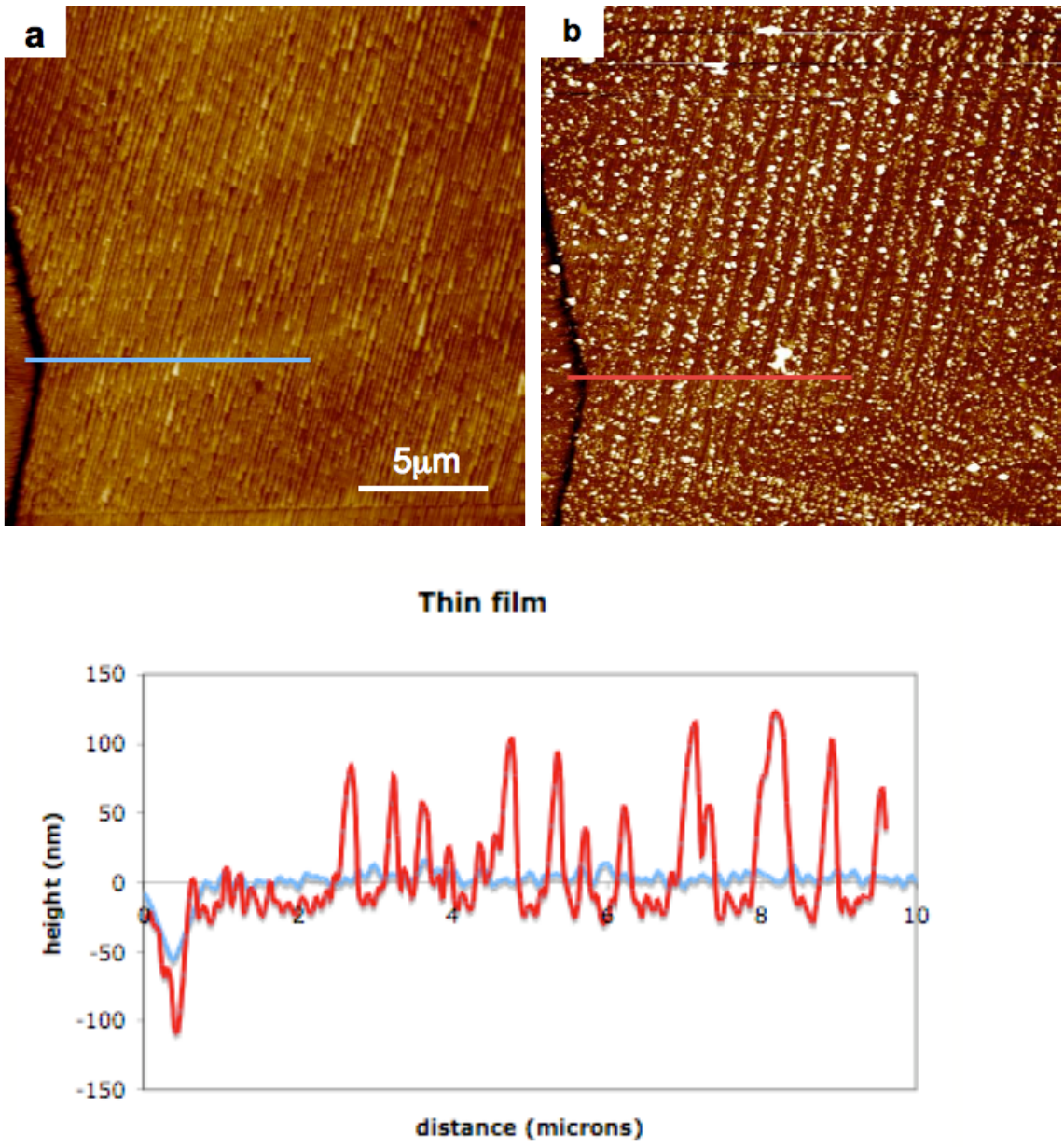


**Figure 10.6.** (a) is a topographical AFM image of the surface of a 15 nm thick film on {110} $BaTiO_3$, (b) is the same location after reaction with silver nitrate (15 seconds). In (c) height profiles of the blue line marked in (a) and the red line marked in (b) are shown. Black to white contrasts are 80 nm and 175 nm.

# 11 Conclusions

## 11.1 Effect of Ferroelectric Substrates on the Reactivity of a Thin Film

The primary conclusion of the work in this thesis is that the dipolar field in an underlying ferroelectric substrate can influence the photochemical reactivity of a protective thin film. Photochemical oxidation and reduction reactions were observed to occur in different locations on $TiO_2$ film surfaces supported by both $BaTiO_3$ and $BiFeO_3$ ferroelectric substrates. Because this effect is not observed for bulk $TiO_2$ [83], it is assumed that the spatial separation of reactions occurs as a result of the dipolar field from the ferroelectric.

Experiments performed in Chapter 7 suggested that when the positive end of the dipole intersected the substrate surface, reduction reactions were promoted on the thin film surface, while the negative end of the dipole promoted oxidation reactions on the film surface. It was concluded that electrons and holes photogenerated in the substrate were responsible for the observed spatial selectivity on the film surface. In the substrate, the dipolar field drives one type of carrier (electron and hole) to the film/substrate interface while the other is driven away. Because for thin films, the majority of carriers are photogenerated in the substrate, the preferred carrier (at the interface) makes up the majority of carriers available for reaction. Consequently, a majority of either electrons or holes is promoted to the film surface, and one type of reaction (oxidation or reduction) is favored.

## 11.2 Conclusions

### *11.2.1 Effect of substrate conductivity type (i.e. n-type or p-type)*

In this work, both n-type ($BaTiO_3$) and p-type ($BiFeO_3$) substrates were used. Consequently, two types of heterojunctions, n/n and p/n were formed at the interface between the substrate and the film. For both types of heterojunction, the polarization was observed to be the dominant factor in influencing photochemical reactivity on the film surface. As discussed in Chapter 5, oxidation and reduction reactions were observed to occur in different locations on the film surface for both substrates.

### *11.2.2 Effect of film thickness*

In Chapter 8, it was observed that spatial localization of reactions on the film surface diminished as the film thickness was increased from 15 nm to 100 nm. The diminished spatially selective reactivity was attributed to the increase in band bending in the film at the film/substrate interface as well as the increase in the number of carriers being photogenerated in the film as thickness was increased. Both of these factors diminish the effects of photogenerated carriers in the substrate, which were concluded to be responsible for spatially selective reactivity on the film surface.

### *11.2.3 Effect of Film Carrier Concentration*

As the carrier concentration in the film was increased, the effect of the ferroelectric was diminished. This was attributed to steeper band bending in the film at the film/substrate interface for films with higher carrier concentration. This band

bending hinders the transport of preferred substrate carriers to the film surface and thus the preference for a specific reaction is diminished.

### *11.2.4 Effect of $BaTiO_3$ and $TiO_2$ orientation and phase*

The orientation relationships between $BaTiO_3$ substrates and $TiO_2$ films were explored and are summarized below:

{100} $BaTiO_3$ || {001} anatase

{110} $BaTiO_3$ || {110} rutile

{111} $BaTiO_3$ || {100} rutile

The reactivities of these three orientation were compared and no significant differences were observed. This was interesting because the reactivity of $TiO_2$ varies significantly with orientation [80-85], and for all three orientations studied here the reactivities were comparable. Hence, it appears that the effect from the dipolar field overwhelms the effect of anisotropic reactivity in $TiO_2$.

Additionally, the presence of the ferroelectric substrate was observed to enhance the photochemical reactivity of the {110} rutile orientation. This orientation has been previously observed to have a relatively low reactivity for reduction of silver [83]. However, thin films of rutile {110} grown on ferroelectric substrates were observed to have high reactivities for the reduction of silver.

# References


1. Fujishima, A., and Honda, K., Nature, 1972. **238**: p. 37.
2. Gratzel, Nature, 2001. **414**: p. 338.
3. Kudo, A., Miseki, Y., Chemical Society Review, 2008. **38**: p. 253-273.
4. Kitano, M., Tsujimaru, K., Anpo, M., Topics in Catalysis, 2008. **49**: p. 4-17.
5. Navarro, R.M., Sanchez-Sanchez, M.C., Alvarez-Galvan, M.C., del Valle, F., and Fierro, J.L.G., Energy Environ. Sci., 2009. **2**: p. 35-54.
6. Osterloh, F.E., Chem. Mater., 2008. **20**: p. 35-54.
7. Kudo, A., Journal of the Ceramic Society of Japan, 2001. **109**: p. S81-S88.
8. Domen, K., *Surface Photochemistry*, ed. M. Anpo. 1996, Chichester: J. Wiley and Sons.
9. Currao, A., Chimia, 2007. **61**: p. 815-819.
10. Kato, H., Asakura, K., and Kudo, A., *2003.* Journal of the American Chemical Society. **125**: p. 3082-3089.
11. Kalinin, S.V., Bonnell, D.A., Alvarez, T., Lei, X., Hu, Z., Ferris, J.H., Zhang, Q., Dunn, S., Nano Letters, 2002. **2**: p. 589-593.
12. Giocondi, J., Rohrer, G.S., Journal of Physical Chemistry B, 2001. **105**: p. 8275-8277.
13. Giocondi, J., and Rohrer, G.S., Chem. Mater., 2001. **13**: p. 241-242.
14. Jones, P.M., Gallardo, D.E., Dunn, S., *2008.* Chemistry of Materials. **20**: p. 5901-5906.
15. Dunn, S., Jones, P.M., Gallardo, D.E., Journal of the American Chemical Society. **129**: p. 8724-8728.
16. Giocondi, J. 2003, Carnegie Mellon University.
17. Inoue, Y., Sato, K., and Suzuki, S., Journal of Physical Chemistry, 1985. **89**: p. 2827.
18. Lines, M.E. and A.M. Glass, *Principles and Applications of Ferroelectrics and Related Materials*. 2001, New York: Oxford University Press.
19. Kwei, G.H., Lawson, A.C., Billinge, S.J.L., and Cheong, S.-W, J. Phys. Chem., 1993. **97**: p. 2368-2377.
20. Merz, W.J., Physical Review, 1953. **91**: p. 513.
21. Callister, W.D., *Materials Science and Engineering: An Introduction*. 2000, New York: John Wiley and Sons Inc.
22. Forsbergh, P.W., Physical Review, 1949. **76**: p. 1187.
23. Giocondi, J. 2003, Carnegie Mellon Ph. D. Thesis.
24. Basu, S.R., Martin, L.W., Chu, Y.H, Gajek, M., Ramesh, R., Rai, R.C., Xu, X., Musfeldt, J.L. , Applied Physics Letters, 2008. **92**: p. 091905.
25. Chu, Y.H., Zhao, T., Cruz, M.P., Zhan, Q., Yang, P.L., Martin, L.W., Huijben, M., Yang, C.H., Zavaliche, F., Zheng, H., and Ramesh, R., Applied Physics Letters, 2007. **90**: p. 252906.
26. Neaton, J.B., Ederer, C., Waghmare, U.V., Spaldin, N.A, and Rabe, K.M., Physical Review B, 2005. **71**: p. 014113.
27. Zavaliche, F., Shafer, P., Ramesh, R., Cruz, M.P., Das, R.R., Kim, D.M., Eom, C.B, Applied Physics Letters, 2005. **87**: p. 252902.
28. Shvartsman, V.V., Kleemann, W., Haumont, R., Kreisel, Applied Physics Letters, 2007. **90**: p. 172115.

29. Bard, A.J., Parsons, R., and Jordan, J., *Standard Potentials in Aqueous Solutions*. 1985, New York: Marcel Dekker.
30. Mulliken, Journal of Chemical Physics. **2**: p. 782-793.
31. Mulliken, Journal of Chemical Physics. **3**: p. 573-585.
32. Sanderson, R.T., Journal of the American Chemical Society. **105**: p. 2259.
33. Sanderson, R.T., *Chemical Periodicity*. 1960, New York: Reinhold.
34. Butler, M.A., and Ginley, D.S., Journal of the Electrochemical Society, 1978. **125**: p. 228.
35. Nozik, A.J., Annual Review of Physical Chemistry, 1978. **29**: p. 189-222.
36. Cardona, M., Physical review, 1965. **140**: p. 651.
37. Landolt-Bornstein. Numerical Data and Functional Relationships in Science and Technology, ed. O. Madelung, et al. Vol. III/17g. 1984, Berlin: Springer.
38. Ihlefeld, J.F., Podraza, N.J., Liu, Z.K., Rai, R.C., Xu,X., Heeg, T., Chen, Y.B., Li, J., Collins, R.W., Musfeldt, J.L., Pan, X.Q., Schubert, J., Ramesh, R., and Schlom, D.G., Applied Physics Letters, 2008. **92**: p. 142908.
39. Hauser, A.J., Zhang, J., Mier, L., Ricciardo, R.A., Woodward, P.M., Gustafson, T.L., Brillson, L.J., Yang, F.Y., Applied Physics Letters, 2008. **92**: p. 222901.
40. Giocondi, J.L., Salvador, P.A., and Rohrer, G.S., Topics in Catalysis, 2007. **44**(4): p. 529-533.
41. Salehi, H., Shahtahmasebi, N., and Hosseini, S.M., Eur. Phys. J. B 2003. **32**: p. 177-180.
42. Morrison, S.R., *Electrochemistry at Semiconductor and Oxidized Metal Electrodes*. 1980, New York: Plenum Press.
43. Bak, T., Nowotny, J., Rekas, M., Sorrell, C.C., Journal of the Physical Chemistry of Solids, 2003. **64**: p. 1043-1067.
44. Nowotny, M.K., Bak, T., Nowotny, J., Journal of Physical Chemistry B, 2006. **110**: p. 16270.
45. Bard, A.J., Science, 1980(207): p. 139-144.
46. Hope, G.A., and Bard, A.J., Journal of Physical Chemistry, 1983. **87**: p. 1979-1984.
47. Kaneko, M., and Okura, I., *Photocatalysis: Science and Technology*. 2002, New York: Springer.
48. Fridkin, V.M., Ferroelectrics, 1984. **53**: p. 169-87.
49. Brody, P.S., Solid State Communication, 1973. **12**: p. 673.
50. Brody, P.S., Journal of Solid State Chemistry, 1975. **12**: p. 193-200.
51. Brody, P.S.a.C., F., J. Elect. Mater., 1975. **4**: p. 955-71.
52. von Baltz, R., Phys. Stat. Sol. (b), 1978. **89**: p. 419-29.
53. Glass, A.M., von der Linde, D., and Negran, T.J., Applied Physics Letters, 1974. **25**: p. 233-35.
54. van Damme, H., and Hall, W.K., Journal of Catalysis, 1981. **69**: p. 371-383.
55. Hanson, J.N., Rodriguez, B.J., Nemanich, R.J., Gruverman, A., Nanotechnology, 2006. **17**: p. 4946-4949.
56. Haussmann, A., Milde, P., Erler, C., Eng, L.M., Nanoletters, 2009. **9**: p. 763-768.
57. Inoue, Y., Yoshioka, I., and Sato, K., J. Phys. Chem., 1984. **88**: p. 1148-1151.
58. Inoue, Y., Sato, K., Sato, K., Miyama, H., Journal of Physical Chemistry 1986. **90**: p. 2809-2810.

59. Giocondi, J., and Rohrer, G.S., Topics in Catalysis, 2008. **49**: p. 18-23.
60. Milnes, A.G., and Feucht, D.L., *Heterojunctions and Metal-Semiconductor Junctions*. 1972, New York: Academic Press.
61. Morrison, F.D., Sinclair, D.C., and West, A.R., Journal of the American Ceramic Society, 2001. **84**: p. 531-538.
62. Prosandeyev, S.A., Fisenko, A.V. Riabchinski, A.I., Osipenko, I.A., Raevski, I.P., and Safontseva, N., J. Phys,: Condens. Matter, 1996. **8**: p. 6705.
63. Yang, H., et al., Applied Physics Letters, 2008. **92**: p. 102113.
64. Yang, H.e.a., Applied Physics Letters, 2009. **95**: p. 062909.
65. Wurfel, P., and Batra, I.P., Physical Review B, 1973. **8**: p. 5126.
66. Watanabe, Y., Physical Review B, 1999. **59**: p. 11257.
67. Watanabe, Y., Solid State Ionics, 1998. **108**: p. 59.
68. Yeredla, R.R., and Xu, H.F., Journal of Physical Chemistry C, 2008. **112**: p. 532-539.
69. Inoue, Y., et al., J. Phys. Chem., 1985. **89**: p. 5184.
70. Albery, W.J., and Bartlett, P.N., Journal of the Electrochemical Society, 1984. **131**: p. 315.
71. Breckenridge, R., and Hosler, W., Physical Review, 1953. **91**: p. 793
.
72. Du, X., Wang, Q., Belegundu, U., Bhalla, A., and Uchino, K., Materials Letters, 1999. **40**: p. 109
.
73. Lotnyk, A., Senz, S., and Hesse, D., Thin Solid Films, 2007. **515**: p. 3439.
74. Weng, X., Fisher, P., Skowronski, M., Salvador, P.A., and Maksimov, O., Journal of Crystal Growth, 2008. **310**: p. 545.
75. Hsieh, C.C., Wu, K.H., Juang, J.Y., Uen, T.M., Lin, J.Y., and Gou, Y.S., Journal of Applied Physics, 2002. **92**: p. 2518.
76. Yamamoto, S., Sumita, T., Yamaki, T., Miyashita, A., and Naramoto, H., Journal of Crystal Growth, 2002. **237-239**: p. 569-573.
77. Lotnyk, A., Senz, S., and Hesse, D., Solid State Ionics, 2006. **177**: p. 429.
78. Lotnyk, A., Senz, S., and Hesse, D., Journal of Physical Chemistry C, 2007. **111**: p. 6372.
79. Maruska, H.P.a.G., A.K., Sol. Energy, 1978. **20**: p. 443.
80. Taguchi, T., Saito, Y., Sarukawa, K., Ohno, T., and Matsumura, M., New J. Chem., 2003. **27**: p. 1304.
81. Morris-Hotsenpiller, P.A., Bolt, J.D., Farneth, W.E., Lowekamp, J.B., and Rohrer, G.S., Journal of Physical Chemistry B, 1998. **102**: p. 3216
.
82. Lowekamp, J.B., Rohrer, G.S., Morris-Hotsenpiller, P.A., Bolt, J.D., and Farneth, W.E., Journal of Physical Chemistry B, 1998. **102**: p. 7323.
83. Lowekamp, J. 1999, Carnegie Mellon University Ph.D. Thesis.
84. Kobayashi, M., Petrykin, V., and Kakihana, M, Journal of the American Ceramic Society, 2009. **92**: p. S21-S26.
85. Ohno, T., Sarukawa, K., Matsumura, M., New J. Chem. , 2002. **26**: p. 1167.
86. Goodenough, J.B., Hamnett, A., Huber, G, Hulliger, F., Leib, M., Ramasesha, S.K., and Werheit, H., *Landolt-Bornstein, Numerical Data and Functional*

*Relationships in Science and Technology*, ed. K.H.a.M. Hellwege, O. Vol. 17. 1984, New York: Springer-Verlag.
87. Kumar, M.M., Palkar, V.R., Srinivas, K., Suryanarayana, S.V., Applied Physics Letters, 2000. **76**: p. 2764.
88. Als-Nielsen, J., *Elements of Modern X-ray Physics*. 2001, New York: Wiley.
89. Paratt, L.G., Phys. Rev. , 1954. **95**: p. 359.
90. Adams, B.L., Wright, S.I, and Kunze, K., Met. Trans. A, 1993. **24**: p. 819-831.
91. Herrmann, J.-M., Disdier, J., Pichat, P., Journal of Catalysis, 1988. **113**: p. 72.
92. Clark, W.C., and Vondjidis, A.C., Journal of Catalysis, 1965. **4**: p. 691.
93. Torres, J., and Cervera-March, S., Chem. Eng. Sci. , 1992. **47**: p. 3857.
94. Tanaka, K., Harada, K., and Murata, S., Solar Energy, 1986. **36**: p. 159.
95. Kalinin, S.V., Bonnell, D.A., Physical Review B, 2001. **63**: p. 125411.
96. Kalinin, S.V., Shao, R., and Bonnell, D.A., Journal of the American Ceramic Society, 2005. **88**: p. 1077.
97. Bunge, H.J., *Texture analysis in Materials Science*. 1982, London: Butterworths.
98. Dunn, S., Sharp, S., and Burgess, S., Nanotechnology, 2009. **20**: p. 115604.
99. Emeline, A.V., Furubayashi, Y., Zhang, X., Jin, M., Murakami, T., Fujishima, A., Journal of Physical Chemistry B, 2005. **109**: p. 24441-24444.
100. Miyagi, T., Kamei, M., Sakaguchi, I., Mitsuhashi, T., Yamazaki, A., Japanese Journal of Applied Physics, 2004. **43**: p. 775-776.